Modelling nephron dynamics and tubuloglomerular feedback

Scott J. Graybill

A thesis presented for the degree of
Doctor of Philosophy
in
Bioengineering
at the
University of Canterbury,
Christchurch, New Zealand.

14 July 2010

ACKNOWLEDGEMENTS

This work was made possible by the support, guidance, and understanding of a number of people. I would first and foremost like to thank Alex James and Mike Plank for their guidance, effort, and time. I would also like to thank Tim David and Zoltán Endre, for their expert technical advice; Nicole Kleinstreuer, for making me lift my game; and the postgraduates at UC, for the good times.

I am greatly indebted to Shelley Andreassend for her love, support, and understanding through this process. Thank you to my parents, Jay and Leslie, for all their support and encouragement.

I gratefully acknowledge the financial support from the Mathematics and Statistics department, Mechanical Engineering department, and the University of Canterbury. Without this support, this thesis would not have been possible.

> *In physiology data trumps [sic] theory, unless they exhibit the same properties.* Anon referee

CONTENTS

NOMENCLATURE

0.1 SUBSCRIPTS

a	Afferent arteriole
e	Efferent arteriole
g	Glomerulus
b	Bowman's capsule
t	Tubule

0.2 VARIABLES

$\hat{t} = t_{\text{ref}} t$	s	Time
$\hat{z} = Lz$	m	Tubular distance
x	m	Glomerular distance
$\hat{C}(z,t) = C(z,t) C_{\text{ref}}$	$\text{mol} \cdot \text{m}^{-3}$	NaCl concentration
$\hat{P}(z,t) = P(z,t) P_{\text{ref}}$	Pa	Fluid pressure
$\hat{Q}(z,t) = Q(z,t) Q_{\text{ref}}$	$\text{m}^3 \cdot \text{s}^{-1}$	Volume flow
$\hat{R}(t) = R(t) R_{\text{ref}}$	$\text{Pa} \cdot \text{s} \cdot \text{m}^{-3}$	Resistance
$J_{\text{s}}(z, C(z,t))$	$\text{kg} \cdot \text{s}^{-1} \cdot \text{m}^{-1}$	NaCl reabsorption
$J_{\text{v}}(z, C(z,t))$	$\text{m} \cdot \text{s}^{-2}$	Fluid volume reabsorption

0.3 PARAMETERS

$K_\mathrm{f} = K'_\mathrm{f} Q_\mathrm{ref}/P_\mathrm{ref}$	Filtration fraction
$\pi_\mathrm{i} = \pi'_\mathrm{i} P_\mathrm{ref}$	Input osmotic pressure
$P_\mathrm{e} = P'_\mathrm{e} P_\mathrm{ref}$	Efferent arteriole pressure
$P_\mathrm{d} = P'_\mathrm{d} P_\mathrm{ref}$	Macula densa pressure
$\xi_\mathrm{max} = \xi'_\mathrm{max} R_\mathrm{ref}$	Afferent arteriole resistance range
$\psi = \psi' R_\mathrm{ref}$	Max value of afferent arteriole resistance
$k = k'/C_\mathrm{ref}$	Sensitivity of the TGF response
$C_{\frac{1}{2}} = C'_{\frac{1}{2}} C_\mathrm{ref}$	Inflection point of the TGF curve
$C_\mathrm{in} = C'_\mathrm{in} C_\mathrm{ref}$	Inlet NaCl concentration
$\kappa = \kappa' Q_\mathrm{ref}/L$	Proximal volume reabsorption constant
$\theta = \theta'/L$	Proximal volume reabsorption constant
$L_\mathrm{v} = L'_\mathrm{v} Q_\mathrm{ref}/(L n_\mathrm{s} C_\mathrm{ref})$	Descending limb water permeability
$L_\mathrm{s} = L'_\mathrm{s} Q_\mathrm{ref}/L$	Ascending limb NaCl permeability
$V_\mathrm{max} = V'_\mathrm{max} Q_\mathrm{ref} C_\mathrm{ref}/L$	Michaelis-Menten constant
$K_m = K'_\mathrm{m} C_\mathrm{ref}$	Michaelis-Menten constant
$\eta = \eta' \pi r_0^4 P_\mathrm{ref}/(8 L Q_\mathrm{ref})$	Dynamic viscosity
$z_\mathrm{p} = z'_\mathrm{p} L$	Distance to end of proximal tubule
$z_\mathrm{d} = z'_\mathrm{d} L$	Distance to bend of loop of Henle
$z_\mathrm{a} = z'_\mathrm{a} L$	Distance to end of loop of Henle
L	Tubule length
Λ	Effective blood viscosity constant
n_s	Number of osmoles per mole of NaCl
r_0	Tubule radius
Q_ref	Tubular volume flow reference value
P_ref	Tubular pressure reference value
$t_0 = t_\mathrm{ref}/t'_0$	Afferent arteriole time reference value
$t_\mathrm{ref} = \pi r_0^2 L/Q_\mathrm{ref}$	Tubular time reference value
C_ref	NaCl concentration reference value
$R_\mathrm{ref} = P_\mathrm{ref}/Q_\mathrm{ref}$	Tubular resistance reference value
$\gamma = \gamma' r_0/P_\mathrm{ref}$	Tubular compliance

ABSTRACT

The kidneys are amazingly versatile organs that perform a wide range of vital bodily functions. This thesis provides an analysis into a range of mathematical models of the tubuloglomerular feedback (TGF) mechanism. The TGF mechanism is an autoregulatory mechanism unique to the kidney that maintains approximately constant blood flow to the organ despite wide fluctuations in pressure. Oscillations in pressure, flow, and sodium chloride concentration have been attributed to the action of the TGF mechanism through a number of experimental studies. These oscillations appear spontaneously or in response to a natural or artificial pressure step or microperfusion.

The reason for sustained oscillatory behaviour in nephrons is not immediately clear. Significant research has gone into experimentally determining the signal to the TGF mechanism, but the physiological significance is not mentioned in the literature. Considerable modelling of the oscillations attributed to the TGF mechanism has also been undertaken. However, this modelling uses models that are inherently oscillatory, such as a second-order differential equation or delay differential equations. While these models can be fitted to closely approximate the experimental results they do not address the physiological factors that contribute to sustained oscillations. This thesis aims to determine the contributing factors to the sustained oscillations. By understanding these factors a better hypothesis of the physiological role of the oscillations should be possible.

Chapter 3 presents a mathematical model by Holstein-Rathlou and Marsh [28] that uses a partial differential equation (PDE) model for the tubule and a second-order differential equation for the TGF feedback. The remainder of this chapter shows that oscillations occur without an inherently oscillatory second-order differential equation due to the delays in the system. Tubular compliance was also shown to be necessary for sustained oscillations. Sustained oscillations were not exhibited in the TGF model with a noncompliant tubule. Although damped oscillations were exhibited for a wide range of parameter space. Adding

compliance to the tubule increased the delay around the loop of Henle. This additional delay elicited sustained oscillations.

The computationally expensive PDE model of Chapter 3 was simplified to an ordinary differential equation (ODE) model in Chapter 4 by assuming a spatial profile. This model exhibits much of the same qualitative behaviour as the PDE model including sustained oscillations for similar ranges of parameter space. Compliance was also found to be important in the generation of sustained oscillations in agreement with the PDE tubule model. This model is less computationally expensive than the PDE model and allows analysis that was unfeasible with the PDE model.

Significant natural and artificial blood pressure fluctuation occur in experimental rat models. Chapter 5 examines the effect of inlet pressure forcing on a nonoscillatory and an oscillatory model. The inherently nonoscillatory noncompliant model becomes oscillatory with a physiologically realistic pressure forcing. The oscillatory compliant model remains oscillatory with the addition of a inlet pressure forcing. Pressure fluctuations were hypothesised to contribute to sustained oscillations and could be validated experimentally.

Two extensions to the single nephron TGF models are presented in Chapter 6. A realistic juxtaglomerular delay is added to the single nephron models with both the ODE and PDE tubular models. Physiologically realistic juxtaglomerular delays induce sustained oscillations in the otherwise nonoscillatory noncompliant models. The remainder of this chapter presents a different model for a variable interstitial sodium chloride concentration profile. This model demonstrates experimentally observed function of the countercurrent mechanism by which a concentration gradient is set up and maintained in the interstitium.

Two single nephron models with ODE tubular models are coupled in Chapter 7. The coupling is modelled through the effect on the resistance of their neighbouring nephron's afferent arteriole resistance. The coupled nephron model exhibits entrainment as observed experimentally. Inhibiting the oscillation in one nephron reduces the amplitude of the oscillation in its neighbour. This result compares well with experiments where the TGF mechanism in one nephron is blocked by the administration of furosemide.

Chapter 1

ANATOMY AND PHYSIOLOGY

The urinary system performs three essential bodily functions: excretion, the removal of organic waste products from body fluids; elimination, the discharge of these waste products from the body; and homeostatic regulation of the volume and solute concentration of blood plasma.

The kidneys perform the excretory and regulatory functions of the urinary system. Through their highly specialised anatomy and physiology they are able to rapidly vary the volume and composition of the urine and thus maintain bodily homeostasis of water, ions, and small soluble compounds.

1.1 KIDNEY FUNCTION

The kidneys perform a wide range of functions including:

Regulation of water. Our intake of water through drinking and eating varies widely throughout the day as does our output through sweat, respiration, urination, and defecation. The rate of fluid accumulation in the body depends on the rates of inputs and outputs, over which our bodies have no control except through urination. The kidney possesses the ability to produce large amounts of dilute urine or a small volume of concentrated urine depending on the balance of inputs and outputs.

Regulation of blood pressure. Blood pressure is regulated through regulation of water excretion, as blood pressure is ultimately dependent on blood volume. The kidneys also regulate blood pressure through the vasoaction of smooth muscle cells contained in their vasculature and through generation of renin, which leads to the formation of the powerful vasoconstrictor angiotensin II [17]. Angiotensin II, not only increases blood pressure directly,

it stimulates adrenal gland formation of aldosterone, which indirectly increases blood pressure by stimulating sodium (and water) reabsorption in the kidney.

Regulation of ionic plasma concentrations. The kidneys regulate the concentration of most ions in the blood by varying their concentration in urine. For example, the kidney regulates the concentration of sodium, chloride, potassium, and hydrogen. The concentration of each ion can be regulated independently [17].

Elimination of metabolic waste products. Waste products, such as urea, uric acid, and creatinine, are continuously produced as end products of metabolism. These are excreted by the kidneys before they reach harmful concentrations.

A disruption in any one of these vital bodily functions will have systemic consequences that could be fatal [57].

1.2 GROSS ANATOMY

There are two kidneys in the human body, located on either side of the spine in the posterior of the abdomen. An adult kidney constitutes approximately 0.25% of total body weight at 150 g and is approximately 12 cm long, 6 cm wide, and 3 cm thick. In stark contrast to their small contribution to total body weight, they receive approximately 25% of total cardiac output. Blood is supplied to each kidney via the renal artery through a slit on the concave medial surface called the renal hilus, as seen in Figure 1.1. The renal vein, lymphatics, renal nerve, and ureter also pass through the hilus. Processed blood flows out of the kidney, back to the heart, through the renal vein and urine flows out through the ureter [54].

Figure 1.1 shows the gross structural features and vascularisation of the kidney. The inner section of the kidney framed by the arcuate arteries is called the medulla. It has a striated appearance that results from the parallel arrangement of the blood vessels and elongated capillary beds pass through it [63]. The outer section is called the cortex and has a granular appearance due to the spherical capillary tufts found there, called glomeruli. The blood supply branches approximately six times between entering the kidney through the renal artery and reaching the smallest arteries in the kidney, the afferent arterioles. The renal

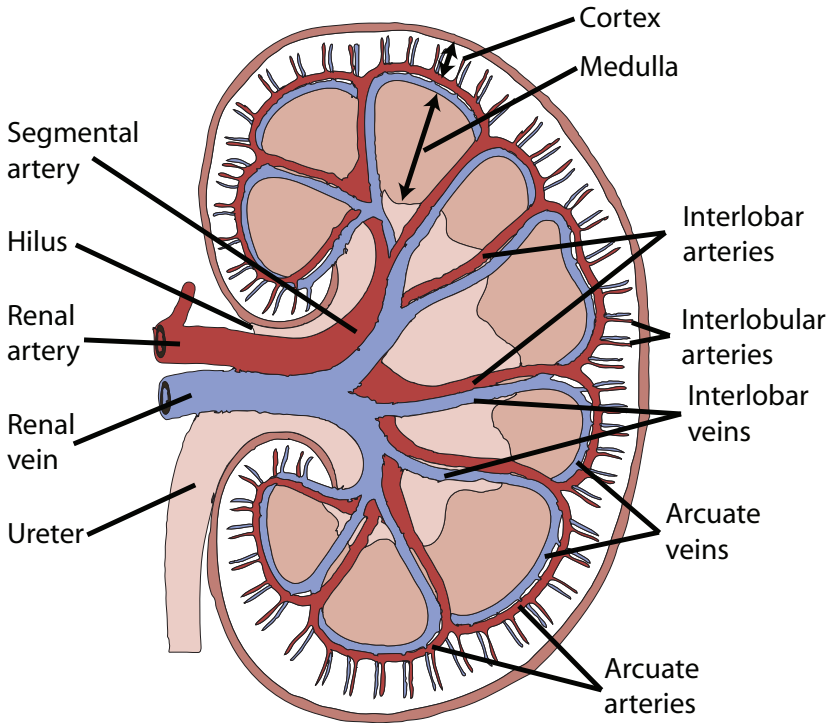

Figure 1.1 A cross-sectional view of the kidney showing the major veins and arteries [57].

artery branches into segmental arteries that in turn branch to form the interlobar arteries. The interlobar arteries pass between the medullary pyramids toward the cortex. Where the medulla and cortex meet these branch again to become the arcuate arteries that arch over the medullary pyramids. Cortical interlobular arteries radiate from the arcuate arteries through the cortex towards the surface of the kidney. Finally, several afferent arterioles branch from each cortical interlobular artery [54]. These afferent arterioles are the feed vessels to the nephrons, the main functional unit of the kidney.

1.3 NEPHRON ANATOMY

The nephron is the basic structural and functional unit of the kidney. Each nephron is individually capable of regulating the volume of water and concentration of soluble substances by filtering the blood, reabsorbing useful components, and excreting the rest. Each human kidney contains approximately one million nephrons. There are approximately 40,000 in a rat kidney.

A nephron consists of two functionally different parts, the glomerulus, G, and the renal tubule shown in Figure 1.2. The renal tubule consists of the tubule from

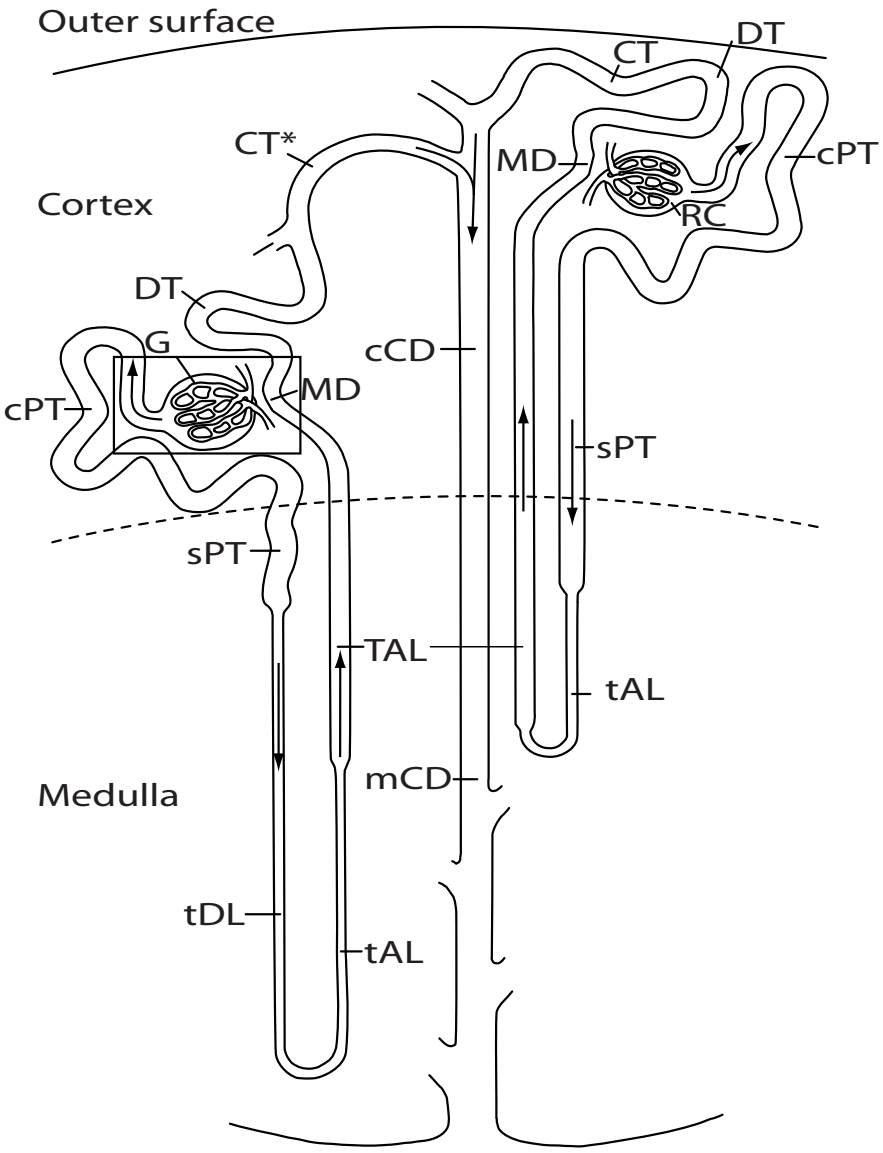

Figure 1.2 Schematic of a long looped nephron (left) and a short looped nephron (right). The dashed line indicated the boundary between the cortex and medulla. The important sections for this study are the: glomerulus, G; proximal convoluted tubule, cPT; proximal straight tubule, sPT; descending thin limb of the loop of Henle, tDL; ascending thin limb of the loop of Henle, tAL; thick ascending limb of the loop of Henle, TAL; macula densa, MD, which is located within the final portion of the thick ascending limb; distal convoluted tubule, DT; connecting tubule, CT; connecting tubule of the juxtamedullary nephron that forms an arcade, CT*; cortical collecting duct, cCD; and medullary collecting duct, mCD. Adapted from [40]. Note: not drawn to scale. The rectangle is reproduced in more detail in Figure 1.3.

the proximal convoluted tubule, cPT, to the distal convoluted tubule, DT.

The glomerulus is a capillary network and is surrounded by Bowman's capsule. Whole blood enters the glomerulus through the afferent arteriole and exits through the efferent arteriole. Fluid is driven from the lumen of the glomerular capillaries through a size- and charge-selective wall, the basement membrane, into Bowman's capsule by the hydrostatic and colloid osmotic pressure difference. This creates an ultrafiltrate, a plasma-like substance free of proteins and blood cells that flows into the renal tubule.

The renal tubule dramatically alters the composition of the incoming ultrafiltrate by reabsorbing the majority of the useful organic nutrients and water that enter the tubular system and secreting additional waste products that did not enter the ultrafiltrate. The tubule is not homogeneous and is divided into the proximal convoluted tubule, descending limb of the loop of Henle, ascending limb of the loop of Henle, distal convoluted tubule, connecting tubule, and collecting duct. Cells in the tubular wall of each section are structurally different and have different physiological properties [17].

1.3.1 Glomerulus

The glomerulus creates an ultrafiltrate of blood by sieving out blood cells and large plasma proteins. The tubule lacks a mechanism to reabsorb these. Blood enters the glomerulus through the afferent arteriole and leaves through the efferent arteriole as shown in Figure 1.3. The glomerulus is a capillary bed that branches and anastomoses up to fifty times. It is surrounded by a blind-ended tubule called Bowman's capsule. The pressure difference between the lumen of the glomerular capillary bed and the lumen of Bowman's capsule causes a filtrate to flow through the permeable capillary wall into Bowman's space, from where it enters the proximal tubule.

The capillary wall, also known as the glomerular membrane, is made up of three layers. The inner layer that lines the glomerular capillaries is called the capillary endothelial layer. The basement membrane layer surrounds the capillary endothelial layer and the epithelial layer surrounds the basement membrane. The glomerular wall is 100 to 500 times more permeable than an ordinary capillary. This increased permeability permits a larger amount of fluid to be processed and allows the kidney to rapidly alter the composition of the blood. The capillary endothelial layer is made up of a single layer of endothelial cells. The filtrate cannot

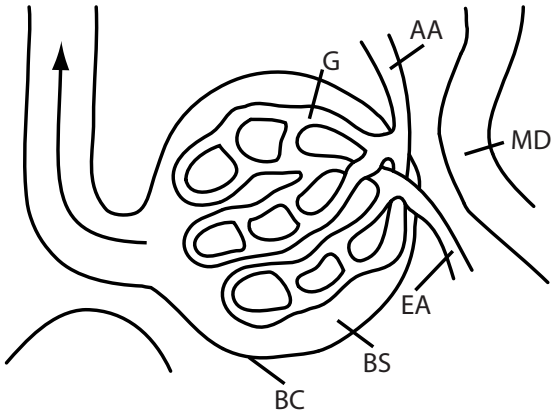

Figure 1.3 Enlarged schematic of the renal corpuscle from the rectangle in Figure 1.2. Anatomy important for this study is the: afferent arteriole, AA; efferent arteriole, EA; Bowman's capsule, BC; Bowman's space, BS; glomerulus, G; and macula densa, MD. Adapted from [40].

pass between adjacent endothelial cells because they are in contact. The filtrate instead passes through several pores in the endothelial cells called Fenestre. The endothelial layer prevents blood cells and platelets from coming into contact with the basement membrane. The basement membrane is the main filtration barrier and selectively allows passage of molecules depending on their shape, charge, and size. Molecular size is the main determinant of filtration. The number of molecules with a molecular weight greater than 70 kDa passing through the capillary wall is insignificant. The basement membrane also has fixed anions that repel anionic molecules like the plasma proteins, although this is only significant for molecules with molecular weights close to 70 kDa. Albumin is a negatively charged protein with a molecular weight of 65 kDa.

1.3.2 Proximal tubule

The filtrate enters the proximal tubule after exiting Bowman's capsule. There are two sections to the proximal tubule that can be distinguished by the cells that make up the cell wall. The first section of the proximal tubule is convoluted (pars convoluta) and the second part is straight (pars recta). The convoluted section consists of cuboidal/columnar cells that have millions of microvilli on the luminal surface. This greatly increases the surface area and hence the tubular reabsorption of tubular fluid. Adjacent pars convoluta cells are joined closely together on their luminal side but have a space on the peritubular side called the lateral intercellular space.

The bulk phase of reabsorption occurs in the proximal tubule. All the proteins, glucose, and amino acids from the glomerular filtrate are reabsorbed along with approximately 65% of the water.

1.3.3 Loop of Henle

The loop of Henle is the next section of the nephron after the proximal tubule. The loop of Henle is divided into three sections: the descending limb, thin ascending limb, and thick ascending limb. The start of the loop of Henle is generally considered to be where the wall of the tubule changes from being a thick-walled tubule (the proximal tubule) to being a thin-walled tubule. The thin ascending limb begins at the bottom of the Loop and the thick ascending limb begins when the tubular wall becomes thick again. The epithelial cells of each section of the loop of Henle have different properties.

The thin descending section allows water egress into and absorbs ions, such as chloride and sodium, from the interstitium. Thus, the concentration of ions in the interstitium increases down the descending section of the loop of Henle. The thick ascending limb of the loop of Henle actively transports ions such as chloride and sodium but is impermeable to water. Thus, the fluid in the tubular lumen becomes less concentrated, that is the osmolality decreases. The main effect of water and ion transport of the loop of Henle is to keep the interstitial fluid in the medulla at a much higher solute concentration than tubular fluid (and blood plasma). This facilitates the control of net water movement by the kidney, which is finely and finally regulated in the collecting duct.

1.3.4 Juxtaglomerular apparatus

The ascending limb of the loop of Henle passes closely between the afferent and efferent arteriole of its own glomerulus. This is the location of sensation and actuation of the tubuloglomerular feedback (TGF) mechanism and is referred to as the juxtaglomerular apparatus (JGA). The JGA comprises: the macula densa cells of the ascending limb of the loop of Henle, the cells of the extra-glomerular mesangium, which fill the angle between the afferent and efferent arterioles, and the modified vascular smooth muscle cells of the afferent arteriole [69].

1.3.5 Distal convoluted tubule

The distal convoluted tubule begins shortly after the plaque of macula densa cells in the most distal section of the ascending limb [40]. It is an important site for the reabsorption and active secretion of various ions and the reabsorption of water [57].

1.3.6 Collecting duct

Each collecting duct is fed by several nephrons through the distal convoluted tubule. In the distal convoluted tubule, ion and water transport is finely controlled by various hormones including aldosterone, which increases Na^+ reabsorption and K^+ and H^+ secretion In the collecting duct, arginine vasopressin (AVP) controls water reabsorption. In the presence of AVP, also known as antidiuretic hormone (ADH), the walls of the collecting duct become permeable to water through the insertion of a water transporting protein, called aquaporin 2, into the luminal cell membrane. As the interstitium is hyperosmotic this allows water to move osmotically from the lumen of the collecting duct creating a concentrated urine. Without AVP, the collecting duct is relatively impermeable to water. This results in a dilute urine because the concentration is unchanged as it passes through the collecting duct [63].

1.3.7 Peritubular capillaries/vasa recta

Anatomically the peritubular capillaries and vasa recta are interlaced around the loop of Henle. The vasa recta, which follow the loops of Henle of juxtamedullary nephrons, contain many branches and anastomoses. The peritubular capillaries are fed from the efferent arteriole. This configuration of two capillary beds in series is unique to the kidney. The peritubular and vasa recta capillary beds reabsorb the filtrate created by the glomerular capillary bed.

1.3.8 Interstitium

The interstitium comprises less than 10% of the renal volume. It contains scattered interstitial cells (fibroblasts and others) that synthesise an extracellular matrix of collagen, proteoglycans, and glycoproteins including erythropoietin, which stimulates bone marrow production of red blood cells [17].

1.4 NEPHRON HETEROGENEITY

There are significant anatomic, biochemical, and functional variations between nephrons [17]. Nephrons can be divided into three groups depending on the location of their renal corpuscle in the cortex [63]. The corpuscles of superficial nephrons are located within 1 mm of the capsular surface, mid-cortical corpuscles are located in the mid-cortex, and juxtamedullary nephrons corpuscles are located just above the cortex medulla junction [17]. Two types of nephrons are shown in Figure 1.2: a superficial and juxtamedullary nephron on the left and right, respectively. A major distinction between the three types of nephron is the length of their loops of Henle. Superficial nephrons have short loops that make their hairpin turn above the outer inner medulla junction. Juxtamedullary nephrons have long loops of Henle that extend into the inner medulla. Mid-cortical nephrons may have either short or long loops of Henle. A group of nephrons with a distribution of lengths can produce a more concentrated urine than a group with the same lengths, as shown in a model by Hoppensteadt and Peskin [31].

1.5 RENAL MECHANISMS

1.5.1 Transport mechanisms

The nephron alters the constituents of the fluid in the renal tubule by transporting various substances across the epithelium between the lumen and the interstitium. This can happen via the paracellular route or the transcellular route. The paracellular route passes between the cells of the epithelium where the transcellular route passes directly through the epithelium cells. Transcellular transport is a two-stage process as the substance must pass into the cell cytoplasm through the apical membrane then pass through the basolateral membrane into the interstitium.

Transport can occur in two ways: active or passive processes. Active processes require metabolic energy from the cell to move substances across the cell membrane where passive processes do not. A secondary active transport process uses the electrochemical gradient, explicitly the potential or concentration gradient, established by an active process for transport. A secondary active transport process does not explicitly require energy, although its activity is directly dependent on an energy-reliant active process.

Passive transport

The three germane passive transport processes are diffusion, osmosis, and filtration. Substances moved by passive transport processes can take either the transcellular or the paracellular route.

Diffusion is the net transport of molecules or ions from a region of high concentration to a region of low concentration. The energy for diffusion comes from the kinetic energy of the particles. If the particles have a higher kinetic energy, for example a higher temperature, they will diffuse more quickly through the medium. In a transport setting, the movement down the concentration gradient occurs across the epithelial cells comprising the tubule wall. Not all substances will diffuse across the epithelial cell wall because the plasma membrane is selectively permeable. A molecule or ion will diffuse if it is: lipid soluble, small enough to pass through membrane channels, or is assisted by a carrier molecule [54]. Ions such as sodium and chloride are not lipid soluble and must pass through the membrane channels. Membrane channels are a mechanism for rapidly moving large amounts of a certain substance, for example potassium or calcium, across a membrane that might otherwise allow diffusion slowly or not at all.

Osmosis is the same process as diffusion except that it describes diffusion of a solvent rather than a solute. Water, the universal solvent, moves down its concentration gradient from an area of high concentration to an area of low concentration. With respect to transcellular transport, water must pass through the channels as it is lipid insoluble and cannot pass directly through the membrane.

Filtration is the process by which water and solutes are driven through a membrane or capillary wall by the difference in hydrostatic pressure. Water and solutes are transported across the membrane wall down the pressure gradient from an area of high pressure to an area of low pressure. Filtration is solely size selective; only molecules small enough to pass through the membrane channels permeate.

Active/secondary active transport

The two main forms of secondary active transport are countertransport and cotransport. Countertransport moves two or more solute species in opposite directions across a membrane, in contrast to cotransport that moves two or more solute species in the same direction. The energy for secondary active transport processes comes from one of the species moving down its electrochemical gradi-

ent, usually sodium. Active and secondary active transport processes only move substances via the transcellular route. In contrast to channels, transporters move substances at a much lower rate because the substances bind more strongly to the transport protein [17].

The Na-K-2Cl (NKCC2) cotransporter is one of the important secondary active transport processes in the nephron. The NKCC2 cotransporter moves one sodium ion, one potassium, and two chloride ions across the apical membrane from the nephron lumen into the cytoplasm. It is a secondary active transport process as it requires the operation of the active Na-K-ATPase pump in the basolateral membrane to constantly remove sodium from the cells of the epithelium. This provides a sodium concentration gradient and hence the energy required for the operation of the NKCC2 cotransporter.

1.5.2 Autoregulatory mechanisms

Blood pressure varies widely throughout the day due to a wide range of factors including: physical activity, stress, circadian rhythm, respiratory cycle, and heart beat [11]. The kidneys exhibit highly efficient autoregulation, a process by which blood flow remains relatively constant as pressure fluctuates as shown in Figure 1.4 from Eaton and Pooler [17]. Renal blood flow drives filtration, and its autoregulation is important as it actively stabilises water and ion excretion and protects renal structure. Without the autoregulatory function of the kidney, a spike in blood pressure would cause prolonged salt and water loss by exceeding cellular transport mechanisms, and could damage the glomerular capillary bed. Conversely, low blood pressure would reduce the ability of the kidneys to rapidly regulate plasma volume, the concentration of various ions, and clear metabolic wastes. The entire autoregulatory process of sensation, transduction, and actuation occurs within the kidney and is independent of any central neural or hormonal control [14]. The kidney also autoregulates the amount of fluid entering the tubule in addition to blood flow.

There are two widely recognised autoregulatory mechanisms in the kidney: the myogenic mechanism and the tubuloglomerular feedback (TGF) mechanism. Together, they account for 90% of the renal autoregulatory response [37]. The remainder is attributed to a third mechanism, although its cause, possibly adenosine triphosphate, angiotensin II, or a slow component of the myogenic response [32], and physiological function is currently unclear [14]. Pressure events occurring faster than 0.3 Hz are generally believed to be handled passively by the renal

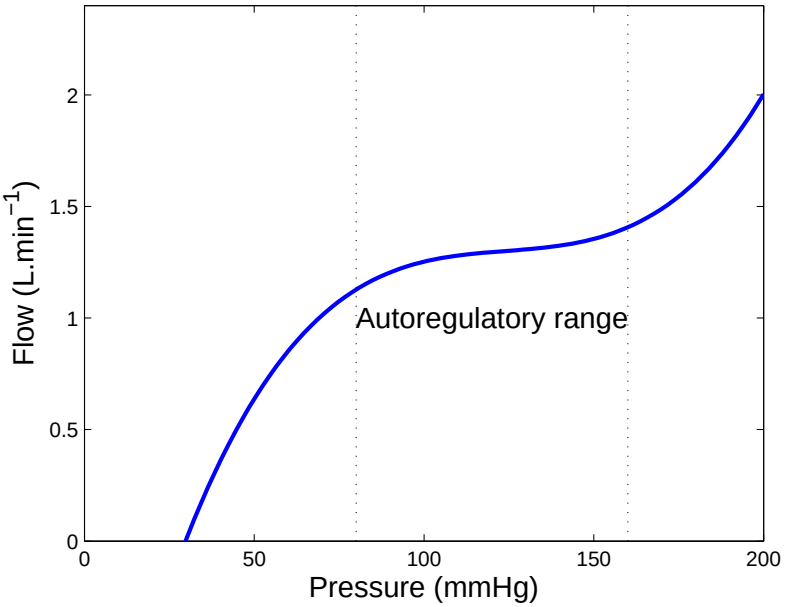

Figure 1.4 Typical autoregulation curve [17]. Note the flow is nearly constant throughout the autoregulatory range.

vasculature [52]. Autoregulation blunts the change in arterial pressure as renal blood flow and glomerular filtration rate change, in the autoregulatory range, but does not completely prevent any change [17].

Myogenic mechanism

The myogenic mechanism was first discovered by Bayliss over 100 years ago [37]. The myogenic response is a pressure-induced vasoconstriction or dilation of the vasculature [52]. While a myogenic response exists throughout the renal vasculature, its effect is much greater in the smaller diameter distal sections of the vasculature [37].

A myogenic response is elicited by an increase in intraluminal pressure stretching blood vessel walls, which opens stretch-activated cation channels in smooth muscle cells. The ensuing membrane depolarisation opens voltage-dependent calcium (Ca^{2+}) channels, and intracellular calcium concentration rises, causing smooth muscle contraction. Vessel lumen diameter decreases and vascular resistance increases. Decreased blood pressure causes the opposite changes [63].

The response times of the myogenic mechanism vary greatly throughout the vascular tree. The response time of the smallest arteries is typically the fastest

with the smallest arteriole, the afferent arteriole, acting on a time scale of 3–10 s [51].

Tubuloglomerular feedback (TGF) mechanism

The cells of the macula densa play the sensory role in the TGF autoregulatory mechanism. While it remains uncertain which specific property of the flow is sensed [14], there is strong evidence that the sodium chloride (NaCl) delivery at the macula densa is an important signal to the TGF mechanism [28].

NaCl enters the macula densa cells apically through either a Na-K-2Cl (NKCC2) cotransporter or a sodium hydrogen exchanger, NHE2. The NKCC2 cotransporter accounts for approximately 80% of the apical NaCl entry. This transporter has a higher affinity for chloride than its other isoforms and is able to reabsorb NaCl even at the lower limit of normal NaCl concentration (15–25 $\mathrm{mmol \cdot L^{-1}}$). However, the isoform exhibits saturation and maximal transport rates at a luminal NaCl concentration of 60 $\mathrm{mmol \cdot L^{-1}}$. The remaining 20% enters through NHE2. Unlike NKCC2, this sodium hydrogen exchanger does not saturate as levels of luminal NaCl concentration are raised above 60 $\mathrm{mmol \cdot L^{-1}}$. The high affinity for NaCl entry across the apical membrane along with the relatively weak sodium secretion, may result in macula densa cell NaCl concentrations tracking changes in luminal NaCl concentration. Logically, this behaviour is necessary if fluid composition is to be the TGF signal.

The close proximity of the macula densa and smooth muscle cells allows for rapid signal transfer. Although they are in close proximity, there are no cell-to-cell junctions and they are thought to communicate via the release of paracrine signalling factors including ATP, prostaglandin $\mathrm{E_2}$, and nitric oxide [38].

Actuation is affected by the smooth muscle cells of the afferent arteriole that constrict or relax depending on the level of hormonal activation and intracellular calcium concentration. High NaCl concentration at the macula densa leads to constriction of the afferent arteriole, whilst low NaCl concentration leads to dilation [33]. Constriction of the afferent arteriole leads to lower flows and hence lower concentrations, where dilation leads to higher flows and hence higher concentrations, thus bringing the system back towards its equilibrium. This negative feedback mechanism acts to maintain the NaCl concentration at the macula densa within a relatively narrow range. The dynamic range of the TGF mechanism occurs over a range of NaCl concentration of 15–60 $\mathrm{mmol \cdot L^{-1}}$ with maximal response occurring at or above 60 $\mathrm{mmol \cdot L^{-1}}$ [38].

Prolonged activation of the TGF mechanism, by a high NaCl load, leads to an upward shift of the whole dynamic range. This resetting implies that the TGF mechanism loses its ability to correct the long-term perturbation. Resetting is beneficial as the TGF mechanism retains its ability to regulate shorter term perturbations in this higher dynamic range. The TGF mechanism resets over a time period of 20–60 min and is mediated by nitric oxide synthase produced in the macula densa [32].

The TGF response is almost completely abolished by luminal administration of furosemide. Furosemide is known to block the apical NKCC2 cotransporter [38]. The response of the TGF can be modulated by various hormones including angiotensin II. Low-dose angiotensin II has been shown to increase both NHE2 exchanger activity and apical NKCC2 cotransporter activity. This suggests that angiotensin II enhances the transport of NaCl across the apical membrane increasing the sensitivity of the TGF mechanism [38].

1.5.3 Countercurrent mechanism

The countercurrent mechanism creates a NaCl concentration gradient in the interstitium due to the transport properties of the descending and ascending limbs of the loop of Henle. The relatively small NaCl concentration difference created by the active pump in the ascending limb is multiplied by the close anatomical configuration of two tubules with flow in opposite directions. The NaCl concentration in the cortex is typically 300 mOsm and increases to a maximum of approximately 1200 mOsm deep in the medulla. The kangaroo rat has longer loops of Henle than a human and is able to produce a urine more concentrated than sea water through the multiplicative action of the countercurrent mechanism.

Chapter 2

PREVIOUS WORK

The kidney has been extensively studied from both experimental and, more recently, mathematical modelling perspectives. Despite this effort and the huge steps in current knowledge many of the complexities of the kidney still elude current scientific understanding. From a clinical perspective, early detection of renal failure is arguably the most critical problem. The current methods, for example measuring the glomerular filtration rate using the creatine clearance rate, are invasive, costly, and are often only measured after it is clear that renal dysfunction is occurring. Clinicians are also interested in understanding how diseases such as polycystic kidney disease, hypertension, and diabetes occur, can be detected, and can best be managed. In terms of modelling, the current focus is understanding how the two autoregulatory mechanisms interact in a single nephron and elucidating the function of the third autoregulation mechanism. With recent advances in computing power, modelling the dynamics of large populations of detailed single nephron models has become feasible. Current research aims to determine the effect of large numbers of interacting nephrons on the autoregulatory capability of the kidneys.

2.1 EXPERIMENTAL WORK

There is a large body of experimental studies on the kidney. Renal experiments are conducted both *in vivo* and *in vitro* on a wide range of animals including rats, mice, pigs, and goats. Work is conducted on both healthy animals and pathological animal models, for example those with hypertension and diabetes. The experimental work that is relevant to this thesis relates to the TGF mechanism, sustained oscillations, and nephron coupling.

The rat experimental models commonly used in renal research are Sprague-

Dawley (SD), Wistar-Kyoto (WKY), and spontaneously hypertensive (SHR). SD and WKY are normotensive animal models meaning that they have normal blood pressure. SD rats are commonly used because of their calmness and ease of handling. SHR rats are the most common rat model of hypertension. Hypertension develops at approximately 5–6 weeks of age. Both SD rats and SHR models were developed by selective breeding of WKY rats.

The TGF mechanism has been studied extensively experimentally. It is generally accepted that the sodium chloride (NaCl) concentration at the macula densa is the signal to the afferent arteriole [43]. The TGF mechanism is a negative feedback mechanism that provides homeostasis to distal NaCl delivery. The steady state response function relating NaCl concentration and afferent arteriole resistance empirically fits a logistic curve. The steady state function was found to be identical between SD and WKY [10].

Sustained oscillations in proximal tubule pressure, flow, and NaCl concentration have been observed in a number of experiments. Sustained oscillations are seen to occur spontaneously, or with elicitation by: microperfusion or suction of artificial tubular fluid, a jump in mean arterial pressure, or intravenous infusion. While the frequency of these sustained oscillations varies significantly between animals, between nephrons of an individual animal, and with anesthetic used, it is generally considered to fall within the range of 0.02–0.05 Hz in normotensive animals. The dynamics of the tubular pressure were also the same in the two normotensive strains [10]. Irregular oscillations in an animal model of hypertension have also been widely reported [23, 50]. In contrast to the single, well defined peak in spectral power of the normotensive animals, spontaneously hypertensive animals have several peaks in spectral power at frequencies that fall within the generally accepted range of TGF elicited sustained oscillations of 0.02–0.05 Hz.

Pairs of nephrons originating from the same interlobular artery oscillate in phase at the same frequency [24]. Oscillations in one of the pair is effected by varying the amplitude of the oscillations in the other, through microperfusion of artificial tubular fluid or by loop diuretics like furosemide [24].

2.1.1 The tubuloglomerular feedback (TGF) mechanism

The TGF mechanism was first proposed by Goormaghtigh in 1937 [46] based on the close anatomical arrangement of the macula densa and the afferent arterioles. His hypothesis was unable to be tested until the development of micropuncture

in the 1960's. The steady state response of the TGF mechanism has been studied extensively experimentally [8]. The first experiments were conducted by inserting a wax block into the proximal tubule. This stopped the flow through the nephron and is referred to as open-loop micropuncture because it effectively isolated the sensor and effector, opening the feedback loop. Artificial tubular fluid was then microperfused downstream of the wax block and various relationships were established, for example the relationship between flow through the proximal tubule and glomerular pressure. The limitation of this experimental procedure was that it severed the feedback loop and hence the nephron was not operating as it would *in vivo*. In the 1980's, Moore suggested that the *in vivo* TGF response of the nephron could be better measured by not blocking the tubule and measuring the response to a pressure perturbation, closed-loop micropuncture. This method is still invasive to the *in vivo* function of the TGF mechanism as micropipettes are required to be inserted into the tubule. The least invasive technique is know as videometric flow velocitometry (VMFV) [46]. This involved inserting small boluses of a substance that could be tracked into the tubule. The boluses are tracked by video from which the velocity of the fluid was calculated. While this method is considered to be non-invasive in the literature it still requires micropuncture of the tubule and insertion of fluid, usually in a pulsatile fashion. The characteristic steady state response curve most often discussed in the literature relates flow through the proximal tubule and single nephron glomerular filtration rate. Figure 2.1 shows the idealised TGF response curve relating late proximal flow, VLP, and single nephron glomerular filtration rate, SNGFR. This curve is typically fitted by a logistic function with four parameters: the coordinates of the inflection point, the maximum range, and the slope of the curve at the turning point (often referred to as the gain of the TGF system).

While Figure 2.1 is one representation of the steady state TGF response, a more physiologically insightful TGF steady state response curve relates the NaCl concentration at the macula densa with the resistance of the afferent arteriole. It is widely accepted that the NaCl concentration at the macula densa is the signal to the TGF mechanism [43]. High NaCl concentrations at the macula densa constrict the afferent arteriole, reducing single nephron glomerular filtration in turn reducing the NaCl concentration at the macula densa. A low NaCl concentration has the opposite effect [38]. The complex signalling processes between the macula densa cells and the smooth muscle cells of the afferent arteriole involve a number of intermediaries including calcium, adenosine triphosphate, and prostaglandin [39]. The signalling process is not totally understood [32].

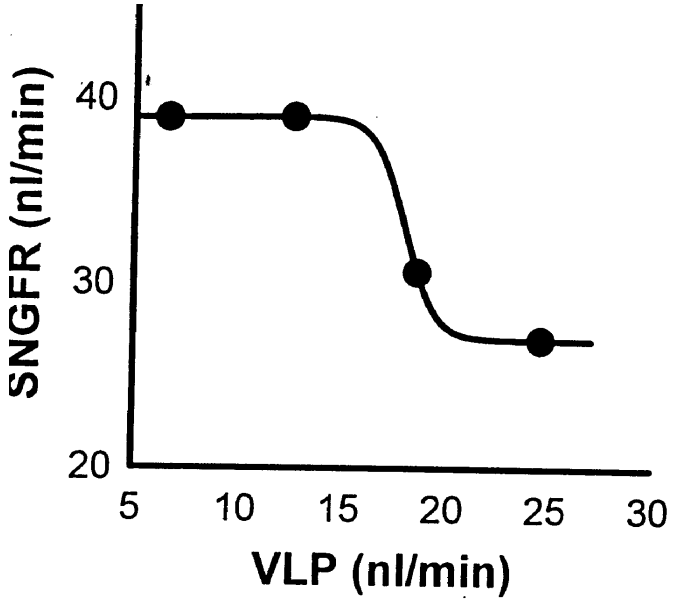

Figure 2.1 From Layton and Weinstein [46]. Shows an idealised steady state response curve that relates late proximal flow, VLP, to single nephron glomerular filtration rate, SNGFR. The points represent pieces of experimental data.

2.1.2 Sustained oscillations

An early experiment by Leyssac and Baumbach [47], demonstrated the existence of sustained intratubular pressure oscillations occurring at a frequency of approximately 0.03 Hz in the proximal tubule of the loop of Henle. These sustained oscillations occurred in 16 of 17 male, halothane-nitrous oxide-oxygen anesthetised Sprague-Dawley (SD) rats. Proximal intratubular pressure was measured concurrently with systemic arterial pressure. A Fourier transform showed that the 0.03 Hz sustained oscillations were absent from the systemic pressure recording, indicating that this was a locally occurring phenomenon. The maximum amplitude of the proximal pressure oscillations was 3.41 ± 1.29 mmHg and the sustained oscillations lasted for 9.38 ± 4.02 min. The oscillations could be elicited or existing oscillations could be markedly amplified by a small, 2.5 $\mathrm{nL} \cdot \mathrm{min}^{-1}$ intravenous infusion of 0.9% NaCl solution. They concluded that as the microperfusion did not disturb the vascular system, the signal eliciting the oscillation was likely to be transmitted to the vessels from the distal tubular lumen, defining the oscillation as a TGF response. Spontaneous increases or decreases in mean arterial pressure (MAP) of 5–10 mmHg during an experiment were also observed to elicit oscillations.

In a follow-up study Leyssac [49] reproduced the earlier findings in [47] of

0.03 Hz sustained oscillations in proximal tubule pressure. In addition to these oscillations a faster, 0.175 Hz oscillation was also observed for very high microperfusion rates of 25.4 $\mathrm{nL} \cdot \mathrm{min}^{-1}$ in four of five experiments. Leyssac [49] abolished the oscillations by microperfusion of furosemide, 0.1 $\mathrm{mmol} \cdot \mathrm{L}^{-1}$, which was known to block NaCl transport in the thick ascending limb [20], and correctly concluded that the signal activating the oscillations was transmitted by some change in the composition of the macula densa reabsorbate. Sustained oscillations returned within two minutes after cessation of furosemide.

Leyssac and Holstein-Rathlou [48] investigated the effects of five transport inhibitors including furosemide. Their group reproduced the earlier findings that microperfusion of furosemide at 0.1–2.0 $\mathrm{mmol} \cdot \mathrm{L}^{-1}$ inhibited the slow TGF elicited sustained oscillations in 24, and partially inhibited 4, of 30 experiments. In addition, they microperfused a lower concentration of furosemide, 0.05 $\mathrm{mmol} \cdot \mathrm{L}^{-1}$, and observed partial inhibition of the oscillations in 18 of 18 of which 13 exhibited irregular oscillations. The power spectrum of the irregular oscillations exhibited three distinct peaks in power between 0.02 Hz and 0.04 Hz. Bumetanide inhibited the slow TGF elicited sustained oscillations in 17 of 23 male SD rats and partially inhibited oscillations in the other 5, shown in Figure 2.2B. The other three transport inhibitors used: amiloride, bendroflumethiazide, and acetazolamide, were deemed to have the same effect as microperfusion of artificial tubular fluid (ATF). Of these five transport inhibitors only those with an action in the thick ascending limb, furosemide and bumetanide, inhibited or abolished the sustained proximal tubule pressure oscillations. This finding strongly supports the conclusions of [47] and [49] that the pressure oscillations are mediated by the composition of the macula densa reabsorbate.

Sustained oscillations were also observed in Wistar-Kyoto (WKY) rats, another normotensive strain, by Holstein-Rathlou and Leyssac [23]. The frequencies of the oscillations in the WKY rats varied over a range of frequencies from 0.020 Hz to 0.0467 Hz [23]. This relatively wide range indicates high variability between individual nephrons. These frequencies correspond well with the frequency of 0.03 Hz measured previously by [47] and [49]. Holstein-Rathlou and Leyssac [23] also measured the proximal tubule pressure in spontaneously hypertensive rats (SHR), an animal model of hypertension. They observed the tubular pressure oscillations to be highly irregular. The power density spectrum shows several peaks in power on the 20–40 mHz range in contrast to one well-defined peak in the WKY rats. The power of the SHR peaks was approximately half that

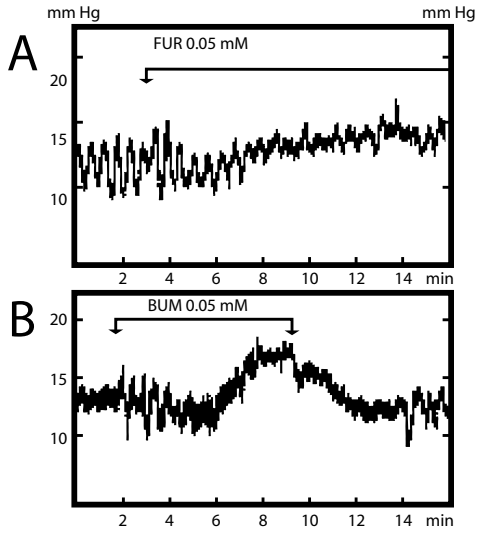

Figure 2.2 Reproduced from Leyssac and Holstein-Rathlou [48]. **A**: Microperfusion of furosemide 0.05 mmol $\cdot$ L^{-1} at 5 nL $\cdot$ min^{-1} abolishes the TGF elicited oscillations. **B**: Microperfusion of bumetanide 0.05 mmol $\cdot$ L^{-1} at 7 nL $\cdot$ min^{-1} initially activates the slow oscillations during the first 3–4 min of administration thereafter the slow oscillations were diminished and gradually disappeared. During the administration of furosemide, at 0.05 mmol $\cdot$ L^{-1}, the pressure exhibits irregular oscillations. At a higher concentration of 0.1 mmol $\cdot$ L^{-1} the oscillations are completely abolished [48].

of the WKY [23].

All rats in experiments are anesthetised. The two commonly used anaesthetics are halothane inhalation and barbiturate anesthesia. Anaesthesia has been shown to have an effect on renal function and that different anaesthetics have different effects [25]. For example, the tubular compliance after inactin, a commonly used barbiturate anaesthetic, is double that found with halothane anaesthetised rats [49]. There is evidence that the type of anesthetic also changes the slope of the TGF response [42]; barbiturate anesthetised animals have a smaller TGF slope than those that were halothane anesthetised.

Sustained oscillations in flow and NaCl concentration were first reported in an experimental paper by Holstein-Rathlou and Marsh [27]. They simultaneously measured proximal intratubular pressure and either late proximal pressure, distal chloride concentration, or distal tubular pressure. They were unable to measure all four variables simultaneously and chose to measure proximal pressure in each experiment to provide a baseline that the other three variables could be compared to. Simultaneous proximal pressure and distal chloride concentration time series are shown in Figure 2.3. The distal measurements were made in the earliest accessible distal convolution. One of the main results of this paper was to quantify

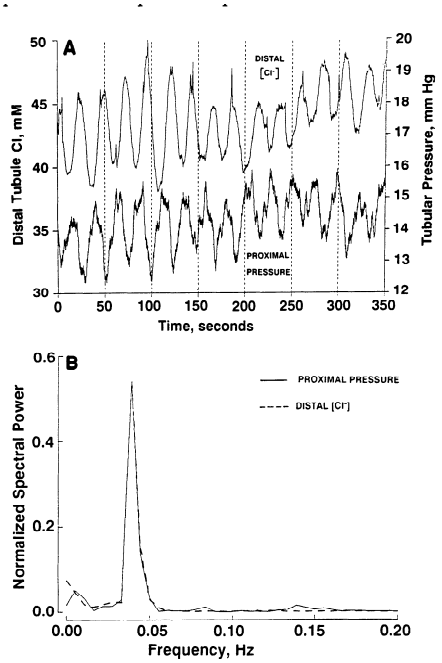

Figure 2.3 Reproduced from Holstein-Rathlou and Marsh [27]. **A**: typical recording of proximal tubule pressure and distal chloride concentration. A delay of approximately 10 s can be identified between the proximal pressure and distal chloride concentration. **B**: corresponding power spectra. Both proximal pressure (solid) and distal chloride concentration (dashed) show a well defined peak in power at approximately 0.04 Hz.

the phase relationships between the flow, pressure, and distal chloride concentration oscillations. In relation to proximal pressure: distal chloride was delayed 8.9±0.8 s, distal pressure was delayed 1.05±0.38 s, and proximal flow was delayed -1.5±0.4 s. The 8.9 s delay between proximal pressure and distal chloride concentration was approximately half the period of the oscillations ($T \approx 25$ s). Thus, the pressure and distal chloride concentration time series were approximately in antiphase.

In summary, sustained and irregular oscillations have been attributed to the action of the TGF mechanism. Sustained oscillations in pressure, volume flow, and NaCl concentration occurs in most, but not all, normotensive rats. These rats were anesthetised using halothane inhalation or a barbiturate, both of which are known to have an effect on renal function. The oscillations are known to be caused by the TGF mechanism because when the TGF sensor is blocked by furosemide, the oscillations are abolished. In contrast to the regular oscillations seen in normotensive animal models, hypertensive animals exhibit chaotic, non-periodic fluctuations. It is still unclear if these oscillations arises from delays in the system, a cellular oscillator, interaction with another mechanism such as

the myogenic mechanism, a combination of these, or some other reason. The physiological significance is also unclear. An oscillating tubule has a greater cross-sectional area if the radius is varying like a sine wave. This permits a higher volume flow than a tubule of constant radius, which allows a higher blood flow to the kidney. Alternatively, sustained oscillations may be unavoidable in this system due to the inherent delays around the loop of Henle. Or maybe the oscillations do not occur naturally *in vivo*, and are elicited by the experimental procedure.

2.1.3 Coupling

Leyssac [49] showed that neighbouring nephrons did not oscillate in phase or with the same amplitude and that they oscillated at a slightly different frequency. This result suggests that oscillations are regulated independently in individual nephrons. This result is contradicted by the results shown in Holstein-Rathlou [24], which showed that subpopulations of nephrons oscillated with the same frequency and phase. [24] examined two groups: A) pairs of nephrons sharing the same interlobular artery and B) pairs of nephrons not sharing the same interlobular artery. These contradictory results can be explained by the difference in experimental procedure. Leyssac [49] chose two nephrons that were close but did not necessarily share the same interlobular artery, as done in Holstein-Rathlou [24]. Twenty-nine of 33 nephron pairs from group A showed synchronised pressure oscillations in contrast to 1 of 23 pairs of group B, as shown in Figure 2.4.

In addition they showed that experimentally abolishing, attenuating, or eliciting oscillations in one nephron from group A provoked a similar response in its pair. Modulating the oscillations in a group B nephron had no effect on its pair. The oscillations were affected by either microperfusion of artificial tubular fluid (5–12 $\mathrm{nL \cdot min^{-1}}$ or 20–30 $\mathrm{nL \cdot min^{-1}}$) or microperfusion of 0.2 $\mathrm{mmol \cdot L^{-1}}$ furosemide, known to abolish or attenuate the TGF or attenuate the TGF elicited oscillations. Figure 2.5A shows the effect of microperfusion of a group A nephron with 25 $\mathrm{nL \cdot min^{-1}}$of artificial tubular fluid. The oscillations in the perfused nephron were abolished, while the oscillations in the neighbouring group A nephron were attenuated. Shortly after microperfusion ceased, both nephrons returned to synchronous oscillations. Disruption of the oscillations in a group B nephron had no effect on the corresponding group B nephron, as shown in Figure 2.5B.

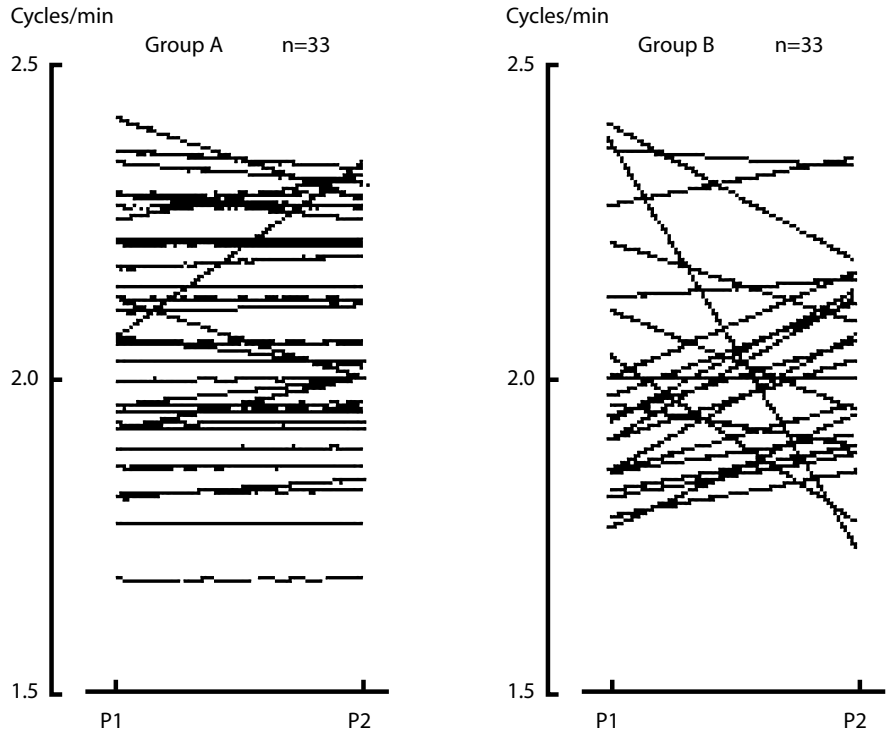

Figure 2.4 Reproduced from Holstein-Rathlou [24]. Correlation between frequencies in coupled (**A**) and uncoupled (**B**) pairs of nephrons. P_1 and P_2 are is nephron 1 and nephron 2 in a coupled pair, respectively.

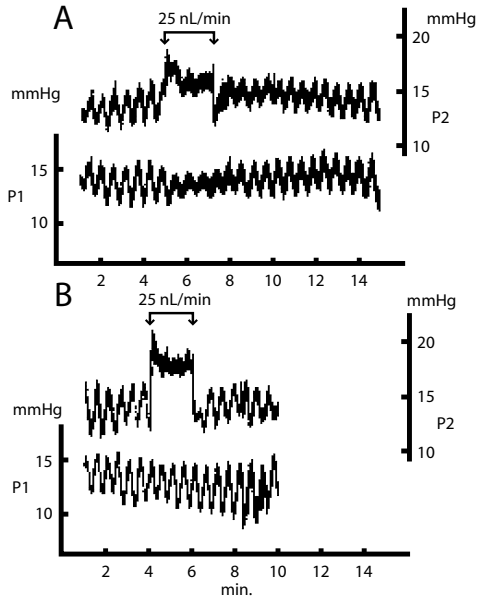

Figure 2.5 Reproduced from Holstein-Rathlou [24]. Effect of 25 $\text{nL} \cdot \text{min}^{-1}$ microperfusion of artificial tubular fluid on proximal pressure and a neighbouring nephron's proximal pressure. **A**: shows abolishment of the TGF elicited oscillations in perfused nephron and a reduction in the amplitude of the coupled nephron. **B**: abolition of the TGF elicited oscillations in the perfused nephron and no effect on the uncoupled nephron.

2.2 MODELLING

The kidneys have been mathematically modelled at a range of levels from whole organ, to single nephron, to cellular level. Preliminary whole organ models consisted of diffusion models through a homogenous medium, whilst early single-nephron models focused on the steady state concentrating ability of the kidneys. Fairly recently, detailed, dynamic single nephron models have been coupled together to model subpopulations of nephrons. A recent mathematical model [37] simulated the myogenic response throughout the entire renal vasculature. The level of detail in these whole organ models has increased with the fairly recent advances in computing power. However, computing power has not increased enough to model the complex physiology and interactions occurring within the kidney and most of the modelling has been done in a single nephron or small group of nephrons.

While many models focus on the concentrating ability of the kidney at its transport processes the focus of this thesis is on autoregulation by the TGF mechanism. The mathematical models in the literature relevant to TGF are: glomerular, tubular, and TGF models.

The myogenic mechanism has also been extensively modelled. Current myogenic modelling research focuses on the interplay between the fast dynamics of the myogenic mechanism and the slower dynamics of the TGF mechanism. The myogenic response will not be addressed as it is not the focus of this research. For an excellent physiological discussion and mathematical model the reader is referred to Kleinstreuer [36].

2.2.1 Glomerular models

Glomerular models represent filtration at the glomerulus. Filtration is driven by the difference in hydrostatic pressure and opposed by the osmotic pressure of the large plasma proteins.

Deen et al.

The filtration model proposed by Deen et al. [15] to model the glomerulus has been widely used in the literature. The single equation comprising the glomerular model can be derived from conservation of mass in a noncompliant, reabsorbing

cylinder as

$$\frac{\mathrm{d}Q}{\mathrm{d}x} = -\frac{Sk}{L} P_{\mathrm{UF}}, \tag{2.1}$$

where Q is the volume flow, x is the spatial coordinate, S is the total surface area of the tubule, k is the membrane hydraulic permeability, L is the length of an idealised glomerulus, and P_{UF} is the net driving pressure.

P_{UF} is comprised of the hydrostatic and osmotic pressures giving

$$P_{\mathrm{UF}} = (P_{\mathrm{GC}} - P_{\mathrm{T}}) - (\pi_{\mathrm{GC}} - \pi_{\mathrm{T}}) \tag{2.2}$$

where the glomerular capillary hydrostatic pressure, P_{GC}, aids filtration and filtration is opposed by the sum of the tubule hydrostatic pressure, P_{T}, and the osmotic pressure of the large plasma proteins in the glomerulus, π_{GC}. The osmotic pressure due to ions is the same on each side of the glomerular wall, as the wall is freely permeable to ions. The osmotic pressure in Bowman's capsule, π_{T}, is zero as there are no large plasma proteins in the tubule due to the impermeability of the glomerular wall.

Combining (2.1) and (2.2) gives

$$\frac{\mathrm{d}Q}{\mathrm{d}x} = -K_{\mathrm{f}}(P_{\mathrm{GC}} - P_{\mathrm{T}} - \pi_{\mathrm{GC}}) \tag{2.3}$$

where $K_{\mathrm{f}} = Sk/L$ is the filtration coefficient. Deen et al. [15] assume P_{GC} and P_{T} are spatially constant based on experimental work from Brenner et al. [6, 7], although their paper also presented numerical results for a small pressure drop. The glomerular capillary osmotic pressure, π_{GC}, was expressed empirically as a quadratic,

$$\pi_{\mathrm{GC}} = a_1 C + a_2 C^2, \tag{2.4}$$

in the plasma protein concentration, C. The constants, a_1 and a_2, were calculated from a least squares fit to the empirical, cubic Landis-Pappenheimer equation, which was determined by fitting some experimental data. Equations (2.3) and (2.4) can be solved together for C, in closed form, after substitution of $Q = m/C$, where m, a constant, is the large plasma protein mass flow rate.

Keener and Sneyd

The filtration model of Keener and Sneyd [34] parallels the work of Deen et al. [15] except that it replaced the empirical equation for osmotic pressure in the

glomerular capillaries, (2.4), by a conservation equation. In addition, the Keener and Sneyd [34] model also describes the afferent and efferent arterioles and the renal tubule.

As the glomerulus is impermeable to large plasma proteins, conservation of protein mass gives

$$c_{\mathrm{i}} Q_{\mathrm{i}} = c q_1, \tag{2.5}$$

where $c_{\mathrm{i}} = c(0)$ and c are the inlet and spatially dependent protein concentrations, respectively, and $Q_{\mathrm{i}} = q_1(0)$ and q_1 are the inlet and spatially dependent volume flows in the glomerulus, respectively. Rearranging (2.5) for c and applying Morse's equation, $\pi_{\mathrm{c}} = RTc$, gives

$$\pi_{\mathrm{c}} = \pi_{\mathrm{i}} \frac{Q_{\mathrm{i}}}{q_1}, \tag{2.6}$$

where $\pi_{\mathrm{i}} = RTc_{\mathrm{i}}$ is the inlet osmotic pressure, R is the gas constant, and T is the temperature of the fluid. Using (2.6) for the glomerular osmotic pressure, π_{c}, in (2.3) gives

$$\frac{\mathrm{d}q_1}{\mathrm{d}x} = -K_{\mathrm{f}}(P_1 - P_2 - \pi_{\mathrm{i}} \frac{Q_{\mathrm{i}}}{q_1}) \tag{2.7}$$

that can be solved by definite integration with respect to x between $x = 0$ and $x = L$ as

$$Q_{\mathrm{e}} + \frac{\pi_{\mathrm{i}} Q_{\mathrm{i}}}{P_1 - P_2} \ln\left(\frac{(P_1 - P_2)Q_{\mathrm{e}} - \pi_{\mathrm{i}} Q_{\mathrm{i}}}{(P_1 - P_2)Q_{\mathrm{i}} - \pi_{\mathrm{i}} Q_{\mathrm{i}}}\right) = Q_{\mathrm{i}} - K_{\mathrm{f}} L \left(P_1 - P_2\right), \tag{2.8}$$

where $Q_{\mathrm{e}} = q_1(L)$ is the glomerular outflow that passes into the efferent arteriole.

The remainder of the steady state Keener and Sneyd [34] glomerular model, is comprised of mathematical descriptions of the afferent and efferent arterioles and renal tubule. These three anatomical structures are modelled using Poiseuille's law as

$$Q_{\mathrm{i}} R_{\mathrm{a}} = P_{\mathrm{a}} - P_1, \tag{2.9}$$

$$Q_{\mathrm{e}} R_{\mathrm{e}} = P_1 - P_{\mathrm{e}}, \text{ and} \tag{2.10}$$

$$Q_{\mathrm{d}} R_{\mathrm{d}} = P_2 - P_{\mathrm{d}}, \tag{2.11}$$

where R_{a}, R_{e}, and R_{d} are the resistances of the afferent arteriole, efferent arteriole, and renal tubule, respectively; P_{a}, P_1, P_2, P_{e}, and P_{d} are mean arteriole, Bowman's capsule, glomerular, efferent arteriole, and renal tubule pressures, respectively; and Q_{i}, Q_{e}, and Q_{d} are the volume flows through the afferent arteriole, efferent arteriole, and renal tubule, respectively. Completing the model, conser-

vation of flow through the glomerulus gives

$$Q_{\mathrm{d}} = Q_{\mathrm{i}} - Q_{\mathrm{e}}. \tag{2.12}$$

2.2.2 Tubular models

Modelling of the vascular system began with Euler in 1775 [65]. Since 1965 there have been several models proposed to describe 1D or 2D flows in noncompliant [4], compliant tubules [3, 53, 64, 65], or specifically in the renal tubule with its reabsorbing endothelium [28, 35, 62, 75]. Each model begins with, or derives, a simplified version of the Navier-Stokes and continuity equations under the assumptions of an incompressible Newtonian fluid. In the noncompliant models this closes the system; in the compliant models an equation describing the behaviour of the wall is necessary. The diversity in the models comes from the variety of equations of motion used for the tubule wall and from the reabsorption patterns.

A commonly used [26, 66] ordinary differential equation (ODE) tubule model is

$$\dot{P}_{\mathrm{t}} = \frac{1}{C_{\mathrm{tub}}} \left(F_{\mathrm{f}}(P_{\mathrm{t}}, r) - F_{\mathrm{reab}} - (P_{\mathrm{t}} - P_{\mathrm{d}})/R_{\mathrm{Hen}} \right), \tag{2.13}$$

where P_{t} is the spatially constant pressure in the tubule, C_{tub} is the compliance of the tubule, $F_{\mathrm{f}}(P_{\mathrm{t}}, r)$ is the single nephron glomerular filtration rate, F_{reab} is the assumed constant reabsorption in the proximal tubule, P_{d} is a distal pressure, and R_{Hen} is the resistance of the loop of Henle. This model permits a simple solution and a greater detail of analysis than the partial differential equation (PDE) models, presented next, at the cost of a more realistic solution.

Young and Marsh

The most widely used PDE tubule model is partially derived in a paper by Young and Marsh [75]. With assumptions of laminar, nonpulsatile flow in a compliant, reabsorbing, axisymmetric, cylindrical tubule, the dimensional Navier-Stokes and continuity equations give

$$\frac{\partial P}{\partial z} = -\frac{\rho}{\pi R^2}\frac{\partial Q}{\partial t} - \frac{8\eta}{\pi R^4}\hat{Q} \text{ and} \tag{2.14}$$

$$\frac{\partial Q}{\partial z} = -2\pi R \frac{\partial R}{\partial P}\frac{\partial P}{\partial t} - J_{\mathrm{v}}, \tag{2.15}$$

respectively, where P is pressure, Q is volume flow, z is the distance along the tubule from the glomerulus, t is time, R is the radius of the tubule, ρ is the fluid density, η is the dynamic fluid viscosity, and J_{v} is the rate of fluid volume reabsorption per unit time per unit distance. A third equation for the motion of the wall, given by

$$R = \gamma(P - P_{\mathrm{I}}) + r_0, \tag{2.16}$$

closes the system. γ is the compliance of the renal tubule and P_{I} is the interstitial pressure. A detailed derivation of (2.14) and (2.15), paralleling the work of Young and Marsh [75], is given in Chapter 3.

2.2.3 Tubuloglomerular feedback (TGF) models

Two main groups are responsible for the majority of dynamic TGF modelling in the last twenty years: Holstein-Rathlou, Marsh, Leyssac, and coworkers, and Layton, Moore, Pitman, and coworkers. The models of Layton et al. are simpler than the models of Holstein-Rathlou and contain only enough anatomy and physiology to maintain a degree of isomorphism to the *in vivo* system while producing sustained oscillations. Both models exhibit sustained oscillations at frequencies consistent with experimentally observed frequencies as well as experimentally observed phase lags and elicitation of sustained oscillations from microperfusion.

Holstein-Rathlou et al.

The first foray of Holstein-Rathlou and colleagues into mathematically modelling sustained oscillations attributed to the TGF mechanism was presented in Holstein-Rathlou and Leyssac [26]. Their reasonably detailed model included a model of the glomerulus based on the model of Deen et al. [15], a simple compliant compartment model for the tubule, and a second-order, flow based feedback function for the TGF mechanism given by

$$\frac{1}{\omega_n^2}\frac{\mathrm{d}^2 R_{\mathrm{AS}}}{\mathrm{d}t^2} + \frac{2\xi}{\omega_n}\frac{\mathrm{d}R_{\mathrm{AS}}}{\mathrm{d}t} + R_{\mathrm{AS}} = \Phi(F_{\mathrm{iH}}). \tag{2.17}$$

ω_{n} is the natural frequency, ξ is the dampening of the response, R_{AS} is the resistance of the afferent arteriole, and $\Phi(F_{\mathrm{iH}})$ is a logistic function that is in turn a function of the flow rate out of the loop of Henle, F_{iH}. This equation was chosen by Holstein-Rathlou and Leyssac [26] to be the simplest equation able to describe experimental results. The experimental results included: the

vascular wall contains an inertial, a viscous, and an elastic component; damped oscillations are observed for changes in transmural pressure; and the response of the vascular resistance vessels was found to correspond to a system that was at least second-order. In their model they showed that the operating point of the system needed to be on a steep section of the forcing function given by

$$\Phi(F_{\mathrm{iH}}) = R_{\mathrm{ASmax}} - \frac{\mathrm{DR}_{\mathrm{AS}}}{1 + \exp(k(F_{\mathrm{iH}} - \mathrm{tp}))}, \tag{2.18}$$

where tp is the point of inflection, k is related to the slope, R_{ASmax} is the maximum afferent resistance, and $\mathrm{DR}_{\mathrm{AS}}$ is the dynamic range of the afferent resistance. Holstein-Rathlou and Leyssac [26] showed that the sustained oscillations in their model could be abolished or the amplitude decreased by either: decreasing the slope of the feedback curve, $\Phi(F_{\mathrm{iH}})$, by decreasing k; by moving the inflection point of the curve away from the operating point by varying tp; or by varying the operating point, F_{iH}, by increasing or decreasing the flow into the system. This last simulation corresponded well with experimental observations that microperfusion could elicit or abolish the sustained oscillations.

The later 1990 model of Holstein-Rathlou and Marsh [28] is arguably one of the most physiologically realistic single nephron TGF models in the literature. Their TGF model was the first to include a detailed representation of the renal tubule, a chemically based feedback function, and an accurate modelling of the experimentally measured phase differences between pressure, flow, and NaCl concentration. This model is still current and has recently been used in another effort to understand the interactions between the myogenic response and the TGF mechanism in Marsh et al. [55]. As the work in this thesis is based so heavily on the model of Holstein-Rathlou and Marsh [28] a detailed duplication and discussion is included. The nomenclature has been modified to make it consistent with the rest of this thesis and is shown in Table 2.1.

The model of Holstein-Rathlou and Marsh [28] is comprised of three distinct sub-models: the glomerular model, the tubule model, and the TGF model. The glomerular model describes the filtration at the glomerulus and is based on the work of Deen et al. [15]. The tubule model describes the volume flow, pressure, and NaCl concentration in the renal tubule and is based on the model of Young and Marsh [75]. Finally, the TGF model describes the resistance of the afferent arteriole in the glomerular model based on the NaCl concentration at the end of the renal tubule.

Table 2.1 Holstein-Rathlou and Marsh [28] nomenclature

Independent variables		
t	s	Time
z	m	Tubular distance
Dependent variables		
$C(z,t)$	$\mathrm{mol}\cdot\mathrm{m}^{-3}$	NaCl concentration
$P(z,t)$	Pa	Fluid pressure
$Q(z,t)$	$\mathrm{m}^3\cdot\mathrm{s}^{-1}$	Volume flow
$R(z,t)$	m	Tubule radius
$R_\mathrm{A}(t)$	$\mathrm{Pa}\cdot\mathrm{s}\cdot\mathrm{m}^{-3}$	Resistance
$J_\mathrm{s}(z,C)$	$\mathrm{kg}\cdot\mathrm{s}^{-1}\cdot\mathrm{m}^{-1}$	NaCl reabsorption
$J_\mathrm{v}(z,C)$	$\mathrm{m}\cdot\mathrm{s}^{-2}$	Fluid volume reabsorption
$\xi(t)$	$\mathrm{Pa}\cdot\mathrm{s}\cdot\mathrm{m}^{-3}$	Afferent arteriole structural resistance
C_A	$\mathrm{kg}\cdot\mathrm{m}^{-3}$	Afferent arteriole protein concentration
C_E	$\mathrm{kg}\cdot\mathrm{m}^{-3}$	Efferent arteriole protein concentration
$\mathrm{Hct}_\mathrm{E}(t)$	1	Efferent arteriole haematocrit
$\Pi(t)$	Pa	Plasma oncotic pressure
Q_A	$\mathrm{m}^3\cdot\mathrm{s}^{-1}$	Afferent arteriole volume flow
Q_E	$\mathrm{m}^3\cdot\mathrm{s}^{-1}$	Efferent arteriole volume flow
P_GC	Pa	Glomerular capillary pressure
$P_\mathrm{T}(0)$	Pa	Bowman's capsule/tubule inlet pressure

Glomerular model The glomerular model describes the filtration process by which the glomerulus produces an ultrafiltrate of plasma. It is based on the filtration model of Deen et al. [15] and is comprised of six algebraic equations.

As the glomerular capillary wall is impermeable to plasma protein, protein mass is conserved throughout the glomerulus giving an expression for the single nephron filtration rate (SNGFR), $Q_\mathrm{T}(0)$, as

$$Q_\mathrm{T}(0) = \left(1 - \frac{C_\mathrm{A}}{C_\mathrm{E}}\right) Q_\mathrm{A}, \tag{2.19}$$

where the protein concentration varies from C_A at the start of the glomerulus to C_E at the end of glomerulus and Q_A is the volume flow through the afferent arteriole. By considering Poiseuille's law in the afferent arteriole a relationship between Q_A and the pressure drop, $P_\mathrm{Art} - P_\mathrm{GC}$, through the arteriole can be shown to be

$$\frac{Q_\mathrm{A}}{1 - \mathrm{Hct}_\mathrm{A}} = \frac{P_\mathrm{Art} - P_\mathrm{GC}}{R_\mathrm{A}}, \tag{2.20}$$

where the pressure drops from mean arterial pressure, P_Art, to glomerular capillary pressure, P_GC. R_A is the resistance of the afferent arteriole and Hct_A is the

haematocrit at the afferent arteriole. The resistance of the afferent arteriole can be expressed as

$$R_{\mathrm{A}} = \xi \exp(\Lambda \mathrm{Hct}_{\mathrm{A}}) \tag{2.21}$$

[28], where ξ is the structural resistance of the afferent arteriole, and Λ is a constant. The resistance of the efferent arteriole, R_{E}, is expressed analogously to (2.21), where the haematocrit in the efferent arteriole, $\mathrm{Hct}_{\mathrm{E}}$, is expressed as

$$\mathrm{Hct}_{\mathrm{E}} = \frac{1}{1 + \frac{C_{\mathrm{A}}}{C_{\mathrm{E}}} \frac{1-\mathrm{Hct}_{\mathrm{A}}}{\mathrm{Hct}_{\mathrm{A}}}} \tag{2.22}$$

by considering conservation of blood cell mass through the glomerulus. The glomerular pressure, P_{GC}, can be expressed as

$$P_{\mathrm{GC}} = R_{\mathrm{E}} \left(\frac{Q_{\mathrm{A}}}{1 - \mathrm{Hct}_{\mathrm{A}}} - Q_{\mathrm{T}}(0) \right) + \frac{Q_{\mathrm{A}} R_{\mathrm{PC}}}{1 - \mathrm{Hct}_{\mathrm{A}}} \tag{2.23}$$

by applying Poiseuille's law between the glomerular capillaries and the venous bed. It is assumed that the total SNGFR, $Q_{\mathrm{T}}(0)$, is reabsorbed into the efferent blood flow that then passes through a distal resistance, R_{PC}, to the venous beds where the pressure is assumed to be zero [28]. The filtration model of Deen et al. [15], expressly

$$\int_{C_{\mathrm{A}}}^{C_{\mathrm{E}}} \frac{1}{C^2 (P_{\mathrm{GC}} - P_{\mathrm{T}}(0) - \Pi(C))} dC = \frac{K_{\mathrm{f}}}{Q_{\mathrm{A}} C_{\mathrm{A}}}, \tag{2.24}$$

completes the model, where $P_{\mathrm{T}}(0)$ is the spatially constant pressure in Bowman's capsule, $\Pi(C)$ is the osmotic pressure exerted by the plasma proteins across the glomerular capillary wall, and K_{f} is the capillary filtration rate. The osmotic pressure, $\Pi(C)$, is given a simplified version of the empirical Landis-Pappenheimer equation

$$\Pi(C) = aC + bC^2, \tag{2.25}$$

where a and b are constants and C is the plasma protein concentration.

The glomerular model provides two of the upstream boundary conditions for the tubule model: $Q_{\mathrm{T}}(0)$ and $P_{\mathrm{T}}(0)$. The glomerular model also effects the TGF mechanism through the afferent arteriole structural resistance, ξ, in (2.21).

Tubule model The tubule model describes volume flow, Q_{T}; pressure, P_{T}; and NaCl concentration, C_{S}, in the renal tubule through three coupled PDEs:

$$\frac{\partial P_{\mathrm{T}}}{\partial z} = -\frac{\rho}{\pi R^2}\frac{\partial Q_{\mathrm{T}}}{\partial t} - \frac{8\mu}{\pi R^4}Q_{\mathrm{T}}, \tag{2.26}$$

$$\frac{\partial Q_{\mathrm{T}}}{\partial z} = -2\pi R\frac{\partial R}{\partial P_{\mathrm{T}}}\frac{\partial P_{\mathrm{T}}}{\partial t} - J_{\mathrm{V}}, \text{ and} \tag{2.27}$$

$$\frac{\partial (AC_{\mathrm{S}})}{\partial t} = -\frac{\partial (Q_{\mathrm{T}}C_{\mathrm{S}})}{\partial z} - J_{\mathrm{S}}. \tag{2.28}$$

t is time, z is the spatial coordinate along the tubule, J_{V} and J_{S} are the volume/water and NaCl fluxes across the tubule wall, respectively, A is the cross-sectional area, ρ is the density of the tubule fluid, μ is the dynamic viscosity, and R is the radius of the tubule.

(2.26) and (2.27) are derived from the incompressible Navier-Stokes and continuity equations in an inertial reference frame and have been used previously to model the renal tubule system by Young and Marsh [75]. In the derivation several terms can be shown to be small through a nondimensionalisation of the system and Poiseuille flow is assumed removing the dependence on the radial coordinate. Equation (2.28) is derived from conservation of solute mass in a reabsorbing cylinder.

The radius of the tubule is assumed to be a function of the pressure difference across the tubular wall, $P_{\mathrm{T}} - P_{\mathrm{I}}$, giving

$$R(P) = \gamma\,(P_{\mathrm{T}} - P_{\mathrm{I}}) + R_0, \tag{2.29}$$

where P_{I} is the interstitial pressure, R_0 is the radius when the transmural pressure is zero, and γ is the compliance of the tubule. (2.29) has been used previously in Young and Marsh [75] and in a detailed mathematical paper by Sherwin et al. [65], except that the constants are in terms of the properties of the tubule wall. Equating (2.29) and the corresponding expression from Sherwin et al. [65], derived from Laplace's law, gives an expression for the compliance, $\gamma = (1-\nu^2)R_0^2/(h_0E)$, where h_0 is the vessel-wall thickness, E is Young's modulus, and ν is Poisson's ratio.

Tubular fluid reabsorption, J_{v}, is different for each section of the tubule because of the different transport properties. In the proximal tubule J_{v} is assumed to be an exponentially decaying function of distance to correspond with experimental observations [28]. In the descending limb of the loop of Henle the volume flux is governed by osmotic forces and the ascending limb is water impermeable

giving

$$J_{\mathrm{v}}(z) = \begin{cases} \kappa \exp(-\theta z) & 0 \leq z < z_{\mathrm{p}}, \\ -L_{\mathrm{v}} n_{\mathrm{s}} (C_{\mathrm{S}} - C_{\mathrm{I}}) & z_{\mathrm{p}} \leq z < z_{\mathrm{d}}, \\ 0 & z_{\mathrm{d}} \leq z < L, \end{cases} \tag{2.30}$$

where z_{p}, z_{d}, and L are the spatial coordinates of the end of the proximal tubule, descending limb, and ascending limb, respectively; θ and κ are constants describing the exponentially decaying flow in the proximal tubule; and the product $L_{\mathrm{v}} n_{\mathrm{s}}$ describes the water permeability of the descending limb. The NaCl concentration of the interstitial fluid, C_{I}, varies linearly from 150 $\mathrm{mmol} \cdot \mathrm{L}^{-1}$ at the end of the proximal tubule, $z = z_{\mathrm{p}}$, to 300 $\mathrm{mmol} \cdot \mathrm{L}^{-1}$ at the bend on the loop of Henle, $z = z_{\mathrm{d}}$, back to 150 $\mathrm{mmol} \cdot \mathrm{L}^{-1}$ at the end of the ascending limb, $z = L$.

NaCl reabsorption, J_{s}, is also different for each section of the tubule and is defined in a piecewise manner. In the proximal tubule the NaCl concentration does not vary because the solute and volume fluxes are matched. Holstein-Rathlou and Marsh [28] chose not to model the NaCl concentration in the proximal tubule as it remains spatially constant, which is valid if the inlet NaCl concentration is constant. In the descending limb of the loop of Henle NaCl reabsorption is assumed to be proportional to the NaCl concentration gradient across the tubule wall and is modelled using Fick's law. This term is also used in the ascending limb in addition to a pump term to model the active transport of NaCl giving

$$J_{\mathrm{s}}(z) = \begin{cases} L_{\mathrm{s}}(C - C_{\mathrm{I}}) & z_{\mathrm{p}} \leq z < z_{\mathrm{d}}, \\ L_{\mathrm{s}}(C - C_{\mathrm{I}}) + \frac{V_{\max} C}{K_{\mathrm{m}} + C} & z_{\mathrm{d}} \leq z < L, \end{cases} \tag{2.31}$$

where L_{s} is the solute permeability of the loop of Henle, C_{I} is the interstitial solute NaCl concentration, $V_{\max}$ is the maximum solute transport rate, and K_{m} is the half maximal solute NaCl concentration.

The outlet pressure, $P(L)$, is expressed by an implicit empirical relationship,

$$P(L) = \frac{Q(L)}{\left(\alpha P(L) + \beta\right)^4}, \tag{2.32}$$

used previously by [64], where α and β are constants.

The tubule model gives the NaCl concentration at the macula densa, $C_{\mathrm{S(md)}}$ that is the input to the TGF model.

Tubuloglomerular feedback (TGF) model The structural resistance of the afferent arteriole is modelled by the second-order differential equation

$$\frac{1}{\omega^2}\frac{\mathrm{d}^2\xi}{\mathrm{d}t^2} + \frac{2\zeta}{\omega}\frac{\mathrm{d}\xi}{\mathrm{d}t} + \xi = \phi(C_{\mathrm{S(md)}}), \tag{2.33}$$

where ω is the natural frequency and ζ is the damping coefficient. The homogenous version of (2.33), namely $\phi(C_{\mathrm{S(md)}}) = 0$, has eigenvalues $\lambda = -\zeta\omega \pm \omega\sqrt{\zeta^2 - 1}$. Holstein-Rathlou and Marsh [28] use ζ=0.9 and ω=0.2 rad $\cdot\, \mathrm{s}^{-1}$ giving two complex eigenvalues with negative real part. The homogenous equation is inherently oscillatory and will exhibit damped oscillations at $\omega\sqrt{\zeta^2 - 1} \approx 0.0139$ Hz, where $\omega = 2\pi f$.

The forcing term, $\phi(C_{\mathrm{S(md)}})$, is given by

$$\phi(C_{\mathrm{S(md)}}) = \xi_{\max} - \frac{\psi}{1 + \exp(k(C_{\mathrm{S(md)}} - C_{\frac{1}{2}}))} \tag{2.34}$$

where $\xi_{\max}$ is the maximum structural resistance of the afferent arteriole, ψ is the range, $C_{\frac{1}{2}}$ is the inflection point of the curve, $C_{\mathrm{S(md)}}$ is the NaCl concentration at the macula densa, and k is related to the slope of the curve and is commonly referred to in the literature as the gain.

Layton et al.

The modelling approach taken by Layton and colleagues is, in their own words, minimalist in that it includes only the features necessary to provide sustained oscillation while maintaining good structural isomorphism with the TGF system. Their base model, presented in Layton et al. [42], used a PDE to model the NaCl concentration in the ascending limb, given by

$$\frac{\partial C}{\partial t} + F(C(1, t-\tau))\frac{\partial C}{\partial x} = -J(C, C_{\mathrm{e}}) \tag{2.35}$$

where C is the NaCl concentration, x and t are the spatial and temporal coordinates, respectively, and $J(C, C_{\mathrm{e}})$ is the NaCl flux that is a function of the temporally constant interstitial NaCl concentration, C_{e}. $F(C(1, t-\tau))$ represents the fluid flow into the ascending limb that is a function of the NaCl concentration at the macula densa, $z = 1$, at an earlier time, $t - \tau$. The delay, τ, models the time delay of a signal at the macula densa affecting the flow into the ascending limb due to the transmission time between the macula densa and the afferent

arteriole, the response time of the afferent arteriole, and the delay caused by tubular compliance. The ascending limb inlet flow, F, is assumed to follow a logistic curve,

$$F(C_{\mathrm{MD}}) = 1 + K_1 \tanh(K_2(C_{\mathrm{op}} - C_{\mathrm{MD}})), \tag{2.36}$$

due to strong experimental evidence. This model is still current and has recently been used by this group to model two coupled nephrons in Layton et al. [41].

Chapter 3

NEPHRON MODEL

The main focus of this chapter is to investigate the oscillatory behaviour of the tubuloglomerular feedback (TGF) mechanism through a mathematical model. The mathematical TGF model of Holstein-Rathlou and Marsh [28] uses a second-order differential equation to describe these oscillations. Using an inherently oscillatory model masks the fundamental cause and physiological significance of this behaviour. Throughout this thesis, a first-order differential equation is used, representing simple reversion dynamics of the afferent arteriole resistance, R_{a}, to the target resistance, R_{a}^{*}. In contrast to the system presented in [28], this equation alone is not inherently oscillatory. Hence, any oscillatory behaviour that does occur will result from the interaction of this feedback mechanism with some other feature of the model, such as the delay between changes in the resistance of the afferent arteriole and changes in sodium chloride (NaCl) concentration at the macula densa. The results show that tubular compliance is an important parameter in this study and that it is necessary for sustained oscillations.

3.1 MODEL

This section primarily consists of a derivation of the model used by Holstein-Rathlou and Marsh [28], although some modifications have been made and will be highlighted where appropriate. The important difference between the analysis of [28] and the current work is the TGF feedback model. Holstein-Rathlou and Marsh [28] used a second-order differential equation to describe the reversion of the resistance of the afferent arteriole, R_{a}, to some target resistance. This equation has a characteristic frequency like all second-order, linear differential equations with complex eigenvalues. This was chosen by [28] to match the experimentally observed time scale of the TGF mechanism, approximately 30 s.

The single nephron TGF model presented here consists of three coupled sub-models: the glomerular model, the tubular model, and the TGF model. A schematic diagram of the glomerular, tubular, and TGF models is shown in Figure 3.1. The glomerular model was from Keener and Sneyd [34], the tubular model was from Young and Marsh [75], and they were coupled using the approach from [28]. The model is comprised of three partial differential equations (PDEs), five algebraic equations, and one temporal ordinary differential equation (ODE).

A spatial, one-dimensional diffusion model that relates the flow across the glomerular wall to the pressure difference was used for the glomerular model, based on the work of Keener and Sneyd [34]. The total flow across the glomerular wall, Q_{d}, and the pressure in Bowman's capsule, P_{b}, from the glomerular model provide the upstream boundary conditions for the tubular model.

A spatiotemporal model that relates the pressure, $P(t, z)$; flow, $Q(t, z)$; and NaCl concentration, $C(t, z)$, in the renal tubule was used for the tubular model, based on the work of Holstein-Rathlou and Marsh [28]. Pressure, flow, and NaCl concentration were functions of time, t, and distance along the tubule from the start of the proximal tubule, z. The tubular distance, z, was nondimensionalised with respect to the distance from the start of the proximal tubule to the macula densa, namely z=1 at the macula densa. The tubule was modelled up to the macula densa where the distal boundary conditions were applied. This point was chosen as the signal to the TGF mechanism is the NaCl concentration at the macula densa. Although changes in pressure or resistance distal to the macula densa affect the characteristics of the flow upstream, this was assumed to be applied through the distal pressure boundary condition.

The TGF model describes the negative feedback mechanism by which the NaCl concentration at the macula densa, $C(t, 1)$, which was itself determined by the tubule model, modulates the resistance of the afferent arteriole, R_{a}.

The aim of the work presented in this chapter was to determine whether sustained oscillations exist in this model and, if so, to identify some of the physiological factors that contribute to them.

3.1.1 Glomerular model

The complex geometry of the glomerular capillary bed can be represented as two parallel one-dimensional tubules and modelled using simple filtration [15, 34]. The glomerular model of Keener and Sneyd [34] is used in this thesis; for more

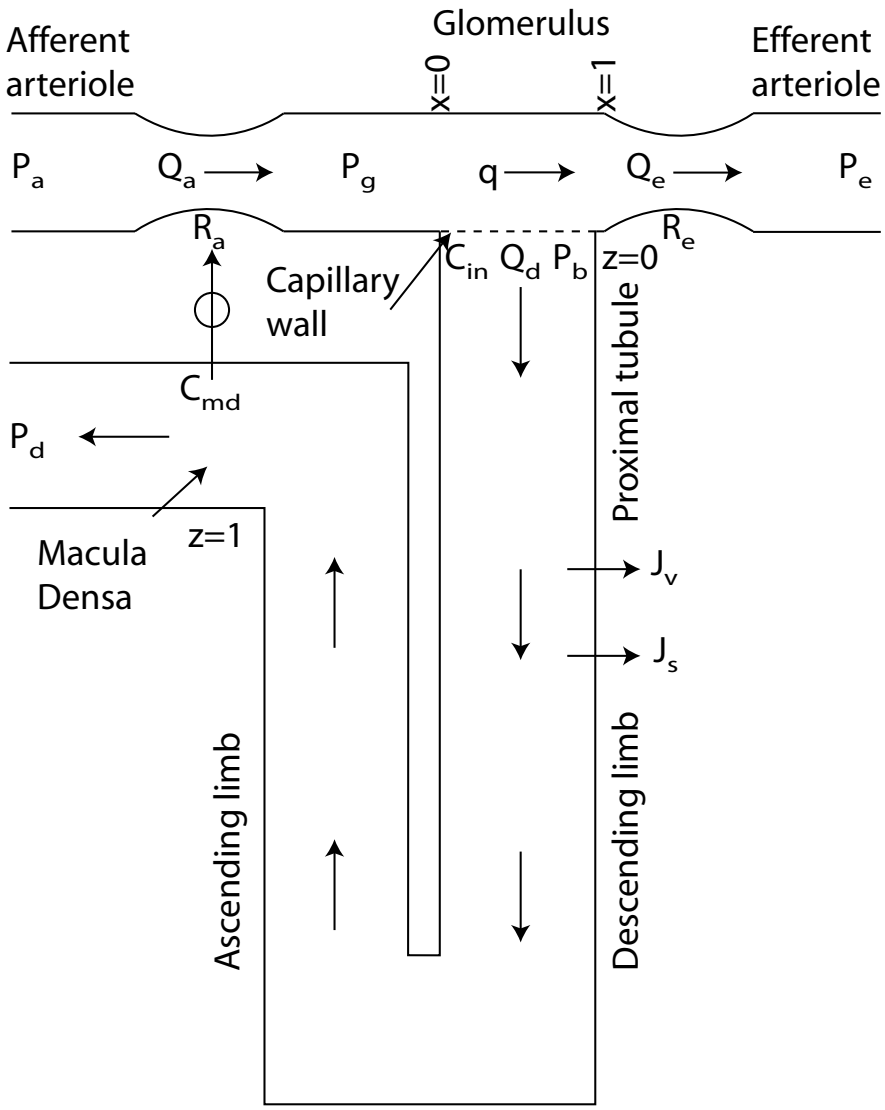

Figure 3.1 Model diagram: whole blood passes into the afferent arteriole, with resistance R_{a}, at pressure P_{a}, and volume flow rate Q_{a}. The pressure in both glomerulus, P_{g}, and Bowman's capsule, P_{b}, is assumed to be constant throughout. Fluid is driven across the capillary wall by the hydrostatic pressure difference, $P_{\mathrm{g}} - P_{\mathrm{b}}$, and by the colloid osmotic pressure difference created by the size-selective and charge-selective properties of the wall. The sum of the flow across the capillary wall is the single nephron glomerular filtration rate (SNGFR), Q_{d}. The volume flow out of the glomerulus through the efferent arteriole, Q_{e}, is restricted by the resistance of the efferent arteriole, R_{e}. P_{e} and P_{d} are the pressure downstream of the efferent arteriole and at the macula densa (MD), respectively. NB: this model diagram is not drawn to scale. Figure 1.2 is more anatomically realistic.

Table 3.1 Nomenclature for the variables used in this chapter. Primes denote a dimensional variable.

Symbol	Value/units	Description
Subscripts		
a		Afferent arteriole
e		Efferent arteriole
g		Glomerulus
b		Bowman's capsule
Independent variables		
$t' = t_{\text{ref}} t$	s	Time
$z' = Lz$	m	Tubular distance
x	m	Glomerular distance
Dependent variables		
$C'(t,z) = C(t,z) C_{\text{ref}}$	$\text{mol} \cdot \text{m}^{-3}$	NaCl concentration
$P'(t,z) = P(t,z) P_{\text{ref}}$	Pa	Fluid pressure
$Q'(t,z) = Q(t,z) Q_{\text{ref}}$	$\text{m}^3 \cdot \text{s}^{-1}$	Volume flow
$R'(t) = R(t) R_{\text{ref}}$	$\text{Pa} \cdot \text{s} \cdot \text{m}^{-3}$	Resistance
Auxiliary variables		
$J'_{\text{s}}(z, C(t,z))$	$\text{kg} \cdot \text{s}^{-1} \cdot \text{m}^{-1}$	NaCl flux
$J'_{\text{v}}(z, C(t,z))$	$\text{m} \cdot \text{s}^{-2}$	Fluid flux

details refer to page 25. The model of Keener and Sneyd [34] is similar to the earlier glomerular model of Deen et al. [15] except that conservation of protein mass was used to represent colloid osmotic pressure in terms of volume flow instead of a variant of the empirical Landis-Pappenheimer equation. The transit time in the glomerular capillaries is an order of magnitude smaller than any other time dynamics considered in the single nephron model [28] and the glomerular variables are hence assumed to be in a pseudo-steady state. The pressure in the glomerulus, P_{g}, and in Bowman's capsule, P_{b}, are assumed to be spatially constant as the change in pressure in each is small compared to the pressure drop in the afferent and efferent arterioles [34]. Refer to Table 3.1 for the nomenclature.

Filtration across the capillary wall is proportional to the sum of the hydrostatic and oncotic pressure differences with proportionality constant K'_{f} [15]. This filtration causes a corresponding drop in nondimensional glomerular volume flow, q', with respect to the nondimensional distance, x', from the glomerulus inlet and was modelled [34] by

$$\frac{\text{d}q'}{\text{d}x'} = -K'_{\text{f}} \left(P'_{\text{g}} - P'_{\text{b}} - \pi'_{\text{a}} \frac{Q'_{\text{a}}}{q'} \right), \tag{3.1}$$

where Q'_{a} is the inlet volume flow, P'_{g} and P'_{b} are the temporally variable but spatially constant pressures in the glomerulus and Bowman's capsule, and π'_{a} is the osmotic pressure at the inlet to the glomerulus. A schematic diagram with the relevant variables is shown in Figure 3.1. The last term on the right hand side of (3.1) represents the osmotic pressure from the large plasma proteins and was derived in more detail on page 25. In this thesis, primes denote a nondimensional variable or constant. Integration of (3.1) between x'=0 and x'=1 (the length of the glomerulus) gives

$$Q'_{\mathrm{e}} + \frac{\pi'_{\mathrm{a}} Q'_{\mathrm{a}}}{P'_{\mathrm{g}} - P'_{\mathrm{b}}} \ln\left(\frac{\left(P'_{\mathrm{g}} - P'_{\mathrm{b}}\right) Q'_{\mathrm{e}} - \pi'_{\mathrm{a}} Q'_{\mathrm{a}}}{\left(P'_{\mathrm{g}} - P'_{\mathrm{b}}\right) Q'_{\mathrm{a}} - \pi'_{\mathrm{a}} Q'_{\mathrm{a}}}\right) = Q'_{\mathrm{a}} - K'_{\mathrm{f}}\left(P'_{\mathrm{g}} - P'_{\mathrm{b}}\right), \tag{3.2}$$

an implicit relation between the volume flow through the afferent arteriole, $Q'_{\mathrm{a}} = q'(0)$, and the efferent arteriole, $Q'_{\mathrm{e}} = q'(1)$.

Applying Poiseuille's law (i.e., flow×resistance=pressure drop) in the afferent and efferent arterioles [34] gives

$$\begin{aligned} Q'_{\mathrm{a}} R'_{\mathrm{a}} &= P'_{\mathrm{a}} - P'_{\mathrm{g}} \text{ and} \\ Q'_{\mathrm{e}} R'_{\mathrm{e}} &= P'_{\mathrm{g}} - P'_{\mathrm{e}}, \end{aligned} \tag{3.3}$$

where R'_{a} and R'_{e} are the resistances of the afferent and efferent arterioles; P'_{a}, P'_{g}, and P'_{e} are mean arteriole, glomerular, and efferent arteriole pressures; and Q'_{a} and Q'_{e} are the volume flows through the afferent arteriole and efferent arteriole.

Completing the model, conservation of flow through the glomerulus [34] gives

$$Q'_{\mathrm{d}} = Q'_{\mathrm{a}} - Q'_{\mathrm{e}}. \tag{3.4}$$

3.1.2 Tubule model

The tubule model used in this thesis is based on the model of Young and Marsh [75]. The simplification of the Navier-Stokes and continuity equations presented in [75] was simplified by introducing typical numerical values earlier in the nondimensionalisation. Young and Marsh [75] retained the $\partial Q/\partial t$ term, despite noting that it is six orders of magnitude smaller than the other terms. Physiologically this means that the flow equilibrates much faster than other variables in the system. It was assumed that this term was negligible to simplify the solution process.

Navier-Stokes Equation

The incompressible Navier-Stokes equation in an inertial, cartesian reference frame with constant viscosity and no body forces is

$$\frac{\partial \mathbf{u}}{\partial t} + \mathbf{u} \cdot \nabla \mathbf{u} + \frac{\nabla P}{\rho} = \nu \nabla^2 \mathbf{u} \tag{3.5}$$

[72], where t is time, P is pressure, $\mathbf{u}$ is velocity, ρ is density, and $\nu = \mu/\rho$ is kinematic viscosity. Assuming axisymmetric flow the components of (3.5) in cylindrical coordinates are

$$\frac{\partial u_\mathrm{z}}{\partial t} + u_\mathrm{r}\frac{\partial u_\mathrm{z}}{\partial r} + u_\mathrm{z}\frac{\partial u_\mathrm{z}}{\partial z} + \frac{1}{\rho}\frac{\partial P}{\partial z} = \nu\left(\frac{1}{r}\frac{\partial}{\partial r}\left(r\frac{\partial u_\mathrm{z}}{\partial r}\right) + \frac{\partial^2 u_\mathrm{z}}{\partial z^2}\right) \text{ and} \tag{3.6}$$

$$\frac{\partial u_\mathrm{r}}{\partial t} + u_\mathrm{r}\frac{\partial u_\mathrm{r}}{\partial r} + u_\mathrm{z}\frac{\partial u_\mathrm{r}}{\partial z} + \frac{1}{\rho}\frac{\partial P}{\partial r} = \nu\left(\frac{1}{r}\frac{\partial}{\partial r}\left(r\frac{\partial u_\mathrm{r}}{\partial r}\right) - \frac{u_\mathrm{r}}{r^2} + \frac{\partial^2 u_\mathrm{r}}{\partial z^2}\right), \tag{3.7}$$

where r and z denote the radial and axial coordinates and u_r and u_z denote the flow velocity in those directions. Several terms in (3.6) and all but one term in (3.7) are shown to be relatively small through a nondimensionalisation of the system. To this end, the system was nondimensionalised in the following way:

$$r = r_0 r',\ z = L z',\ u_\mathrm{z} = u_0 u_\mathrm{z}',\ u_\mathrm{r} = v_0 u_\mathrm{r}',\ P = P_\mathrm{ref} P',\ \text{and } t = \frac{L}{u_0} t', \tag{3.8}$$

where r_0 was the radius of the tubule, L was the length of the tubule, u_0 and v_0 were typical flow velocities in the axial and radial directions, and P_ref was a typical pressure. Time was nondimensionalised with respect to the tubule transit time at typical axial flow velocity u_0. Substituting the nondimensional variables defined in (3.8) into (3.6) and (3.7) gives

$$\begin{aligned}\frac{\partial u_\mathrm{z}'}{\partial t'} + \frac{v_0 L}{u_0 r_0} u_\mathrm{r}'\frac{\partial u_\mathrm{z}'}{\partial r'} + u_\mathrm{z}'\frac{\partial u_\mathrm{z}'}{\partial z'} + \frac{P_\mathrm{ref}}{\rho u_0^2}\frac{\partial P'}{\partial z'} \\ = \frac{\nu L}{r_0^2 u_0}\frac{1}{r'}\frac{\partial}{\partial r'}\left(r'\frac{\partial u_\mathrm{z}'}{\partial r'}\right) + \frac{\nu}{u_0 L}\frac{\partial^2 u_\mathrm{z}'}{\partial z'^2} \text{ and}\end{aligned} \tag{3.9}$$

$$\begin{aligned}\frac{\partial u_\mathrm{r}'}{\partial t'} + \frac{v_0 L}{u_0 r_0} u_\mathrm{r}'\frac{\partial u_\mathrm{r}'}{\partial r'} + u_\mathrm{z}'\frac{\partial u_\mathrm{r}'}{\partial z'} + \frac{P_\mathrm{ref} L}{\rho r_0 v_0 u_0}\frac{\partial P'}{\partial r'} \\ = \frac{\nu L}{r_0^2 u_0}\frac{1}{r'}\frac{\partial}{\partial r'}\left(r'\frac{\partial u_\mathrm{r}'}{\partial r'}\right) - \frac{\nu L}{r_0^2 u_0}\frac{u_\mathrm{r}'}{r'^2} + \frac{\nu}{L u_0}\frac{\partial^2 u_\mathrm{r}'}{\partial z'^2}.\end{aligned} \tag{3.10}$$

The ratio of the velocities u_0 and v_0 were assumed to be equal to the ratio of the characteristic lengths L and r_0 [3]. Substituting the typical values from Table 3.2

Table 3.2 Constants and typical values are taken directly from Young and Marsh [75] and converted to SI units. Typical flow velocities in the axial and radial directions are derived from the nondimensionalisation equations and typical values from Young and Marsh [75].

Constants [75]		
Density	ρ	1000 $(\mathrm{kg}\cdot\mathrm{m}^{-3})$
Kinematic viscosity	ν	7.2×10^{-7} $(\mathrm{m}^2\cdot\mathrm{s}^{-1})$
Typical values [75]		
Flow Rate	Q_{ref}	5.833×10^{-13} $(\mathrm{m}^3.\mathrm{s}^{-1})$
Pressure	P_{ref}	1.333×10^{3} (Pa)
Radius	r_0	1×10^{-5} (m)
Total Length	L	1.8×10^{-2} (m)
Derived values		
Axial flow velocity	$u_0 = Q_{\mathrm{ref}}/(\pi r_0^2)$	$1.85\times10^{-3}(\mathrm{m}\cdot\mathrm{s}^{-1})$
Radial flow velocity	$v_0 = u_0 r_0/L$	$2.1\times10^{-6}(\mathrm{m}\cdot\mathrm{s}^{-1})$

into the coefficients of (3.10) gives:

$$\frac{v_0 L}{u_0 r_0} = 1,\ \frac{P_{\mathrm{ref}}}{\rho u_0^2} = 9.67\times10^4,\ \frac{\nu L}{r_0^2 u_0} = 3.49\times10^4,\ \frac{\nu}{L u_0} = 1.08\times10^{-2},$$
$$\text{and } \frac{P_{\mathrm{ref}} L}{\rho r_0 v_0 u_0} = 3.13\times10^{11}. \quad (3.11)$$

The two largest terms in (3.9) were approximately the same size and were larger than the remaining terms by approximately four orders of magnitude. The largest term in (3.10) was approximately seven orders of magnitude larger than the other terms. Removing the comparatively small terms from (3.9) and (3.10) gives

$$\frac{\partial P'}{\partial z'} = \left(\frac{\mu L u_0}{P_{\mathrm{ref}} r_0^2}\right)\frac{1}{r'}\frac{\partial}{\partial r'}\left(r'\frac{\partial u_{\mathrm{z}}'}{\partial r'}\right) \text{ and} \quad (3.12)$$

$$\frac{\partial P'}{\partial r'} = 0. \quad (3.13)$$

(3.13) asserts that the pressure was constant radially [3], which also means that $\partial P'/\partial z'$ is independent of r'. Equation (3.12) can be solved for u_{z}' by integrating with respect to r, giving

$$u_{\mathrm{z}}' = \frac{P_{\mathrm{ref}} r_0^2}{4\mu L u_0}\frac{\partial P'}{\partial z'}(r'^2 - R'^2). \quad (3.14)$$

The constants of integration are solved for using the fact that u_{z}' is bounded as $r' \to 0$ and the boundary condition $u_{\mathrm{z}}'\Big|_{r'=R'} = 0$. Substituting (3.14) into the

definition of volume flow, Q', gives

$$Q' = 2\int_0^{R'} u'_{\mathrm{z}} r' \mathrm{d}r' \tag{3.15}$$

$$= \frac{P_{\mathrm{ref}} r_0^2}{2\mu L u_0} \frac{\partial P'}{\partial z'} \int_0^{R'} (r'^2 - R'^2) \mathrm{d}r' \tag{3.16}$$

$$= -\frac{P_{\mathrm{ref}} r_0^2}{8\mu L u_0} \frac{\partial P'}{\partial z'} R'^4. \tag{3.17}$$

Rearrangement of (3.17) after substitution of $u_0 = Q_{\mathrm{ref}}/(\pi r_0^2)$ from Table 3.2 gives

$$\frac{\partial P'}{\partial z'} = -\left(\frac{8\mu L Q_{\mathrm{ref}}}{\pi P_{\mathrm{ref}} r_0^4}\right) \frac{Q'}{R'^4}. \tag{3.18}$$

The equation derived by Young and Marsh [75],

$$\frac{\partial P}{\partial z} = -\frac{\rho}{\pi R^2} \frac{\partial Q}{\partial t} - \frac{8\mu}{\pi} \frac{Q}{R^4}, \tag{3.19}$$

that has been used since in papers such as Sakai et al. [64], Holstein-Rathlou and Marsh [28], and Marsh et al. [55], differs from (3.18) in that it contains an extra term, $\partial Q/\partial t$. As noted in Young and Marsh [75] this term is six orders of magnitude smaller than the other terms in the equation. Physiologically this means that the flow equilibrates much more quickly than the pressure or NaCl concentration, and can be considered to be in a pseudo-steady state. Numerically solving the tubule model with and without $\partial Q/\partial t$ term yielded little difference in the solution and it was removed from the model. Leaving this term in the system destabilised the numerical solution process and special care was taken to ensure numerical stability. By examining the single sided finite difference scheme of Young and Marsh [75] it appears they also faced this problem, which they overcame by using an implicit numerical scheme.

Continuity equation

The continuity equation for an axisymmetric, incompressible flow in cylindrical coordinates is

$$\frac{1}{r}\frac{\partial}{\partial r}(r u_{\mathrm{r}}) + \frac{\partial u_{\mathrm{z}}}{\partial z} = 0 \tag{3.20}$$

[3]. Using the nondimensional quantities defined in (3.8) transforms (3.20) into

$$\frac{1}{r'}\frac{\partial}{\partial r'}(r' u'_{\mathrm{r}}) + \frac{\partial u'_{\mathrm{z}}}{\partial z'} = 0, \tag{3.21}$$

after applying $u_0 r_0 = v_0 L$ as was used in the nondimensionalisation of the Navier-Stokes equations. Multiplying (3.21) through by r' and integrating between $r' = 0$ and $r' = R'$ gives

$$\int_0^{R'} \frac{\partial}{\partial r'} \left(r' u'_{\mathrm{r}}\right) \mathrm{d}r' + \int_0^{R'} r' \frac{\partial u'_{\mathrm{z}}}{\partial z'} \mathrm{d}r' = 0. \tag{3.22}$$

The first term of (3.22) was integrated using the fundamental theorem of calculus while the second term can be written in terms of Q by swapping the order of differentiation and integration using Leibniz's rule, giving

$$\left[r' u'_{\mathrm{r}}\right]_{r'=0}^{r'=R'} + \frac{\partial}{\partial z'} \left(\int_0^{R'} r' u'_{\mathrm{z}} \mathrm{d}r' \right) - \frac{\partial R'}{\partial z'} \left[r' u'_{\mathrm{z}}\right]_{r'=0}^{r'=R'} = 0 \tag{3.23}$$

$$\implies R' u'_{\mathrm{r}'}|_{r'=R'} + \frac{1}{2} \frac{\partial Q'}{\partial z'} - R' \frac{\partial R'}{\partial z'} u'_{\mathrm{z}}|_{r'=R'} = 0 \tag{3.24}$$

where $Q' = \int_0^{R'} 2r' u'_z dr'$ was the volume flow. The first term on the left hand side of (3.24) was written as the tubule radius, R, multiplied by the sum of two velocities: the velocity of the wall and the velocity of the fluid passing axisymmetrically through the tubule wall, $F(z)$. This gives

$$2R' \frac{\partial R'}{\partial t'} + \frac{\partial Q'}{\partial z'} - 2R' \frac{\partial R'}{\partial z'} u'_{\mathrm{z}}|_{r'=R'} = -2R' F(z'). \tag{3.25}$$

(3.25) was further simplified using the no slip boundary condition, i.e., $u'_{\mathrm{z}}|_{r'=R'} = 0$, and by using the fact that the right hand side can be interpreted as the volume flux, $J'_{\mathrm{v}} = 2R' F(z')$, through the wall, giving

$$2R' \frac{\partial R'}{\partial t'} + \frac{\partial Q'}{\partial z'} = -J'_{\mathrm{v}}. \tag{3.26}$$

Wall model

An equation describing the motion of the tubule wall is necessary to close the system described by (3.18) and (3.26). The radius of the tubule, R', was expressed [28] in terms of the transmural pressure difference as

$$R' = \gamma' \left(P' - P'_{\mathrm{I}}\right) + 1, \tag{3.27}$$

where $\gamma' = \gamma P_{\mathrm{ref}}/r_0$ is the compliance of the tubule and P'_{I} is the interstitial pressure. The relationship given by (3.27) is equivalent to the pressure area re-

lationship used by Sherwin et al. [65] in a vascular network model and is derived using Laplace's law. Substituting $\frac{\partial R'}{\partial t'} = \gamma' \frac{\partial P'}{\partial t'}$, which was derived by differentiating (3.27) with respect to time, into (3.26) gives

$$2\gamma' R' \frac{\partial P'}{\partial t'} + \frac{\partial Q'}{\partial z'} = -J'_{\mathrm{v}}. \tag{3.28}$$

Volume flux (J'_{v})

In the proximal tubule, fluid volume reabsorption is modelled using a function that decays exponentially with respect to z, as early segments of the proximal tubule absorb fluid more vigorously than later segments [28]. A more realistic model, which was not implemented here, would be to use a osmotic term, as water follows the active transport of NaCl across the tubule wall. In the descending limb, volume reabsorption is governed by osmotic forces. Osmosis is modelled as being proportional to the difference between the luminal NaCl concentration, C, and the interstitial NaCl concentration, C_{I}. There is no volume reabsorption in the ascending limb [41]. Hence, volume reabsorption, J_{v}, is defined by the piecewise function

$$J'_{\mathrm{v}} = \begin{cases} \kappa' \exp(-\theta' z') & 0 \le z' < z'_{\mathrm{p}} \text{ (proximal tubule)}, \\ -L'_{\mathrm{v}}(C' - C'_{\mathrm{I}}(z)) & z'_{\mathrm{p}} \le z' < z'_{\mathrm{d}} \text{ (descending limb)}, \\ 0 & z'_{\mathrm{d}} \le z' < 1 \text{ (ascending limb)}, \end{cases} \tag{3.29}$$

where z'_{p} and z'_{d} are the nondimensionalised tubular positions of the end of the proximal tubule and descending limb, respectively. The constants κ' and θ' determine the volume reabsorption in the proximal tubule and L'_{v} was the water permeability of the descending limb. The interstitial NaCl concentration, $C_{\mathrm{I}}(z)$, is assumed to be a piecewise linear function of z, representing the gradient from high NaCl concentration (300 $\mathrm{mmol} \cdot \mathrm{L}^{-1}$), at the ascending/descending limb boundary, to low NaCl concentration (150 $\mathrm{mmol} \cdot \mathrm{L}^{-1}$) at the proximal tubule and top of the ascending limb [28]. The fixed interstitial NaCl concentration profile can be seen in Figure 3.2.

NaCl concentration Equation

For a solute, in a reabsorbing tubule with volume flow Q, mass balance requires that

$$\frac{\partial (AC)}{\partial t} = -\frac{\partial (QC)}{\partial z} - J_{\mathrm{s}} \tag{3.30}$$

[28], where C is the NaCl concentration, A is the cross-sectional area of the tubule, and J_{s} is the NaCl flux. As (3.30) is another conservation equation, the form matches well with the solvent conservation equation, (3.26). The NaCl concentration is important in this model for two reasons: most importantly, it was the signal to the TGF mechanism, and secondly, it was the primary osmotically active component governing volume reabsorption, J_{v}, in the descending limb. Equation (3.30) was nondimensionalised using expressions in (3.8) and Table 3.2, giving

$$\frac{\partial \left(R'^2 C'\right)}{\partial t'} = -\frac{1}{2}\frac{\partial (Q'C')}{\partial z'} - J'_{\mathrm{s}}. \tag{3.31}$$

Solute flux (J'_{s})

In the proximal tubule, NaCl reabsorption was assumed to be proportional to volume reabsorption from (3.29). This ensures that the NaCl concentration remains constant over the length of the proximal tubule as observed experimentally. A more realistic model, which was not implemented here, would be to use active transport term for transport of NaCl across the tubule wall. In the descending limb, NaCl reabsorption is passive and is modelled by Fick's Law, expressly reabsorption is proportional to the NaCl concentration difference across the wall, $C(z) - C_{\mathrm{I}}(z)$ [28]. In the ascending limb, NaCl transport is a combination of passive transport as in the descending limb, and an active Na^+-K^+/$2Cl^-$ cotransporter, which pumps NaCl out of the tubule and is modelled as a Michaelis-Menten term [28]. The NaCl flux, J'_{s}, is defined piecewise, to account for the different transport properties, as

$$J'_{\mathrm{s}} = \begin{cases} C'_{\mathrm{in}}\kappa' \exp(-\theta' z') & 0 \le z' < z'_{\mathrm{p}} \text{ (proximal tubule)}, \\ L'_{\mathrm{s}}(C' - C'_{\mathrm{I}}(z)) & z'_{\mathrm{p}} \le z' < z'_{\mathrm{d}} \text{ (descending limb)}, \\ L'_{\mathrm{s}}(C' - C'_{\mathrm{I}}(z)) + \frac{V'_{\max} C'}{K'_{\mathrm{m}} + C'} & z'_{\mathrm{d}} \le z' \le 1 \text{ (ascending limb)}, \end{cases} \tag{3.32}$$

where C'_{in} was the inlet NaCl concentration, L'_{s} was the solute permeability of the loop of Henle, and $V'_{\max}$ and K'_{m} were the Michaelis-Menten constants describing

the active reabsorption of NaCl in the ascending limb.

Tubule inlet boundary conditions

The inlet boundary conditions for flow and pressure were determined by the glomerular model as $P'(t',0) = P'_{\mathrm{b}}$ and $Q'(t',0) = Q'_{\mathrm{d}}$. The inlet NaCl concentration was the same as the NaCl concentration in blood, namely $C'(t,0) = C'_{\mathrm{in}}$.

3.1.3 Tubuloglomerular feedback (TGF) model

The TGF mechanism was modelled using the first-order differential equation

$$\frac{\mathrm{d}R'_{\mathrm{a}}}{\mathrm{d}t'} = t'_0 \left(R^{*\prime}{}_{\mathrm{a}} - R'_{\mathrm{a}}\right). \tag{3.33}$$

This first-order differential equation was used instead of the second-order differential equation, (2.33), used by [28]. This equation provides a first-order response with characteristic time t'_0. Physiologically this characteristic time represents the time scale over which the afferent arteriole resistance returns to its target level (steady state), R^*_{a}, after perturbation. Experimentally, Loutzenhiser et al. [52] found that constriction of the afferent arteriole (increasing R'_{a}) has a time constant of 4 s. Afferent arteriole dilation (decreasing R'_{a}) has more complex dynamics, such as a consistent activation time delay of 1 s. However, it was modelled using the same time constant as vasoconstriction for simplicity.

The target resistance, $R^{*\prime}{}_{\mathrm{a}}$, of the afferent arteriole is phenomenologically related to the NaCl concentration at the macula densa, $C'_{\mathrm{md}} \equiv C'(t',1)$, through

$$R^{*\prime}{}_{\mathrm{a}}\left(C'_{\mathrm{md}}\right) = \xi'_{\max} - \frac{\psi'}{1+\exp\left(k'\left(C'_{\mathrm{md}} - C'_{\frac{1}{2}}\right)\right)} \tag{3.34}$$

[28], where $\xi'_{\max}$ is the maximum obtainable afferent arteriole resistance, ψ' is the resistance range, k' is related to the slope of the logistic curve (k' is sometimes referred to as the gain of the feedback mechanism), and $C'_{\frac{1}{2}}$ is the inflection point of the curve.

3.1.4 Downstream pressure boundary condition

The pressure at the macula densa has been observed experimentally to oscillate in the range consistent with the TGF frequency at approximately 0.03 Hz [27]. This

downstream pressure oscillates at the same frequency as the proximal pressure, proximal tubular flow, and macula densa NaCl concentration [27]. Two different downstream pressure boundary conditions were used to investigate their effect on the system: a constant as used by Keener and Sneyd [34],

$$P'(t,1) = P'_{\mathrm{d}}, \tag{3.35}$$

and the implicit empirical relationship from Sakai et al. [64] used by [28],

$$P'\left(t',1\right) = \frac{Q'\left(t',1\right)}{\left(\alpha' P'\left(t,1\right) + \beta'\right)^4}. \tag{3.36}$$

This empirical equation has similarities to Pousielle flow, where $\Delta P \propto Q/r^4$. The constant pressure boundary condition, (3.35), cannot replicate the experimentally observed oscillations in pressure at the macula densa, although it simplifies the system. Using (3.35) as the downstream pressure boundary condition also removes the possibility of oscillations occurring from the coupling between flow and pressure provided by (3.36).

3.1.5 Haematocrit

The glomerular model of Keener and Sneyd [34] assumes that the blood is only comprised of blood plasma and large plasma proteins. In reality red blood cells are much too big to pass through an undamaged glomerular wall and should be discounted from the fluid. Holstein-Rathlou and Marsh [28] use a scaling of the flow to allow for the haematocrit in the glomerular model, namely

$$\begin{aligned}
\frac{Q'_{\mathrm{i}}}{1-\mathrm{Hct}_{\mathrm{a}}} R'_{\mathrm{a}} &= P'_{\mathrm{a}} - P'_{\mathrm{g}}, \\
\frac{Q'_{\mathrm{e}}}{1-\mathrm{Hct}_{\mathrm{e}}} R'_{\mathrm{e}} &= P'_{\mathrm{g}} - P'_{\mathrm{e}}, \text{ and} \\
\mathrm{Hct}_{\mathrm{e}} &= \frac{1}{1 + \frac{C'_{\mathrm{A}}}{C'_{\mathrm{E}}} \frac{1-\mathrm{Hct}_{\mathrm{A}}}{\mathrm{Hct}_{\mathrm{A}}}},
\end{aligned} \tag{3.37}$$

where the last equation of (3.37) is derived by considering conservation of solute mass. The afferent and efferent tubule models of [28], (3.37), differs from the model of [34], (3.3), used in this thesis. Removing the haematocrit scaling of the volume flows used by [28] was found to have little effect on the qualitative behaviour of the oscillations while simplifying the solution process. The system

without the hematocrit scaling will tend to overestimate the flows through the afferent and efferent arterioles.

3.1.6 Noncompliant tubule

This compliant tubule model can be converted into the noncompliant case by setting γ' to zero. γ' is important in this analysis as the noncompliant case is mathematically simpler and will be used to elucidate some of the results from the more physiologically realistic compliant case.

The compliant case, given by equations (3.18), (3.28), and (3.31) as

$$\begin{aligned} 2\gamma' R' \frac{\partial P'}{\partial t'} + \frac{\partial Q'}{\partial z'} &= -J'_{\mathrm{v}}, \\ \frac{\partial P'}{\partial z'} &= -\left(\frac{8\mu L Q_{\mathrm{ref}}}{\pi P_{\mathrm{ref}} r_0^4}\right) \frac{Q'}{R'^4}, \text{ and} \\ \frac{\partial \left(R'^2 C'\right)}{\partial t'} &= -\frac{1}{2}\frac{\partial \left(Q'C'\right)}{\partial z'} - J'_{\mathrm{s}}, \end{aligned} \tag{3.38}$$

can be converted into the noncompliant case by setting $\gamma' = 0$ in the wall model, (3.27). This gives

$$\begin{aligned} \frac{\partial Q'}{\partial z'} &= -J'_{\mathrm{v}}, \\ \frac{\partial P'}{\partial z'} &= -\left(\frac{8\mu L Q_{\mathrm{ref}}}{\pi P_{\mathrm{ref}} r_0^4}\right) Q', \text{ and} \\ \frac{\partial C'}{\partial t'} &= -\frac{1}{2}\frac{\partial \left(Q'C'\right)}{\partial z'} - J'_{\mathrm{s}}. \end{aligned} \tag{3.39}$$

3.1.7 Model summary

In summary of the model so far, the single nephron model is comprised of a glomerular model, a tubule model, and a TGF model. The glomerular model is comprised of four equations:

$$Q'_{\mathrm{e}} + \frac{\pi'_{\mathrm{a}} Q'_{\mathrm{a}}}{P'_{\mathrm{g}} - P'_{\mathrm{b}}} \ln\left(\frac{\left(P'_{\mathrm{g}} - P'_{\mathrm{b}}\right) Q'_{\mathrm{e}} - \pi'_{\mathrm{a}} Q'_{\mathrm{a}}}{\left(P'_{\mathrm{g}} - P'_{\mathrm{b}}\right) Q'_{\mathrm{a}} - \pi'_{\mathrm{a}} Q'_{\mathrm{a}}}\right) = Q'_{\mathrm{a}} - K'_{\mathrm{f}}\left(P'_{\mathrm{g}} - P'_{\mathrm{b}}\right), \tag{3.40}$$

$$Q'_{\mathrm{a}} R'_{\mathrm{a}} = P'_{\mathrm{a}} - P'_{\mathrm{g}}, \tag{3.41}$$

$$Q'_{\mathrm{e}} R'_{\mathrm{e}} = P'_{\mathrm{g}} - P'_{\mathrm{e}}, \text{ and} \tag{3.42}$$

$$Q'_{\mathrm{d}} = Q'_{\mathrm{a}} - Q'_{\mathrm{e}}, \tag{3.43}$$

which relate the flows through the afferent and efferent arterioles and into the proximal tubule, $Q'_{\rm a}$, $Q'_{\rm e}$, and $Q'_{\rm d}$, respectively and pressures in the glomerulus, Bowman's capsule, downstream of the efferent arteriole, and upstream of the afferent arteriole, $P'_{\rm g}$, $P'_{\rm b}$, $P'_{\rm e}$, and $P'_{\rm a}$, respectively. $P'_{\rm b}$ and $Q'_{\rm d}$ are the inlet boundary conditions to the tubule model,

$$2\gamma' R' \frac{\partial P'}{\partial t'} + \frac{\partial Q'}{\partial z'} = -J'_{\rm v}, \tag{3.44}$$

$$\frac{\partial P'}{\partial z'} = -\left(\frac{8\mu L Q_{\rm ref}}{\pi P_{\rm ref} r_0^4}\right) \frac{Q'}{R'^4}, \tag{3.45}$$

$$\frac{\partial \left(R'^2 C'\right)}{\partial t'} = -\frac{1}{2}\frac{\partial \left(Q'C'\right)}{\partial z'} - J'_{\rm s}, \tag{3.46}$$

where P is pressure, Q is volume flow, C is concentration of NaCl and the solute, $J_{\rm s}$, and volume fluxes, $J_{\rm v}$, are given by

$$J'_{\rm s} = \begin{cases} C'_{\rm in}\kappa' \exp(-\theta' z') & 0 \le z' < z'_{\rm p} \text{ (proximal tubule)}, \\ L'_{\rm s}(C' - C'_{\rm I}(z)) & z'_{\rm p} \le z' < z'_{\rm d} \text{ (descending limb)}, \\ L'_{\rm s}(C' - C'_{\rm I}(z)) + \frac{V'_{\rm max}C'}{K'_{\rm m}+C'} & z'_{\rm d} \le z' \le 1 \text{ (ascending limb)}, \end{cases} \tag{3.47}$$

and

$$J'_{\rm v} = \begin{cases} \kappa' \exp(-\theta' z') & 0 \le z' < z'_{\rm p} \text{ (proximal tubule)}, \\ -L'_{\rm v}(C' - C'_{\rm I}(z)) & z'_{\rm p} \le z' < z'_{\rm d} \text{ (descending limb)}, \\ 0 & z'_{\rm d} \le z' < 1 \text{ (ascending limb)}. \end{cases} \tag{3.48}$$

Two downstream pressure boundary conditions were used to examine their affect on the system:

$$P'(t,1) = P'_{\rm d}, \tag{3.49}$$

and

$$P'\left(t',1\right) = \frac{Q'\left(t',1\right)}{\left(\alpha' P'\left(t,1\right) + \beta'\right)^4}. \tag{3.50}$$

The concentration of NaCl at the macula densa, given by the tubule model, is used in the TGF model, which varies the resistance of the afferent arteriole. The time dynamics follow

$$\frac{{\rm d}R'_{\rm a}}{{\rm d}t'} = t'_0\left(R^{*\prime}{}_{\rm a} - R'_{\rm a}\right), \tag{3.51}$$

where

$$R^{*\prime}{}_{\mathrm{a}}\left(C'_{\mathrm{md}}\right) = \xi'_{\max} - \frac{\psi'}{1+\exp\left(k'\left(C'_{\mathrm{md}} - C'_{\frac{1}{2}}\right)\right)}. \tag{3.52}$$

The crucial change to the model of Holstein-Rathlou and Marsh [28] is the TGF model. The inherently oscillatory second order differential equation that they used for the TGF model is replaced by a nonoscillatory first order differential equation.

3.1.8 Numerical methods

The three PDEs comprising the tubular model, (3.18); (3.26); and (3.31), were discretised in both time and space. The spatial index is denoted with an i and the temporal index with a j. The time derivatives were discretised as the difference between the values at the current time step, $j+1$, and the previous, j, using single sided finite differences. The volume flow, pressure, and NaCl concentration spatial derivatives were written using single sided difference operators at the current time step. Using values at the current time step instead of the previous created an implicit system. This improves the numerical stability of the system and allows for larger temporal steps without affecting the solution. The discretised version of (3.38) is

$$\begin{aligned}
2\gamma' R'_{(\mathrm{i,j+1})}\frac{P'_{(\mathrm{i,j+1})} - P'_{(\mathrm{i,j})}}{h'_{\mathrm{t}}} &= -\frac{Q'_{(\mathrm{i+1,j+1})} - Q'_{(\mathrm{i,j+1})}}{h'_{\mathrm{z}}} - J'_{\mathrm{v(i,j+1)}},\\
\frac{P'_{(\mathrm{i+1,j+1})} - P'_{(\mathrm{i,j+1})}}{h'_{\mathrm{z}}} &= -\left(\frac{8\mu L Q_{\mathrm{ref}}}{\pi P_{\mathrm{ref}} r_0^4}\right)\frac{Q'_{(\mathrm{i,j+1})}}{R'^4_{(\mathrm{i,j+1})}},\ \text{and}\\
\frac{R'^2_{(\mathrm{i,j+1})}C'_{(\mathrm{i,j+1})} - R'^2_{(\mathrm{i,j})}C'_{(\mathrm{i,j})}}{h'_{\mathrm{t}}} &= -\frac{1}{2}\frac{Q'_{(\mathrm{i+1,j+1})}C'_{(\mathrm{i+1,j+1})} - Q'_{(\mathrm{i,j+1})}C'_{(\mathrm{i,j+1})}}{h'_{\mathrm{z}}} - J'_{\mathrm{s(i,j+1)}},
\end{aligned}$$

for $i = 0, \ldots, n_{\mathrm{z}} - 1$. Equation (3.27) is substituted directly into the discretised PDEs as $R'_{(\mathrm{i,j+1})} = \gamma'\left(P'_{(\mathrm{i,j+1})} - P'_{\mathrm{I}}\right) + 1$. The discretised version of the glomerular

model equations, (3.2), (3.3), and (3.4) are

$$Q'_{\mathrm{e(j+1)}} + \frac{\pi'_{\mathrm{a}} Q'_{\mathrm{a(j+1)}}}{P'_{\mathrm{g(j+1)}} - P'_{\mathrm{b(j+1)}}} \ln\left(\frac{\left(P'_{\mathrm{g(j+1)}} - P'_{\mathrm{b(j+1)}}\right) Q'_{\mathrm{e(j+1)}} - \pi'_{\mathrm{a}} Q'_{\mathrm{a(j+1)}}}{\left(P'_{\mathrm{g(j+1)}} - P'_{\mathrm{b(j+1)}}\right) Q'_{\mathrm{a(j+1)}} - \pi'_{\mathrm{a}} Q'_{\mathrm{a(j+1)}}}\right) =$$
$$Q'_{\mathrm{a(j+1)}} - K'_{\mathrm{f}}\left(P'_{\mathrm{g(j+1)}} - P'_{\mathrm{b(j+1)}}\right),$$
$$Q'_{\mathrm{a(j+1)}} R'_{\mathrm{a(j+1)}} = P'_{\mathrm{a}} - P'_{\mathrm{g(j+1)}},$$
$$Q'_{\mathrm{e(j+1)}} R'_{\mathrm{e}} = P'_{\mathrm{g(j+1)}} - P'_{\mathrm{e}}, \text{ and}$$
$$Q'_{\mathrm{d(j+1)}} = Q'_{\mathrm{a(j+1)}} - Q'_{\mathrm{e(j+1)}}.$$

These temporal variables were written at the current time step, $j+1$. The discretised version of the first-order, temporal TGF model, (3.33), and the target resistance of the afferent arteriole, (3.34), were written at the current time step as

$$\frac{R'_{\mathrm{a(j+1)}} - R'_{\mathrm{a(j)}}}{h'_{\mathrm{t}}} = t'_0\left(R^{*\prime}{}_{\mathrm{a(j+1)}} - R'_{\mathrm{a(j+1)}}\right),$$
$$R^{*\prime}{}_{\mathrm{a(j+1)}} = \xi'_{\max} - \frac{\psi'}{1 + \exp\left(k'\left(C'_{(\mathrm{n_z,j+1})} - C'_{\frac{1}{2}}\right)\right)}$$

This produced a system of $3n_{\mathrm{z}} + 5$ implicit, nonlinear equations, where n_{z} is the number of spatial steps. The $3n_{\mathrm{z}} + 5$ variables were $Q_{\mathrm{i}},\ i = 0, \ldots, n_{\mathrm{z}}$; $P_{\mathrm{i}},\ i = 0, \ldots, n_{\mathrm{z}} - 1$; $C_{\mathrm{i}},\ i = 1, \ldots, n_{\mathrm{z}}$; Q_{a}; Q_{e}; P_{g}; and R_{a}. This system was solved, at every time step, using a multidimensional Newton's method initialised from the solution at the previous time step. The steady state was solved the same manner after time derivatives had been set to zero.

An extensive parameter search was carried out to test if sustained oscillations exist in the single nephron TGF model with constant downstream pressure boundary condition and noncompliant tubule. The stability of the system was investigated in two ways. The Jacobian matrix was calculated numerically from the system of ODEs arising from the spatial discretisation of the PDE (3.30) for NaCl concentration, and the TGF feedback equation (3.33). The eigenvalues of the Jacobian matrix were evaluated at the steady state for a wide range of parameter sets to determine the stability of the system. In addition, the system was integrated forward in time at different sets of parameter values. An increase in the successive differences between peaks and troughs of the time series was used to determine if the oscillations were sustained. Peaks and troughs were identified

by fitting a polynomial through the data points.

3.2 RESULTS

The primary goal of the work presented in this chapter was to determine if sustained oscillations exist in a physiologically realistic single nephron model and secondly to determine the important contributing factors. Tubular compliance was found to be an important contributing factor to sustained oscillations while the downstream pressure boundary condition, (3.35) or (3.36); the time dynamics of the flow, i.e., removing $\partial Q'/\partial t'$; and the haematocrit were unimportant. The parameters that were used in this chapter are shown in Table 3.6 unless otherwise stated in the caption.

3.2.1 Noncompliant tubule

The mathematically simpler noncompliant model, given by model (3.39), permits a simpler solution process and a greater degree of analysis, while losing a degree of physiological realism.

Steady state

Figure 3.2 shows the interstitial and steady state luminal NaCl concentration profiles in a noncompliant tubule. The interstitial NaCl concentration profile is assumed to be constant and is defined piecewise [28]. The NaCl concentration increases in the descending limb as water is reabsorbed by osmosis and NaCl is secreted in accordance with Fick's law. The NaCl concentration in the ascending limb decreases as NaCl is actively reabsorbed by the rate limited Na-K-2Cl (NKCC2) cotransporter. A balance is achieved between the active reabsorption of the NKCC2 cotransporter and the passive secretion modelled by Fick's law, as NaCl moves from the relatively higher NaCl concentration of the interstitial fluid into the tubular lumen. The profile appears as a piecewise function due to the piecewise nature of the transport terms. The NaCl concentration at the macula densa, $C(t, 1)$, was an important variable in the single nephron model as this is the signal to the TGF mechanism [39].

Figure 3.3 shows the noncompliant steady state profiles for pressure, NaCl concentration, flow, and radius. The flow decreases exponentially in the proximal tubule as water reabsorption was assumed to be proportional to an exponential

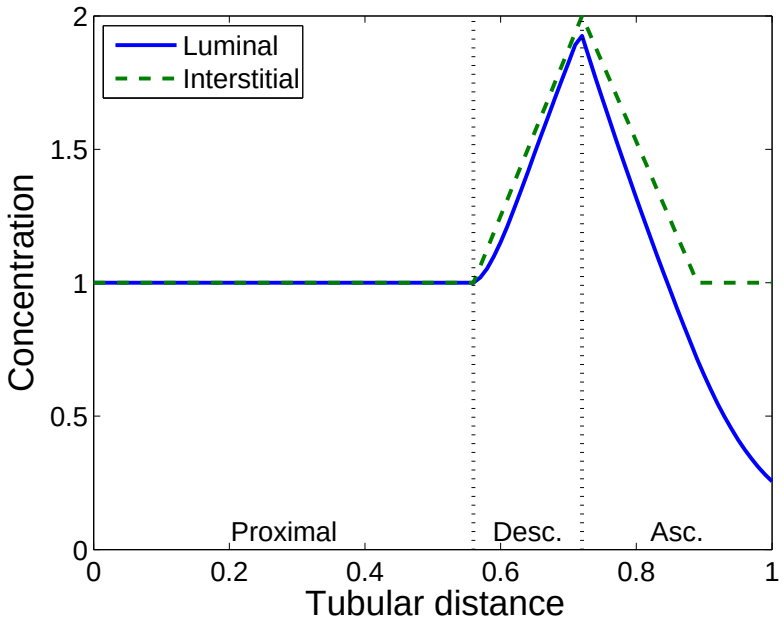

Figure 3.2 Steady state **noncompliant** interstitial (dotted) and luminal (solid) NaCl concentration profiles. The NaCl concentration at the macula densa, $z = 1$, is important in this model as it is the signal to the TGF mechanism [59].

decay function. The flow decreases in the descending limb as water was reabsorbed osmotically. The volume flow remains constant in the ascending limb because of the water impermeable wall. Volume flow is driven by the pressure drop throughout the length of the tubule. As the tubule is noncompliant, $\gamma' = 0$, the radius of the tubule is spatially and temporally constant, i.e., R=1.

Transient behaviour

Figure 3.4 shows the response of several model variables to a 5 mmHg pressure step in mean arterial pressure, P_a, at t=5 s. These variables were chosen as they are the most commonly reported experimental values. The pressure and flow at the end of the proximal tubule exhibit a sudden increase at t=5 s in response to the afferent arteriole pressure step. This sudden increase is due to the infinite wave speed in a noncompliant tubule. After the initial perturbation the system exhibits damped oscillations to its new steady state. Damped oscillations were exhibited for every parameter set investigated.

The damped oscillations can be extended in time by varying several model parameters both independently and in conjunction. However, an extensive parameter search of the noncompliant, constant pressure boundary condition system

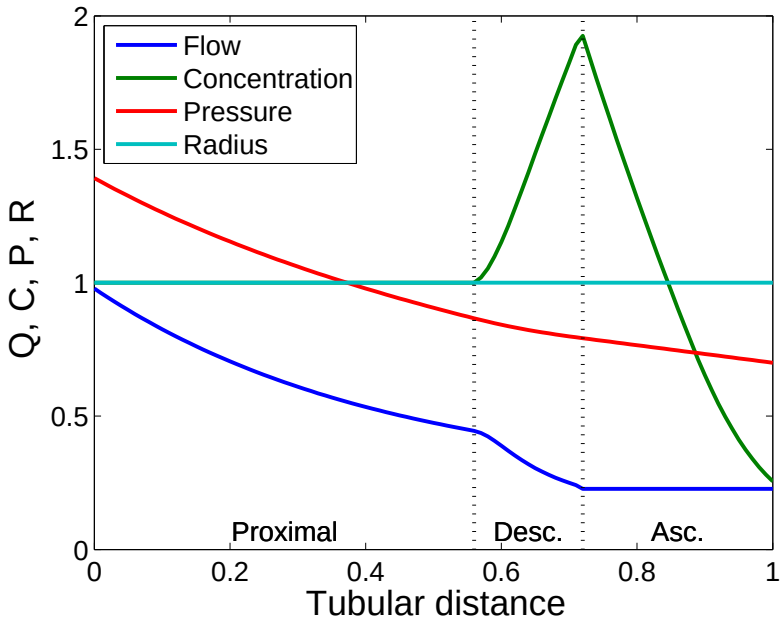

Figure 3.3 Steady state flow, NaCl concentration, pressure, and radius profiles for the **non-compliant** tubule.

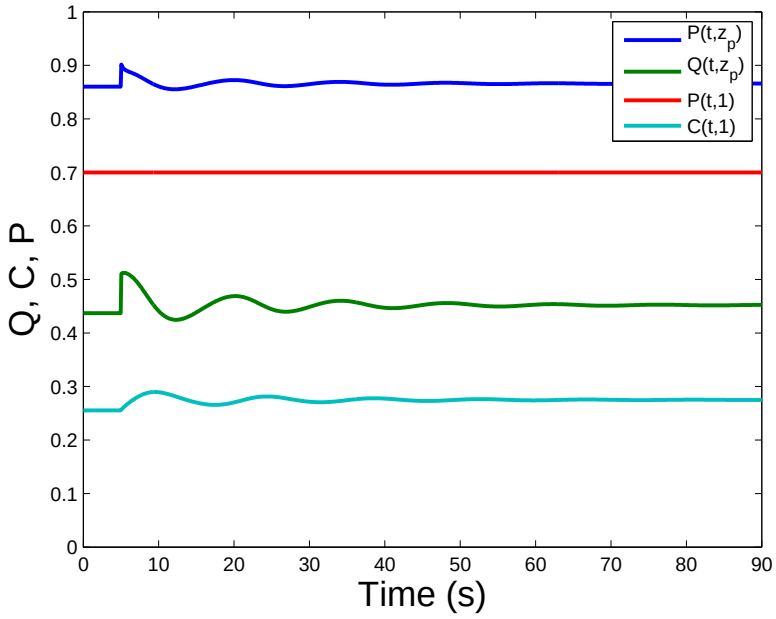

Figure 3.4 Transient behaviour of the pressures at the end of the proximal tubule, $z = z_{\mathrm{p}}$, and macula densa, z=1; flow at the end of the proximal tubule, $z = z_{\mathrm{p}}$; and NaCl concentration at the macula densa in the **noncompliant** tubular model. These variables are shown because they are the variables most commonly shown in the experimental literature, as they are readily available for measurement.

indicates that sustained oscillations are unlikely to exist in this system (or that the region of parameter space in which they exist is so small that it is unlikely to be encountered *in vivo*). For all parameter sets tested, the NaCl concentration always tended towards a stable equilibrium.

The numerical stability was investigated using the eigenvalues of the Jacobian matrix and by integrating forward in time as discussed in more detail in numerical methods, see Section 3.1.8. Eigenvalues with a positive real part were not encountered, indicating that the steady state is always stable. Hence, although oscillations decaying to the steady state often occurs, sustained oscillations are not expected. Forward integration in time did not identify any areas of parameter space that resulted in sustained oscillations, in agreement with the results of the stability analysis using the Jacobian matrix. This extensive parameter search using two different methods, implies that it is unlikely that sustained oscillations exist (or that they exist in an unrealistically small region of parameter space) in the noncompliant model. These parameter searches are simplistic and only vary one parameter at a time. A more sophisticated parameter search would be able to vary more than one parameter and would move in the direction of greatest descent of the largest real part of the eigenvalues of the system.

Sustained oscillations are exhibited if a second-order differential equation is used in place of (3.33), in agreement with the results of Holstein-Rathlou and Marsh [28].

Effect of TGF

The response of the noncompliant model, with and without TGF, to a pressure perturbation is shown in Figure 3.5. Both systems start in the steady state and are subject to a 10% step increase in inlet pressure, P_{a}, to P'_{MAP} at $t = 5$ s. The solid line shows the NaCl concentration at the macula densa without the TGF response, namely R_{a}=constant instead of (3.33). The step increase in inlet pressure causes an immediate increase in flow. This allows less time for osmosis and the cotransporter to act on the fluid as it flows more rapidly through the loop of Henle; hence the NaCl concentration at the macula densa ($z = 1$) is more similar to that of the inlet fluid. This can be seen in Figure 3.5. Following the pressure step, the NaCl concentration achieves a new equilibrium that is closer to the inlet NaCl concentration, $C'_{\mathrm{in}} = 1$. The dashed line shows the response with a fully functional TGF mechanism, represented by (3.33). After the pressure step increase, the NaCl concentration begins to increase as in the TGF disabled case.

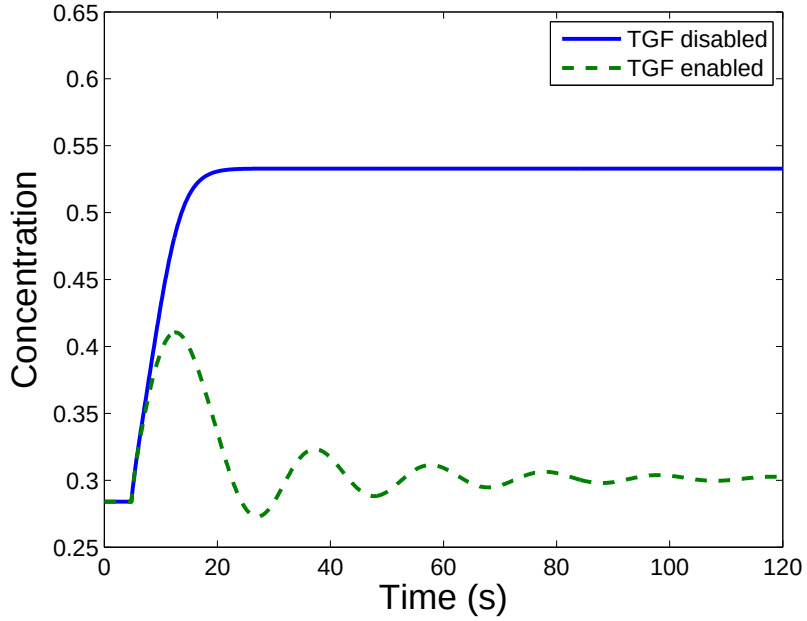

Figure 3.5 NaCl concentration at the macula densa, $C(t, 1)$, in response to a step increase in pressure at $t = 5$ s ($k' = 30$, $\gamma' = 0$): with TGF (dashed) and without TGF (solid) in the **noncompliant** tubular model. Without an intact TGF mechanism, the system quickly reaches a new equilibrium at a significantly higher NaCl concentration. With TGF intact, the system exhibits damped oscillations about a new, slightly higher equilibrium.

However, at approximately $t = 10$ s, the effect of the TGF becomes noticeable as the NaCl concentration levels off and then starts to decrease. This is caused by the increased resistance of the afferent arteriole that leads to a decrease in flow. Subsequently, the NaCl concentration exhibits damped oscillations, eventually reaching a new equilibrium value, which is only slightly higher than the equilibrium value prior to the pressure step. This demonstrates the role of the TGF mechanism in maintaining homeostasis of NaCl concentration at the macula densa.

3.2.2 Compliant tubule

The proximal tubule and the loop of Henle have been shown to have significant compliance [64]. Sakai et al. [64] experimentally measured the compliance of the proximal tubule to be 1.33×10^{-5} cm $\cdot$ mmHg^{-1} and the compliance of the loop of Henle to be 2.85×10^{-4} cm $\cdot$ mmHg^{-1}. These dimensional compliance values correspond to nondimensional compliance values, γ', of 0.1330 and 2.850, respectively. Nephron compliance depends on the type of anaesthetic. Compliance

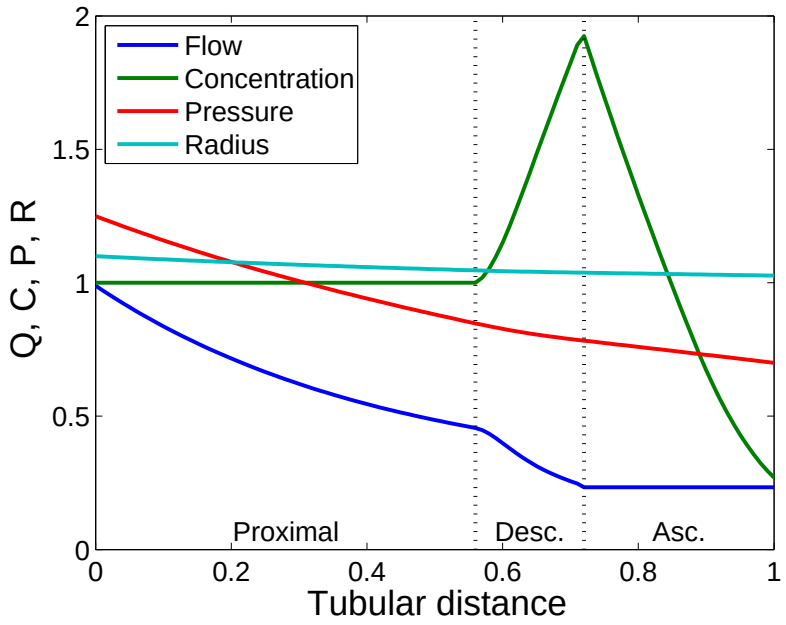

Figure 3.6 Steady state volume flow, pressure, NaCl concentration, and tubule radius profiles in the **compliant** tubule.

is significantly higher in rats that are anaesthetised with inactin compared to halothane [49].

Steady state

Figure 3.6 shows the steady state NaCl concentration, pressure, and volume flow profiles in the compliant tubule. The steady state of the compliant model is very similar to the steady state of the noncompliant model as shown in Figure 3.3. The notable difference is the spatial variance of the radius of the tubule. As the radius of the tubule is linearly related to the pressure through (3.27) it decreases with the decreasing pressure.

Transient behaviour

Time series of late proximal pressure and flow ($z = z_{\mathrm{p}} \approx 0.6$) and distal pressure and NaCl concentration ($z = 1$) are shown in Figure 3.7. Sustained oscillations are observed in all model variables. The oscillations occur at a frequency of approximately 0.06 Hz. These results were obtained by starting the model in the steady state and perturbing the inlet pressure, P_{a}, by 5 mmHg at $t = 5$. A much smaller inlet pressure perturbation of 10^{-4} mmHg was also enough to elicit

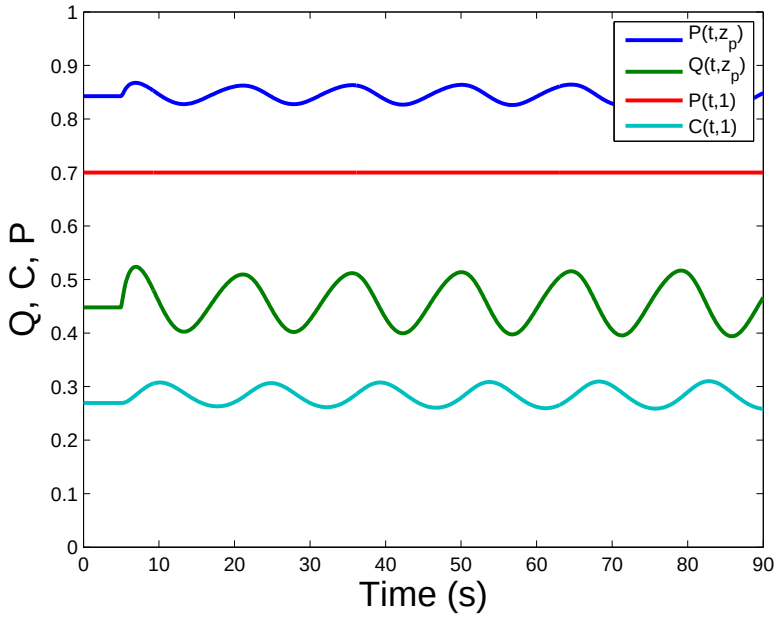

Figure 3.7 Sustained oscillations in late proximal pressure and flow ($z' = z'_{\mathrm{p}} \approx 0.6$) and distal pressure and NaCl concentration ($z' = 1$) in response to a relatively small, 5 mmHg, pressure step at t=5 s, with γ'=0.1330. The **compliant** tubule system is started in the steady state at t=0 s.

sustained oscillations, showing the instability of the system at the steady state. In the compliant model, the stability analysis techniques discussed previously in numerical methods were unnecessary as sustained oscillations were present for a large region of parameter space.

These oscillations compare well qualitatively with both experimental [48, 49, 27] and modelling [28, 42, 16] results. The oscillations are sustained and return to a stable limit cycle on perturbation. A mechanical perturbation and a chemical perturbation were simulated. A mechanical perturbation was simulated by varying the pressure at the afferent arteriole as a step function. This models a sudden change in pressure naturally occurring in vivo or a pressure change applied by an experimentalist. A chemical perturbation was applied by setting the TGF gain, k', to zero then back to its original nonzero value. This simulated the effect of blocking the TGF sensor mechanism as can be achieved experimentally by administration of furosemide. The order of the phase leads and lags in relation to late proximal pressure are also consistent with experimental and modelling results.

Quantitative comparison between the frequencies and amplitudes exhibited by the model presented in this chapter and observed in experimental results

is shown in Table 3.3. The frequency of the oscillations with either downstream pressure boundary condition were marginally higher than the frequencies reported in the experimental literature. This highlights the effect of the second-order ODE used by [28]. The second-order ODE has a slow natural frequency. Using a second-order ODE rather that the first-order ODE as used in this thesis reduces the frequency of the oscillations.

The experimentally observed amplitudes of the proximal pressure oscillations varies substantially. This could result from where the pressure is measured as the measurement site is likely to differ between experimental preparations. The amplitude of the proximal pressure oscillations exhibited by the current model is within the range of these experimental results. The amplitude of the distal pressure oscillations with the constant downstream pressure boundary condition does not compare well with the one piece of experimental data. Experimental results show that there are pressure oscillations at the macula densa. This is not captured in this model as the pressure at the macula densa is held constant by the boundary condition. There is an oscillation in this model with the empirical [28] boundary condition and the amplitude is higher than the experimental results. The amplitude of the oscillations in the NaCl concentration at the macula densa from the model with the constant downstream pressure boundary condition falls within the one range reported experimentally. The amplitude of the NaCl oscillation using the empirical [28] boundary condition is approximately four times higher than the experimental results. This is also the case in the modelling results presented in Holstein-Rathlou and Marsh [28].

Table 3.4 shows a quantitative comparison between the phase differences exhibited by the model presented in this chapter and one set of experimental measurements. The experimentally measured phases of the distal pressure, proximal flow, and distal NaCl oscillations are reported relative to the proximal pressure oscillation and hence so are the modelling results of this chapter. The phase lag of the distal pressure and the phase lead of the proximal flow oscillations exhibited by the current model are just below the range reported experimentally. The phase lag between the proximal pressure and the distal NaCl concentration oscillation is about half that reported experimentally. If the phase lags are reported relative to the period of the oscillation the experimental and model results show better agreement.

Figure 3.8 shows the effect of the empirical boundary condition given by (3.36). Using (3.36) instead of the constant pressure condition given by (3.35)

Table 3.3 Quantitative comparison of frequencies and amplitudes between the current model with a compliant tubule and experimental results. Columns represent frequency, early proximal tubular pressure amplitude, distal tubular pressure amplitude, and distal NaCl concentration amplitude, respectively. Rows represent the model with the constant boundary condition, (3.35); model with the empirical boundary condition, (3.36); and six experimental results, respectively. Numbers are given as a range, mean±standard deviation, or as a single number when only one value was given or when results were shown for a single animal.

	Frequency (Hz)	**Prox. pres. (mmHg)**	**Dist. pres. (mmHg)**	**Dist. conc. (mmol)**
Current (3.35)	0.06	1	0	5
Current (3.36)	0.05	2	1.5	15
[**27**]	0.036±0.0045	1.23±0.44	0.48±0.15	3.8±1.7
[**23**]	0.02–0.0467	5		
[**47**]	0.03	3.41±1.29		
[**48**]	0.02–0.04	2–3		
[**24**]	0.0345±0.003			
[**74**]	0.02–0.05			

Table 3.4 Quantitative comparison of phase leads and lags between current model and the available experimental results. Columns represent the delay between the proximal pressure maximum and the maximum of the: distal tubular pressure, $P(t,1)$; late proximal flow, $Q(t,z_{\mathrm{p}})$; and distal NaCl concentration, $C(t,1)$, respectively. Rows represent model with constant boundary condition, (3.35); model with empirical boundary condition, (3.36); and one experimental result, respectively.

	Dist. pres. (s)	**Prox. flow (s)**	**Dist. conc. (s)**
Current (3.35)	-	0	3.78
Current (3.36)	0.36	-1.08	3.78
[**27**]	1.05±0.38	-1.5±0.4	8.9±0.8

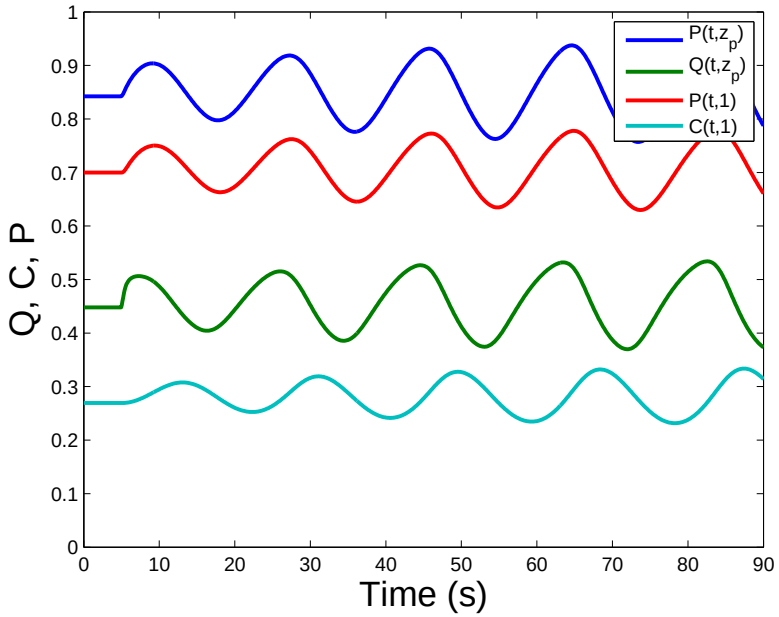

Figure 3.8 With the Holstein-Rathlou boundary condition, (3.36). Sustained oscillations in late proximal pressure and flow ($z' = z'_{\mathrm{p}} \approx 0.6$) and distal pressure and NaCl concentration ($z' = 1$) in response to a relatively small 5 mmHg pressure step at t=5, with γ'=0.1330. The system is started in the steady state at t=0.

changes the quantitative behaviour of the system and has no effect of the qualitative aspects of the system, for example the generation of the stable limit cycle and the order of the time lags. The quantitative differences are shown in Table 3.3. The notable differences are that: the frequency of the oscillations is slower and the pressure oscillates at the distal end of the tubule. The frequency of approximately 0.05 Hz is more consistent with the experimentally observed frequency of the TGF mechanism than the constant boundary condition, (3.35). Experimental evidence from Leyssac and Baumbach [47] shows that the distal pressure oscillates at the frequency of the TGF mechanism and hence the empirical boundary condition for pressure is more realistic than the constant boundary condition.

Figure 3.9 shows a time series of two model variables with the constant boundary condition and lower compliance than shown in Figure 3.7. The system exhibits damped oscillations, however they persist longer than the noncompliant case shown in Figure 3.4.

Figure 3.10 shows a time series of two model variables with a low value of TGF gain, k'. The compliant system exhibits damped oscillations. This agrees

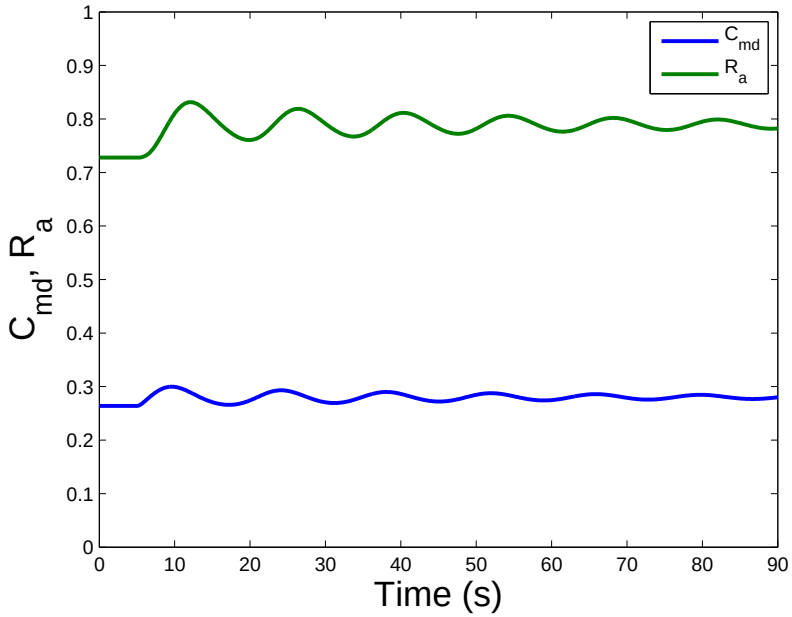

Figure 3.9 Halving the compliance of the tubule changed the behaviour of the system from sustained to damped oscillations in response to a 5 mmHg pressure step ($\gamma' = 0.0665$). The constant pressure downstream boundary condition was used, (3.35).

with the results of Holstein-Rathlou and Marsh [28] who found that k needed to be above approximately 0.1 to produce sustained oscillations.

Figure 3.11 shows the effect of varying the compliance, γ', on the amplitude and frequency of the macula densa NaCl concentration oscillations. Values of γ'=0.1330 and γ'=0.0665 were used to create Figures 3.7 and 3.9, respectively. The steady state becomes unstable at a compliance value of approximately 0.1. The steady state does not stay unstable and becomes stable again as compliance is increased. The steady state becomes stable again because of the position of the steady state on the TGF curve. High compliance lead to high flow as the tubule was distended that lead to high NaCl concentration at the macula densa. The steady state was no longer on a steep portion of the TGF curve, (3.34), and sustained oscillations were not exhibited.

Figure 3.12 shows the effect of varying the TGF gain, k', on the amplitude and frequency of the macula densa NaCl concentration oscillations. Values of k'=60 and k'=30 were used to create Figures 3.7 and 3.10, respectively. The steady state becomes unstable at a TGF gain value of approximately 50. The shape of the amplitude curve indicates a Hopf bifurcation. Holstein-Rathlou and Marsh [28] also found a bifurcation from stable to unstable behaviour at

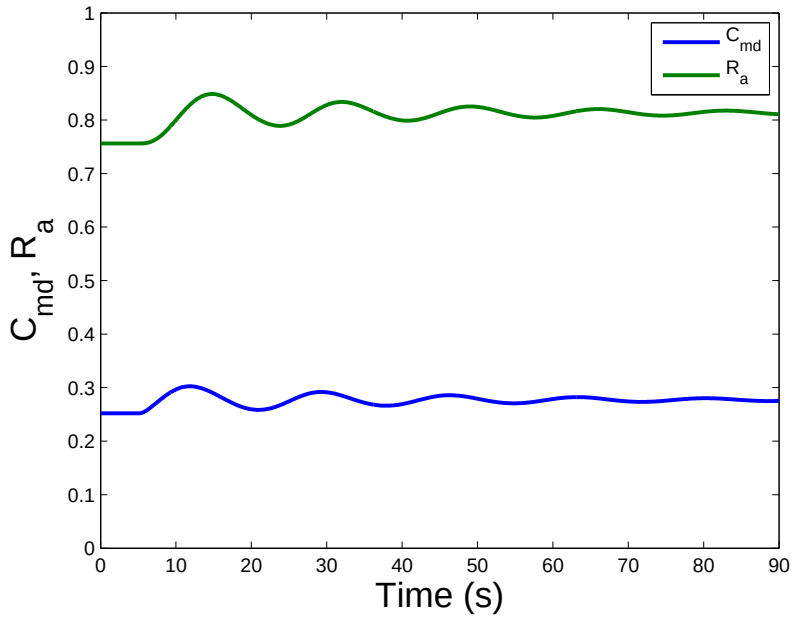

Figure 3.10 Halving the TGF gain of the system changed the behaviour of the system from sustained to damped oscillations in response to a 5 mmHg pressure step ($k' = 30$). The constant pressure downstream boundary condition was used, (3.35).

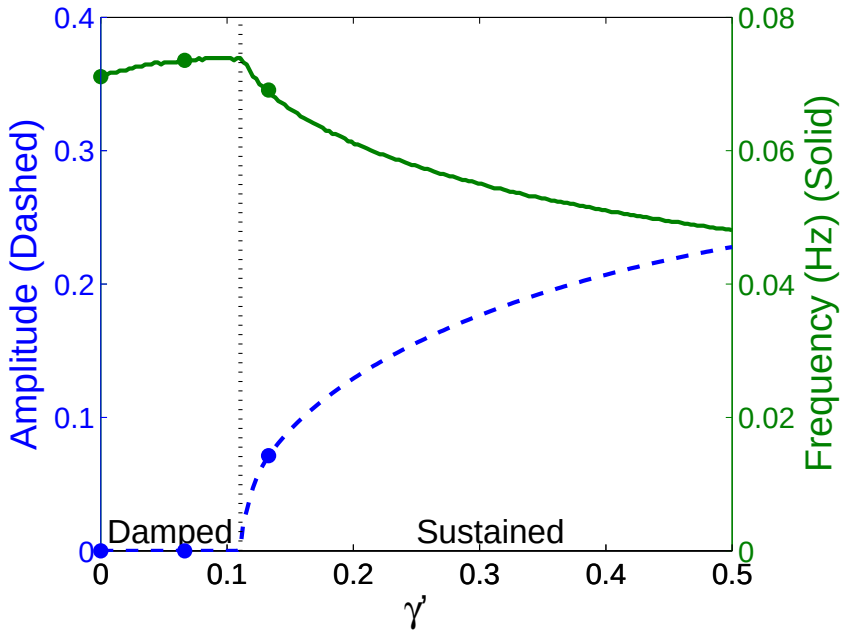

Figure 3.11 Effect of varying compliance, γ', on the amplitude and frequency of the macula densa NaCl concentration. A bifurcation occurs at a compliance value of approximately 0.1. For compliance values less than approximately 0.1 the steady state is stable. The steady state is unstable for compliance values greater than approximately 0.1. The points show the values of compliance used to create Figures 3.4, 3.7, and 3.9.

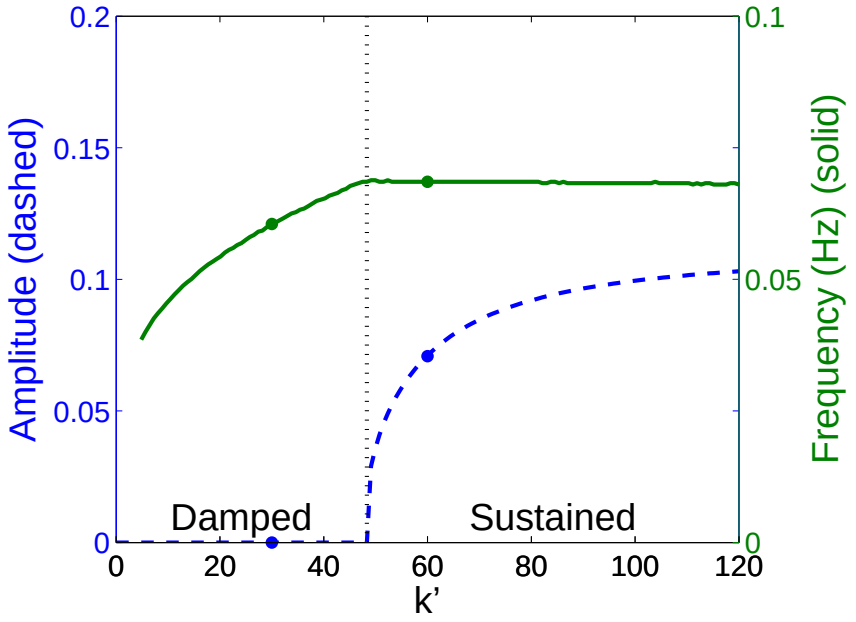

Figure 3.12 Effect of varying TGF gain, k', on the amplitude and frequency of the macula densa NaCl concentration. The points show the values of the TGF gain used to create Figures 3.7 and 3.10.

$k \approx 0.1$ corresponding to $k' \approx 15$. In relation to the bifurcation value of [28], the bifurcation in the current research occurs at a higher value of k', although the same qualitative behaviour is apparent. Another notable feature of the system is that if oscillatory behaviour is exhibited then it occurs at roughly the same frequency, independent of k'. For low values of k', the peaks in the time series could not be found; this resulted in an indeterminate frequency.

3.3 DISCUSSION

The results described in this chapter show that relatively low-frequency, sustained oscillations, at approximately 0.06 Hz, in flow, pressure, and NaCl concentration can be observed in a physiologically realistic system without using an inherently oscillatory model for afferent arteriole resistance. Both the compliance of the tubule and the TGF gain, k', have been shown to be key parameters in the development of sustained oscillations.

The frequency of 0.06 Hz is consistent with the time scale of the TGF mechanism. Fluid transit time from the site of TGF actuation (the glomerulus) to the site of TGF sensation (the macula densa) is approximately 30 s [1]. How-

ever, it does not take this long for a change in single nephron glomerular filtration rate, Q_{d}, to affect the NaCl concentration at the macula densa as the flow quickly equilibrates and begins to affect NaCl concentration throughout the tubule. Therefore, one would expect TGF-induced oscillations to have a shorter period than 30 s, which agrees with the model predictions. Oscillations with a period of approximately 30 s have been observed experimentally that disappear with intratubular microperfusion of furosemide, a TGF inhibitor [26].

While this model is based on the work of Holstein-Rathlou and Marsh [28], it contains an important difference. The model for TGF (i.e., the effect of NaCl concentration at the macula densa on the resistance of the afferent arteriole) is based on a first-order equation, rather than the second-order equation used by Holstein-Rathlou and Marsh [28]. The mechanism responsible for the low-frequency oscillations seen in this model is very different from that of Holstein-Rathlou and Marsh [28]. In using a second-order equation, Holstein-Rathlou and Marsh [28] effectively assumed that the TGF mechanism is inherently oscillatory, with a period of approximately 30 s. In the presented model, the sustained oscillations are a naturally arising property of the system.

Compliance is important in the generation of a stable limit cycle. The non-compliant model exhibits damped oscillations for every parameter set investigated. As compliance is increased there is a qualitative change in the behaviour of the system from damped to sustained oscillations. Sakai et al. [64] reported a value of tubular compliance corresponding to γ'=0.133 in the proximal tubule and 2.85 in the loop of Henle. Cortell et al. [13] found a proximal tubule compliance corresponding to values of γ'=0.45 and 1.0 for the proximal tubule and loop of Henle, respectively. Holstein-Rathlou and Marsh [28] used a single value for the proximal tubule compliance, γ'=0.133, and three compliance values for the loop of Henle, 0.133; 0.665; and 28.6, to investigate the effect on the delay and phase angle between flows, concentrations and pressures at various sites along the tubule. In the current research, one value of compliance was chosen for the entire renal tubule to simplify the analysis. However, significant simulation was undertaken with different compliance values for the proximal tubule and loop of Henle to ensure that sustained oscillations were still exhibited within the experimental ranges for compliance.

The model gives an insight as to why increasing compliance changes the behaviour of the system from damped to sustained oscillations. In the compliant system dilation of the afferent arteriole increases the volume flow throughout

the tubule more so than if the tubule was noncompliant. This can be explained by (3.18). In the compliant tubule the radius, r, is larger so to maintain the same pressure gradient, a higher flow is needed. This higher flow leads to a higher delivery and flux of NaCl at the macula densa than would have occurred if the tubule was noncompliant. Compliance has the opposite effect after the constriction of the afferent arteriole, with the NaCl delivery decreasing to a lower value than in the noncompliant case. It is hypothesised that sustained oscillations occur in the compliant case because of the larger change in NaCl concentration in response to a change in afferent arteriole resistance.

The hypothesis that compliance effects the generation of sustained oscillations would be hard to test experimentally. The small size of the tubules and inaccessibility means that changing the compliance mechanically would be difficult and would disrupt the normal function of the nephron. The compliance could be altered chemically. It is known that the type of anesthetic, barbiturate or halothane, effects the compliance [49]. Using these two commonly used anaesthetics with the experimental setup used in [27] would test the hypothesis that compliance is effecting the oscillations. However, this would only be valid over the range of compliances exhibited using each anaesthetic. In addition, anaesthetics are known to have a range of effects on renal function [25] and this experiment may be tainted by other effects of the anaesthetic.

The type of downstream pressure boundary condition, namely a constant downstream boundary pressure, (3.35), or an implicit relationship, (3.36), was found to be unimportant for the generation of sustained oscillations. The bifurcation point as compliance was varied was not affected significantly by the type of boundary condition. However, the oscillations exhibited by the implicit boundary condition showed better agreement with the experimentally observed, 0.5 mmHg distal pressure oscillation from Holstein-Rathlou and Marsh [27]. This model may produce more realistic results if the downstream pressure boundary condition was moved further downstream. This would allow the pressure to oscillate at the macula densa. The frequency of the oscillations was different with the implicit relationship case typically oscillating 0.005 Hz slower than the constant boundary condition case.

Holstein-Rathlou and Marsh [28] used afferent and efferent haematocrits in the relationships between afferent and efferent flow and arterial, glomerular, and efferent pressure, through (3.37). This was also determined to be unnecessary for the creation of sustained oscillations.

Holstein-Rathlou and Marsh [28] used a range of 0–0.4 $m^3 \cdot mol^{-1}$ for the slope of the TGF feedback curve, k, corresponding to a range of 0–60 for k'. A value of $k' = 30$ in the physiologically realistic compliant case produced close agreement. This value falls within the range reported by Holstein-Rathlou and Marsh [28] to be physiologically realistic.

An important feature of the *in vivo* system that is not currently modelled is the transmission of the TGF signal from the cells of the macula densa to the afferent arteriole smooth muscle cells. This transmission occurs via a number of intermediate mechanisms and does not take place instantaneously, but over a period of time [42]. This time delay will be in addition to the fluid transit time through the renal tubule, thus lengthening the overall time delay associated with the TGF loop. It is possible that this will increase the likelihood of sustained oscillations.

In summary, without a second-order differential equation to describe the TGF mechanism, sustained oscillations are unlikely in the noncompliant single nephron model. Sustained oscillations were observed in the model using a first-order differential equation for the TGF feedback and a compliant tubule model. These oscillations are shown to arise naturally without using an oscillatory second-order differential equation. The oscillations resulted from the interaction of the TGF mechanism with the compliant tubule. A summary of the differences between the model of Holstein-Rathlou and Marsh [28] and the current work is shown in Table 3.5.

Table 3.5 A summary of the differences between the model of Holstein-Rathlou and Marsh [28] and the current research.

[28]	Current	Comment
Second-order DE for TGF	First-order DE for TGF	Oscillatory behaviour is still observed in the model. The system oscillates within the observed frequency for the TGF mechanism albeit more quickly. This shows the effect of the fundamental frequency of the second-order differential equation used by [28].
Empirical boundary condition	Empirical and constant boundary condition	No effect on the qualitative oscillatory behaviour of the system. Empirical boundary condition shows better comparison to experimental results exhibiting oscillations of 2–3 mmHg in the distal pressure.
$\partial Q/\partial t$ retained	$\partial Q/\partial t$ neglected	Negligible effect on system. Significantly simplifies numerical solution procedure.
Haematocrit	Assume Hct=0	No effect on qualitative oscillatory behaviour.

Table 3.6 †, ‡ or ° parameters are taken from Keener and Sneyd [34], Young and Marsh [75] or Loutzenhiser et al. [52], respectively. All other model parameters are taken directly from Holstein-Rathlou and Marsh [28] unless stated otherwise. All parameters have been converted to SI units from the original papers and rounded to their original precision. All prime parameters have been created in the nondimensionalisation of the system during the current research.

Glomerular		
$P_{\text{MAP}} = P'_{\text{MAP}} P_{\text{ref}}$	1.447×10^{4} (Pa)	Mean arterial pressure
$P_{\text{e}} = P'_{\text{e}} P_{\text{ref}}$	2.4×10^{3} (Pa)†	Efferent arteriole pressure
$\pi_{\text{i}} = \pi'_{\text{i}} P_{\text{ref}}$	3.3×10^{3} (Pa)†	Input osmotic pressure
$R_{\text{e}} = R'_{\text{e}} R_{\text{ref}}$	1.4×10^{15} ($\text{Pa}\cdot\text{s}\cdot\text{m}^{-3}$)	Efferent arteriole resistance
$K_{\text{f}} = K'_{\text{f}} Q_{\text{ref}}/P_{\text{ref}}$	3.1×10^{-16} ($\text{m}^3\cdot\text{s}^{-1}\cdot\text{Pa}^{-1}$)	Glomerular wall filtration fraction
Λ	3.3	Effective blood viscosity constant
Hct_{a}	0.5	Haematocrit
Tubular		
$z_{\text{p}} = z'_{\text{p}} L$	1.0×10^{-2} (m)	Distance to end of proximal tubule
$z_{\text{d}} = z'_{\text{d}} L$	1.3×10^{-2} (m)	Distance bend of loop of Henle
L	1.8×10^{-2} (m)	Tubule length
r_0	1×10^{-5} (m)	Tubule radius
n_{s}	2	Number of osmoles per mole of NaCl
$C_{\text{in}} = C'_{\text{in}} C_{\text{ref}}$	150 ($\text{mmol}\cdot\text{L}^{-1}$)	Inlet NaCl concentration
$P_{\text{d}} = P'_{\text{d}} P_{\text{ref}}$	9.3×10^{2} (Pa)	Macula densa pressure
$\kappa = \kappa' Q_{\text{ref}}/L$	5.60×10^{-11} ($\text{m}^2\cdot\text{s}^{-1}$)	Proximal volume reabsorption constant
$\theta = \theta'/L$	1.3×10^{2} (m^{-1})	Proximal volume reabsorption constant
$L_{\text{v}} = L'_{\text{v}} Q_{\text{ref}}/(L n_{\text{s}} C_{\text{ref}})$	2×10^{-12} ($\text{m}^5\cdot\text{mol}^{-1}\cdot\text{s}^{-1}$)	Desc. limb water permeability
$L_{\text{s}} = L'_{\text{s}} Q_{\text{ref}}/L$	3.4×10^{-11} ($\text{m}^2\cdot\text{s}^{-1}$)	Asc. limb NaCl permeability
$V_{\max} = V'_{\max} Q_{\text{ref}} C_{\text{ref}}/L$	1×10^{-8} ($\text{mol}\cdot\text{m}^{-1}\cdot\text{s}^{-1}$)	Asc. limb Michaelis-Menten constant
$K_m = K'_{\text{m}} C_{\text{ref}}$	20 ($\text{mmol}\cdot\text{L}^{-1}$)	Asc. limb Michaelis-Menten constant
$\eta = \eta' \pi r_0^4 P_{\text{ref}}/(8 L Q_{\text{ref}})$	7.2×10^{-4} ($\text{Pa}\cdot\text{s}$)‡	Dynamic viscosity of tubular fluid
$\gamma_1 = \gamma' r_0/P_{\text{ref}}$	9.98×10^{-10} ($\text{m}\cdot\text{Pa}^{-1}$)	Tubular compliance
$\alpha = \sqrt[4]{Q_{\text{ref}}/P_{\text{ref}}^5}\,\alpha'$	1.31×10^{-8} ($\text{m}^3\cdot\text{s}^{-1}\cdot\text{Pa}^{-5})^{\frac{1}{4}}$	Boundary condition constant
$\beta = \sqrt[4]{Q_{\text{ref}}/P_{\text{ref}}}\,\beta'$	9.77×10^{-5} ($\text{m}^3\cdot\text{s}^{-1}\cdot\text{Pa}^{-1})^{\frac{1}{4}}$	Boundary condition constant
Tubuloglomerular feedback (TGF)		
$\xi_{\max} = \xi'_{\max} R_{\text{ref}}$	4.6×10^{14} ($\text{Pa}\cdot\text{s}\cdot\text{m}^{-3}$)	Afferent arteriole resistance range
$\psi = \psi' R_{\text{ref}}$	1.6×10^{14} ($\text{Pa}\cdot\text{s}\cdot\text{m}^{-3}$)	Max. value of afferent arteriole resistance
$k = k'/C_{\text{ref}}$	0.4–2.0 ($\text{m}^3\cdot\text{mol}^{-1}$)	Sensitivity of the TGF response
$C_{\frac{1}{2}} = C'_{\frac{1}{2}} C_{\text{ref}}$	44 ($\text{mmol}\cdot\text{L}^{-1}$)	Inflection point of the TGF curve
$t'_0 = t_{\text{ref}}/t_0$	2.4	Afferent arteriole time reference value
t_0	4 (s) °	Tubular time reference value
Ornstein-Uhlenbeck pressure forcing		
ω'	140	Rate of mean reversion
σ'	4.2	Average magnitude of fluctuations
$V_{\text{LT}} = V'_{\text{LT}} P_{\text{ref}}^2$	1.11×10^{5} (Pa^2)	Long term variance
Reference values		
Q_{ref}	5.8×10^{-13} ($\text{m}^3\cdot\text{s}^{-1}$) ‡	Tubular volume flow reference value
P_{ref}	1.3×10^{3} (Pa) ‡	Tubular pressure reference value
C_{ref}	150 ($\text{mmol}\cdot\text{L}^{-1}$)	NaCl concentration reference value
$t_{\text{ref}} = \pi r_0^2 L/Q_{\text{ref}}$	9.7 (s)	Tubular time reference value
$R_{\text{ref}} = P_{\text{ref}}/Q_{\text{ref}}$	2.3×10^{15} ($\text{Pa}\cdot\text{s}\cdot\text{m}^{-3}$)	Tubular resistance reference value

Chapter 4

MODEL SIMPLIFICATION

The single nephron tubuloglomerular feedback (TGF) model presented in Chapter 3 requires significant computation time due to the system of partial differential equations (PDEs) used to model the tubule. If a simpler system was found this would result in significant savings in computational time and potentially allow a higher level of analytical analysis. Several ordinary differential equation (ODE) tubular models are available in the literature [26, 66]. These models treat the entire tubule as a lumped compartment by assuming a spatially constant pressure and constant volume fluxes. These models are appropriate in these contexts as the authors assume that flow is the signal to the TGF mechanism. Experimental studies have shown that the sodium chloride (NaCl) concentration is the signal to the TGF mechanism [59]. Lumped parameter models are inappropriate to use if the NaCl concentration is used as the signal to the TGF mechanism as spatial variability is lost in lumped parameter models. These models are also unable to capture significant physiological features such as the different transport properties of each tubular section; the spatial profiles for pressure, volume flow, and NaCl concentration; and variable volume and solute fluxes.

This chapter develops an ODE model to replace the computationally expensive, complex PDE tubular model presented in Chapter 3, (3.38). The system of PDEs was reduced to a system of ODEs by assuming spatial profiles for the pressure and the NaCl concentration. The noncompliant tubule model was reduced to a system of three ODEs in terms of the concentrations at the end of the proximal tubule, $C_1'(t)$; descending limb, $C_2'(t)$; and the ascending limb, $C_3'(t)$. In the compliant case another ODE is required to describe the time dynamics of the inlet pressure, $P_{\mathrm{b}}'(t)$. The simplicity of these ODE tubular models allows for a higher level of analysis. For example, the stability of the single nephron system can be determined by interrogating the system Jacobian matrix.

The NaCl concentration at the macula densa is an important variable in the PDE tubular model as it is the signal to the TGF mechanism. It is vital that any simplification of the PDE tubular model maintains the steady state and transient behaviour of the macula densa NaCl concentration. If this behaviour is lost then any insight gained through the analysis of the simpler model is irrelevant. The simplest function that could be used is a spatially constant profile, $C'(t', z') = C'_0(t'),\ z' \in [0,\ 1]$, as if the fluid in the tubule is well mixed. This is clearly inappropriate due to the piecewise nature of the steady state NaCl concentration profile of the PDE model shown in Figure 3.6. The NaCl concentration is constant in the proximal tubule, approximately linear and increasing in the descending limb, and approximately linear and decreasing in the ascending limb. The assumed profile must be piecewise to deal with the piecewise nature of the fluxes. It must also be continuous to ensure continuity of solute mass.

As shown in Chapter 3, examination of the noncompliant model, (3.39), gives insight into the more complex compliant model, (3.38), through its simpler solution procedure and higher level of analytical analysis. The ODE model will be constructed by assuming a linear or exponential spatial profile for each section of the tubule. This will be done for the noncompliant PDE model, (3.39), first, then generalised to model the compliant PDE model, (3.38).

4.1 SIMPLIFIED NONCOMPLIANT MODEL

This section constructs an ODE noncompliant tubular model that approximates the PDE noncompliant tubule model presented in Chapter 3 and compares the two models. The ODE model was constructed by assuming a spatial profile and integrating along the length of the tubule. This removed the dependency on the spatial coordinate leaving only the time coordinate. Two piecewise functions were investigated: a first-order polynomial and an exponential function. The exponential function was used only for the ascending limb. The exponential profile was investigated to address physiologically unrealistic results from the linear approximation, such as negative NaCl concentrations, at low arterial pressures.

4.1.1 PDE tubule model

As presented in Section 3.1.6, the equations of motion for a noncompliant tubule are

$$\frac{\partial Q'}{\partial z'} = -J'_{\mathrm{v}}, \tag{4.1}$$

$$\frac{\partial P'}{\partial z'} = -\left(\frac{8\mu L Q_{\mathrm{ref}}}{\pi P_{\mathrm{ref}} r_0^4}\right) Q', \text{ and} \tag{4.2}$$

$$\frac{\partial C'}{\partial t'} = -\frac{1}{2}\frac{\partial \left(Q'C'\right)}{\partial z'} - J'_{\mathrm{s}}, \tag{4.3}$$

where Q' is the volume flow, P' is pressure, C' is the NaCl concentration, J'_{v} and J'_{s} are the volume flux and NaCl flux through the tubule wall, μ is the dynamic viscosity, L is the length of the tubule, Q_{ref} and P_{ref} are typical volume flow and pressure values, and r_0 is the radius of the tubule at zero transmural pressure.

Each section of the renal tubule is anatomically and physiologically different and hence has different NaCl, J'_{s}, and volume fluxes, J'_{v}, as discussed in Section 3.1.2. The solute flux is modelled by an exponential function in the proximal tubule, osmosis in the descending limb, and the sum of a passive osmotic term and an active Michaelis-Menten term in the ascending limb. This gives

$$J'_{\mathrm{s}} = \begin{cases} C'_{\mathrm{in}}\kappa' e^{-\theta' z'} & 0 \le z' < z'_{\mathrm{p}} \text{ (proximal tubule)}, \\ L'_{\mathrm{s}}\left(C' - C'_{\mathrm{I}}(z)\right) & z'_{\mathrm{p}} \le z' < z'_{\mathrm{d}} \text{ (descending limb)}, \\ L'_{\mathrm{s}}\left(C' - C'_{\mathrm{I}}(z)\right) + \frac{V'_{\max} C'}{K'_{\mathrm{m}} + C'} & z'_{\mathrm{d}} \le z' < 1 \text{ (ascending limb)}. \end{cases} \tag{4.4}$$

The volume flux is modelled by an exponential function in the proximal tubule, osmosis in the descending limb, and the volume flux is zero in the ascending limb as the tubular wall is impermeable to water. This gives

$$J'_{\mathrm{v}} = \begin{cases} \kappa' e^{-\theta' z'} & 0 \le z' < z'_{\mathrm{p}} \text{ (proximal tubule)}, \\ L'_{\mathrm{v}}\left(C' - C'_{\mathrm{I}}(z)\right) & z'_{\mathrm{p}} \le z' < z'_{\mathrm{d}} \text{ (descending limb)}, \\ 0 & z'_{\mathrm{d}} \le z' < 1 \text{ (ascending limb)}. \end{cases} \tag{4.5}$$

A model for the motion of the tubule wall is unnecessary in a noncompliant setting as the nondimensional radius, R', is always one.

The geometry of the idealised nephron tubule is shown in Figure 4.1. This chapter presents a method for reducing the spatial and temporal system of PDEs to a system of temporal ODEs at four discrete points, $z = 0$, $z = z'_{\mathrm{p}}$, $z = z'_{\mathrm{d}}$, and

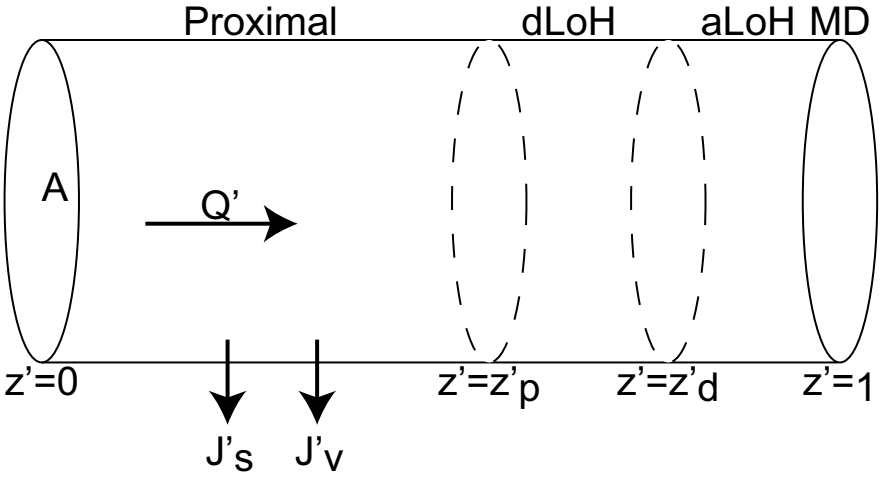

Figure 4.1 Tubular geometry. This is an idealised version on the more anatomically correct nephron shown in Figure 1.2. This diagram shows the proximal tubule; descending limb of the loop of Henle, dLoH; ascending limb of the loop of Henle, aLoH; and macula densa. The positions of the ends of each section are $z' = z'_{\mathrm{p}}$, $z' = z'_{\mathrm{d}}$, and $z' = 1$, respectively.

$z = 1$.

4.1.2 Piecewise linear tubule model

Nodal concentrations

To simplify (4.3) a spatially linear NaCl concentration profile was assumed in each section. This was done using a first-order Lagrange interpolating polynomial,

$$C'(t,z) = \frac{z'_{\mathrm{i+1}} - z'}{z'_{\mathrm{i+1}} - z'_{\mathrm{i}}} C'_{\mathrm{i}}(t') + \frac{z' - z'_{\mathrm{i}}}{z'_{\mathrm{i+1}} - z'_{\mathrm{i}}} C'_{\mathrm{i+1}}(t'), z'_{\mathrm{i}} \leq z' \leq z'_{\mathrm{i+1}}, \tag{4.6}$$

where $C'_{\mathrm{i}}(t')$ and $C'_{\mathrm{i+1}}(t')$ denote the time dependent NaCl concentrations at $z' = z'_{\mathrm{i}}$ and $z' = z'_{\mathrm{i+1}}$, respectively. Substitution of (4.6) into the left hand side of (4.3) gives

$$\frac{z'_{\mathrm{i+1}} - z'}{z'_{\mathrm{i+1}} - z'_{\mathrm{i}}} \frac{\mathrm{d}C'_{\mathrm{i}}}{\mathrm{d}t'} + \frac{z' - z'_{\mathrm{i}}}{z'_{\mathrm{i+1}} - z'_{\mathrm{i}}} \frac{\mathrm{d}C'_{\mathrm{i+1}}}{\mathrm{d}t'} = -\left(\frac{\partial (Q'C')}{\partial z'} + J'_{\mathrm{s}} \right). \tag{4.7}$$

Definite integration of (4.7) between z'_{i} and $z'_{\mathrm{i+1}}$ and the fundamental theorem of calculus gives

$$\frac{z'_{\mathrm{i+1}} - z'_{\mathrm{i}}}{2} \left(\frac{\mathrm{d}C'_{\mathrm{i}}}{\mathrm{d}t'} + \frac{\mathrm{d}C'_{\mathrm{i+1}}}{\mathrm{d}t'} \right) = -\left(\left(Q'_{\mathrm{i+1}} C'_{\mathrm{i+1}} - Q'_{\mathrm{i}} C'_{\mathrm{i}} \right) + \int_{z'_{\mathrm{i}}}^{z'_{\mathrm{i+1}}} J'_{\mathrm{s}} \mathrm{d}z' \right). \tag{4.8}$$

Rearranging for $\mathrm{d}C'_{\mathrm{i}+1}/\mathrm{d}t'$ gives

$$\frac{\mathrm{d}C'_{\mathrm{i}+1}}{\mathrm{d}t'} = -\frac{\mathrm{d}C'_{\mathrm{i}}}{\mathrm{d}t'} - \frac{2}{z'_{\mathrm{i}+1} - z'_{\mathrm{i}}} \left(Q'_{\mathrm{i}+1} C'_{\mathrm{i}+1} - Q'_{\mathrm{i}} C'_{\mathrm{i}} + \int_{z'_{\mathrm{i}}}^{z'_{\mathrm{i}+1}} J'_{\mathrm{s}} \mathrm{d}z \right). \tag{4.9}$$

Appropriately breaking the tubule into three sections gives the z'_{i} as: the tubule inlet ($z'_0 = 0$), the end of the proximal tubule ($z'_1 = z'_{\mathrm{p}}$), the end of the descending limb ($z'_2 = z'_{\mathrm{d}}$), and the macula densa ($z'_3 = 1$). Substituting the linear NaCl concentration profile, (4.6), into the NaCl flux, (4.4), and integrating over each section of the tubule gives

$$\int J'_{\mathrm{s}} \mathrm{d}z' = \begin{cases} C'_{\mathrm{in}} \frac{\kappa'}{\theta'} \left(e^{-\theta' z'_{\mathrm{p}}} - 1 \right), \\ \frac{L'_{\mathrm{s}}}{2} \left(C'_1 + C'_2 - C'_{\mathrm{c}} - C'_{\mathrm{m}} \right) \left(z'_{\mathrm{d}} - z'_{\mathrm{p}} \right), \\ (1 - z'_{\mathrm{d}}) \left(\frac{L'_{\mathrm{s}}}{2} \left(C'_2 + C'_3 - C'_{\mathrm{c}} - C'_{\mathrm{m}} \right) + V'_{\max} \left[1 + \frac{K'_{\mathrm{m}}}{C'_2 - C'_3} \ln \left(\frac{K'_{\mathrm{m}} + C'_3}{K'_{\mathrm{m}} + C'_2} \right) \right] \right), \end{cases} \tag{4.10}$$

where C'_{c} and C'_{m} are the interstitial concentrations in the cortex and medulla, respectively.

Nodal volume flows

Expressions for the nodal volume flows, Q_{i}, are needed for (4.8). These are found by definitely integrating (4.1) between z_{i} and $z_{\mathrm{i}+1}$ giving

$$Q'_{\mathrm{i}+1} - Q'_{\mathrm{i}} = -\int_{z'_{\mathrm{i}}}^{z'_{\mathrm{i}+1}} J'_{\mathrm{v}} \mathrm{d}z, \tag{4.11}$$

using the fundamental theorem of calculus. Definite integration of (4.5) across each section of the renal tubule gives

$$\int J'_{\mathrm{v}} dz = \begin{cases} \frac{\kappa'}{\theta'} \left(1 - e^{-\theta' z'_{\mathrm{p}}} \right) & \text{(proximal tubule)}, \\ \frac{1}{2} L'_{\mathrm{v}} \left(C'_1 + C'_2 - C'_{\mathrm{c}} - C'_{\mathrm{m}} \right) \left(z'_{\mathrm{d}} - z'_{\mathrm{p}} \right) & \text{(descending limb)}, \\ 0 & \text{(ascending limb)}, \end{cases} \tag{4.12}$$

implying the instantaneous nodal volume flow values are:

$$Q'_1 = Q'_0 - \frac{\kappa'}{\theta'}\left(1 - e^{-\theta' z'_\mathrm{p}}\right), \tag{4.13}$$

$$Q'_2 = Q'_1 - \frac{1}{2}L'_\mathrm{v}\left(C'_1 + C'_2 - C'_\mathrm{c} - C'_\mathrm{m}\right)\left(z'_\mathrm{d} - z'_\mathrm{p}\right), \text{ and} \tag{4.14}$$

$$Q'_3 = Q'_2. \tag{4.15}$$

Pressure

An expression for the pressure can be found by first differentiating (4.2) once with respect to z and substituting (4.1) to give

$$\frac{\partial^2 P'}{\partial z'^2} = \left(\frac{8\mu L Q_\mathrm{ref}}{\pi P_\mathrm{ref} r_0^4}\right) J'_\mathrm{v}. \tag{4.16}$$

Indefinite integration of (4.16) gives an expression that can then be integrated definitely between $z' = 0$ and $z' = 1$ to finally give an expression for the difference between inlet and outlet pressure,

$$P'_\mathrm{b} - P'_\mathrm{d} = f(C_0, C_1, C_2, C_3, Q_0). \tag{4.17}$$

While this process is relatively straightforward mathematically, the resulting expression for f is very long and hence is not shown here.

In summary of this noncompliant model, the system is comprised of four ODEs for C_1, C_2, C_3, and R_a, given by (4.9) with i=0, 1, and 2 and (3.33), respectively; three algebraic equations for Q, given by (4.13), (4.14), and (4.15), respectively; one algebraic equation for P, (4.17); and four algebraic equations representing the glomerulus, given by (3.2), (3.3), and (3.4) respectively. The time derivatives of C_1, C_2, C_3, and R_a can be written explicitly in terms of the other variables in this noncompliant model.

4.1.3 ODE-PDE comparison - steady state

Figure 4.2 shows the NaCl concentration profiles for the PDE model in blue and the assumed piecewise linear profile in green. The concentrations from the ODE tubular model, C'_1; C'_2; and C'_3, are shown as points and interpolated with a straight line. There is excellent agreement between the two models at the end of the proximal tubule, $z' = z'_\mathrm{p}$, the end of the descending limb, $z' = z'_\mathrm{d}$, and

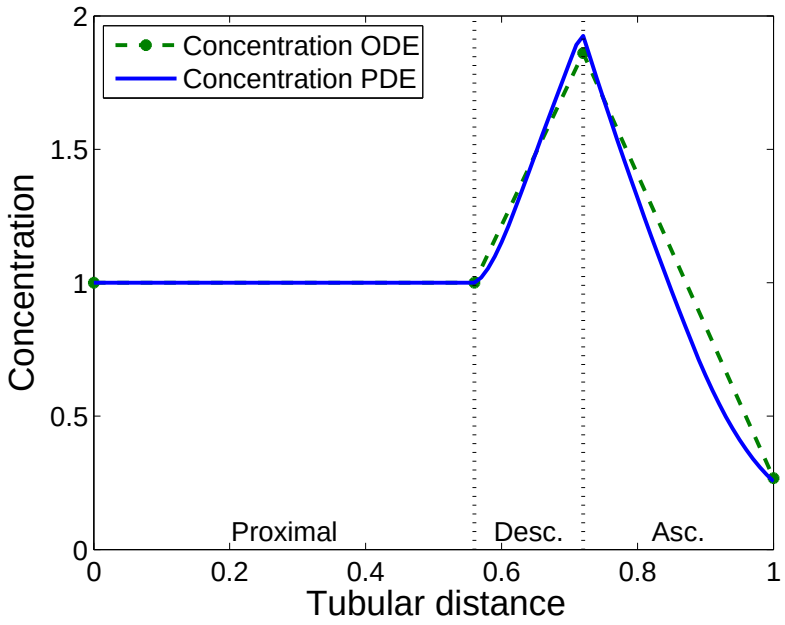

Figure 4.2 Steady state comparison of NaCl concentration profiles from **noncompliant** PDE and ODE tubular models.

most importantly at the macula densa. Agreement between the two models at the macula densa is important as the NaCl concentration at the macula densa is the signal to the TGF mechanism, determining the resistance of the afferent arteriole.

Figure 4.3 shows the nodal volume flow (blue) and pressure (green) profiles for the PDE (solid) and ODE (dashed) models. The linear assumption has only been applied to the concentration profile. The profiles for flow and pressure could be solved with no other assumptions imposed. It is expected that these profiles would give a much better fit to the profiles from the PDE model, but this was not done. As with the NaCl concentration profiles in Figure 4.2, the PDE and ODE model produce very similar volume flow and pressure profiles. The downstream pressures are the same due to the constant Dirichlet boundary condition, (3.35).

As would be expected, the ODE model approximates the PDE well when the profiles from the PDE model are reasonably linear. As the profiles from the PDE model become increasingly nonlinear the assumed linear ODE profiles become a poorer representation. Changing one of several model variables, $V'_{\max}$ or K_{m}, results in the ascending limb NaCl concentration profile of the PDE model becoming more nonlinear. The increased nonlinearity only occurs in the

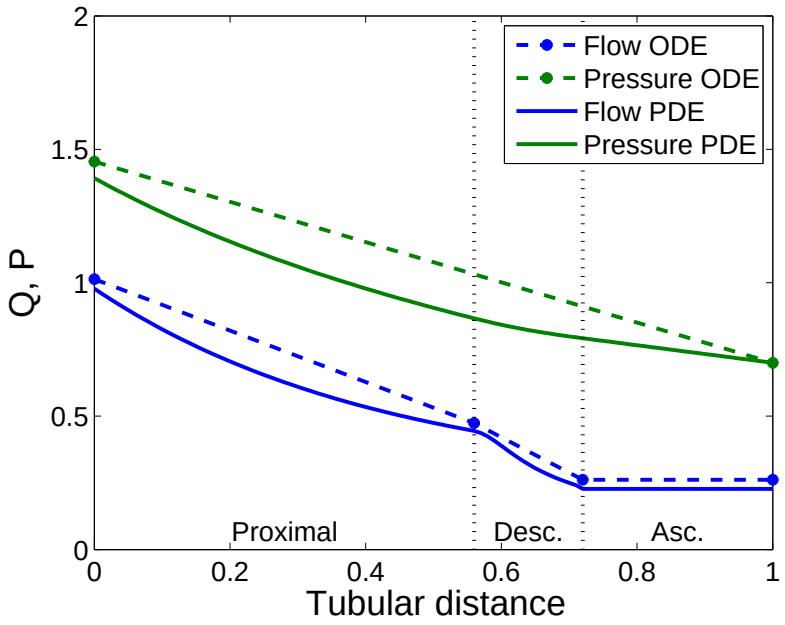

Figure 4.3 Steady state comparison of flow and pressure profiles from **noncompliant** PDE and ODE tubular models.

NaCl concentration profile of the ascending limb. The NaCl concentration profile in the proximal tubule stays linear because of the matched NaCl and volume fluxes. In the descending limb the NaCl concentration also stays roughly linear as osmosis quickly matches the luminal NaCl concentration with the assumed linear interstitial profile.

Low arterial pressure

The nonlinearity of the NaCl concentration profile in the ascending limb can be increased by changing the properties of the Na-K-2Cl (NKCC2) cotransporter or by varying arterial pressure. Figure 4.4 shows the effect of lowering the mean arterial pressure, P'_{MAP}, by 15%. The ascending limb NaCl concentration profile from the PDE model becomes nonlinear. Low pressure results in low volume flow that gives the ascending limb NKCC2 cotransporter more time to act on the fluid. Hence, the NaCl concentration initially drops more rapidly in the ascending limb. The NaCl concentration levels off as the NaCl transport out of the tubule via the NKCC2 transporter balances the influx of NaCl by passive diffusion. The NaCl concentration in the PDE cannot be negative. The steady

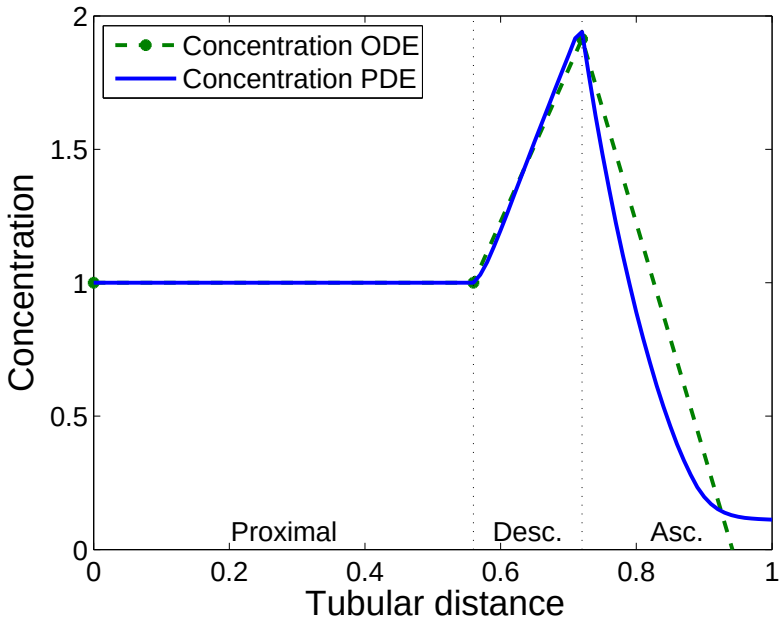

Figure 4.4 NaCl concentration profiles from the **noncompliant** ODE and PDE tubular models at low mean arterial pressure ($P'_{\mathrm{MAP}} = 0.85P'_{\mathrm{MAP}}$).

state NaCl concentration profile in the ascending limb is governed by

$$Q'\frac{\partial C'}{\partial z'} = -2L'_{\mathrm{s}}\left(C' - C'_{\mathrm{I}}(z)\right) - \frac{2V'_{\max}C'}{K'_{\mathrm{m}} + C'}, \tag{4.18}$$

from (4.3) and (4.4). Q' is positive and spatially constant as there is no volume flux in the ascending limb. The first term on the right hand side of (4.18) is positive when C' is small as $C' < 1 \leq C'_{\mathrm{I}}(z)\ \forall z$. The second term approaches zero as $C' \to 0$. This ensures that $\partial C'/\partial z > 0$ as $C' \to 0$ implying that the NaCl concentration cannot drop below zero. This is important because a negative NaCl concentration is physically unrealistic.

Unlike the PDE model, a positive NaCl concentration is not an inherent property of the ODE tubular model as shown in Figure 4.4. The NaCl concentration at the macula densa, C'_3, is clearly less than zero. In cases such as the low pressure case or high NKCC2 pump activity, high $V'_{\max}$, a linear approximation in the ascending limb is not a good representation of the PDE tubular model. The flow and pressure from the ODE and PDE tubular models still show good agreement even at low pressure, as shown in Figure 4.5.

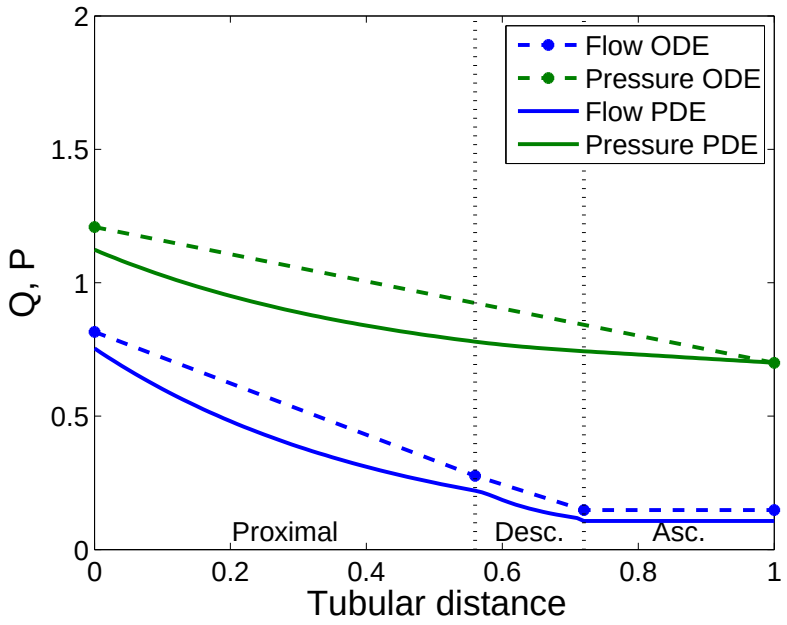

Figure 4.5 Flow and pressure profiles from the **noncompliant** ODE and PDE tubular models at low mean arterial pressure ($P'_{\mathrm{MAP}} = 0.85P'_{\mathrm{MAP}}$).

4.1.4 Exponential NaCl concentration profile

The linear profile introduced in this chapter is, as expected, a good representation of the PDE model only when the NaCl concentration profile in the ascending limb is linear. This good qualitative agreement can be extended to nonlinear profiles when an exponential decaying function,

$$C'(z',t') = C'_2(t')\exp(-\beta'(t')(z'-z'_{\mathrm{d}}))\ z' \in [z'_{\mathrm{d}},\ 1], \tag{4.19}$$

is assumed in the ascending limb. An exponential function was chosen as it is a simple, one-parameter function that has a similar shape to the NaCl concentration profile in the ascending limb with low arterial pressure, shown in Figure 4.4. β' is related to C'_3 via

$$C'_3 = C'(1,t') = C'_2(t')\exp(-\beta'(t)(1-z'_{\mathrm{d}})). \tag{4.20}$$

This mathematical model was developed in the same manner as with the linear approximation previously. The only change was the substitution of the exponential profile, (4.19), into (4.3) instead of the linear profile, (4.6). The substitution

of the exponential function gives

$$\begin{aligned} -\frac{1}{\beta'}\frac{\partial C_2'}{\partial t'}(1-\exp(-\beta'(1-z_{\mathrm{d}}'))) - \\ C_2'\frac{\partial \beta'}{\partial t'}\left((1+\beta'\left(1-z_{\mathrm{d}}'\right))\exp\left(-\beta'\left(1-z_{\mathrm{d}}'\right)\right)-1\right) = \\ -\left(\left(Q_{\mathrm{i+1}}'C_{\mathrm{i+1}}'-Q_{\mathrm{i}}'C_{\mathrm{i}}'\right)+\int_{z_{\mathrm{i}}'}^{z_{\mathrm{i+1}}'} J_{\mathrm{s}}'\mathrm{d}z'\right), \end{aligned} \tag{4.21}$$

which can be rearranged to give $\partial\beta'/\partial t'$. The exponential approximation is also substituted into the expression for the solute flux in the ascending limb, (4.4). The rest of the model remained unchanged.

An exponential function of this form also has the property that C_3' can never be negative, as long as $C_2' > 0$, as is clear from (4.20). This resolves the shortcoming of the linear approximation giving a negative macula densa NaCl concentration. Figure 4.6 shows the results of the model with the exponential function at low mean arterial pressure. The NaCl concentration at the macula densa is positive, unlike the results of the linear approximation shown as a dashed line in Figure 4.4. The approximation to the PDE model is not as good as with high mean arterial pressure, but better than with a linear profile.

As well as high mean arterial pressure, the exponential ascending limb model also approximates the spatial profiles of the PDE tubular at regular mean arterial pressure. The exponential ascending limb model will be used in the remainder of this thesis, although many of the results still hold for the linear approximation.

4.1.5 ODE-PDE comparison - transient behaviour

For every parameter set tested the noncompliant model with the ODE tubular model exhibited damped oscillations in response to a 5 mmHg pressure step as shown in Figure 4.7.

This was consistent with the damped oscillations exhibited by the noncompliant model with the PDE tubular model presented in Chapter 3 and as shown in Figure 3.4. An extensive parameter search was undertaken both by looking at the eigenvalues of the Jacobian matrix and by numerical integration forward in

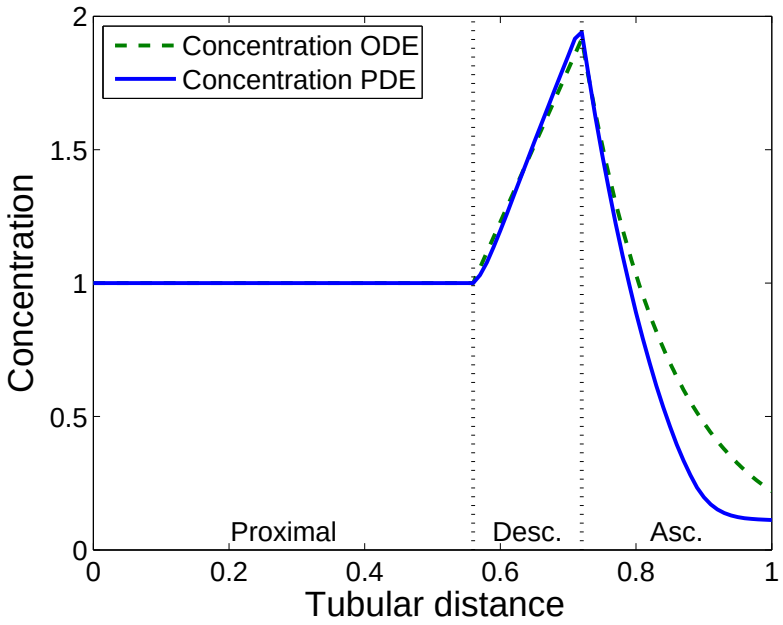

Figure 4.6 NaCl concentration profiles from **noncompliant** ODE and PDE tubular models at low mean arterial pressure ($P'_{\mathrm{MAP}} = 0.85P'_{\mathrm{MAP}}$) with an exponential approximation for the ascending limb NaCl concentration.

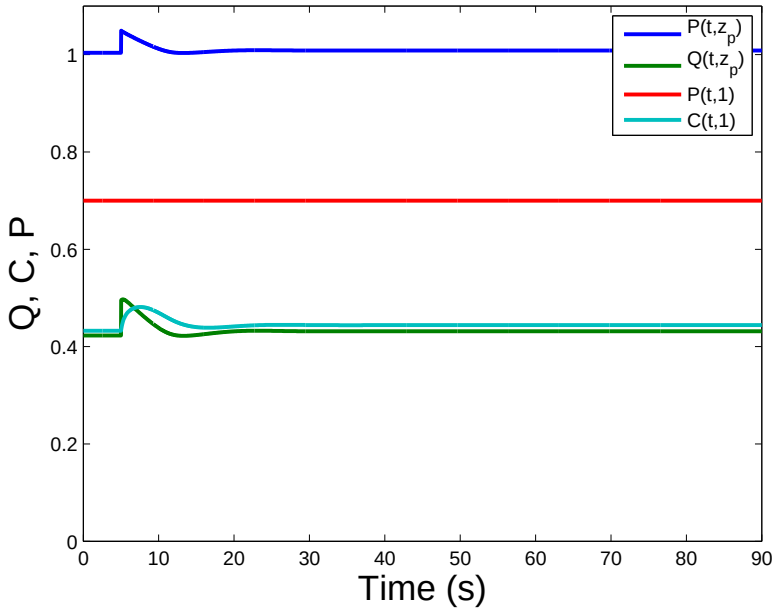

Figure 4.7 Damped oscillations in a single nephron model with a **noncompliant** ODE tubular model ($\gamma'_1 = 0$, $k' = 120$, $C'_{1/2} = 0.45$). This figure shows flow and pressure at the end of the proximal tubule and pressure and NaCl concentration at the macula densa. These variables were chosen as they are the most commonly reported experimental values.

time. The Jacobian matrix of the ODE system was given by

$$J = \begin{bmatrix} \frac{\partial}{\partial C_1'} \\ \frac{\partial}{\partial C_2'} \\ \frac{\partial}{\partial C_3'} \\ \frac{\partial}{\partial R_a'} \end{bmatrix} \begin{bmatrix} \frac{\partial C_1'}{\partial t'} & \frac{\partial C_2'}{\partial t'} & \frac{\partial C_3'}{\partial t'} & \frac{\partial R_a'}{\partial t'} \end{bmatrix}, \tag{4.22}$$

where matrix multiplication is assumed. The Jacobian matrix was calculated analytically then the eigenvalues, at the steady state, were calculated numerically using MATLAB's eigs function. The steady state of the system is stable when all the real parts of the eigenvalues are negative and unstable when at least one of the real parts of the eigenvalues are positive.

The noncompliant single nephron model with ODE tubular model was stable for every parameter set tested. Stability was tested by looking at the eigenvalues of the Jacobian matrix evaluated at the steady state and by integration forward in time. Eigenvalues with positive real part were never encountered. The time integration always converged to the steady state after a pressure perturbation. This is consistent with the PDE noncompliant model.

4.2 SIMPLIFIED COMPLIANT MODEL

This section presents the compliant ODE tubule model approximation and the compliant PDE tubule model and a comparison between the two models. The compliant ODE tubule model was constructed in a similar way to the noncompliant ODE tubule model presented in the previous section. Assuming spatial profiles and integrating along the length of the tubule removes the dependency on the spatial coordinate leaving only the time coordinate. The main difference between the derivation of the compliant and the noncompliant ODE models is that a pressure profile also had to be assumed in the compliant system, as the pressure determines the tubule radius via (3.27).

4.2.1 PDE tubule model

The compliant tubule model (3.38) is given by

$$2\gamma' R' \frac{\partial P'}{\partial t'} + \frac{\partial Q'}{\partial z'} = -J'_{\mathrm{v}}, \tag{4.23}$$

$$\frac{\partial P'}{\partial z'} = -\left(\frac{8\mu L Q_{\mathrm{ref}}}{\pi P_{\mathrm{ref}} r_0^4}\right) \frac{Q'}{R'^4}, \text{ and} \tag{4.24}$$

$$\frac{\partial \left(R'^2 C'\right)}{\partial t'} = -\frac{1}{2}\frac{\partial \left(Q'C'\right)}{\partial z'} - J'_{\mathrm{s}}. \tag{4.25}$$

This model reduces to the noncompliant model when: $\gamma' = 0$ and $R' = 1$. The pressure is now time dependent and is no longer in a pseudo-steady state. Nonlinearities are introduced into the system on the right hand side of (4.24), left hand side of (4.25), and left hand side of (4.23).

The NaCl, J'_{s}, and volume, J'_{v}, fluxes are as given previously in this Chapter by (4.4) and (4.5), respectively. An expression for the motion of the tubule wall [28] is given by (3.27) as used in Chapter 3. This equation reduces to $R' = 1$ in the noncompliant case (γ'=0).

4.2.2 ODE tubule approximation

As before, linear profiles were assumed in the proximal and descending limbs for the NaCl concentration. An exponential profile was assumed in the ascending limb to avoid the problem of negative concentrations as explained in Section 4.1. In the compliant case the pressure also has time dynamics. Therefore it was necessary to assume a profile for the pressure. A linear pressure profile was assumed throughout the tubule. This single linear profile is justified by the pseudo-linear nature of the pressure profile from the PDE tubular model as shown in Figure 3.6.

The pressure profile was given by a first-order Lagrange interpolating polynomial,

$$P'(t', z') = (1 - z')P'_{\mathrm{b}}(t') + z'P'_{\mathrm{d}}(t'), \ 0 \le z' \le 1, \tag{4.26}$$

which is equivalent to the linear approximation used for the NaCl concentration, (4.6).

The compliant system contained many more terms than the noncompliant system due to the nonlinearities introduced with compliance. The solution process for the compliant system was checked against the noncompliant system by

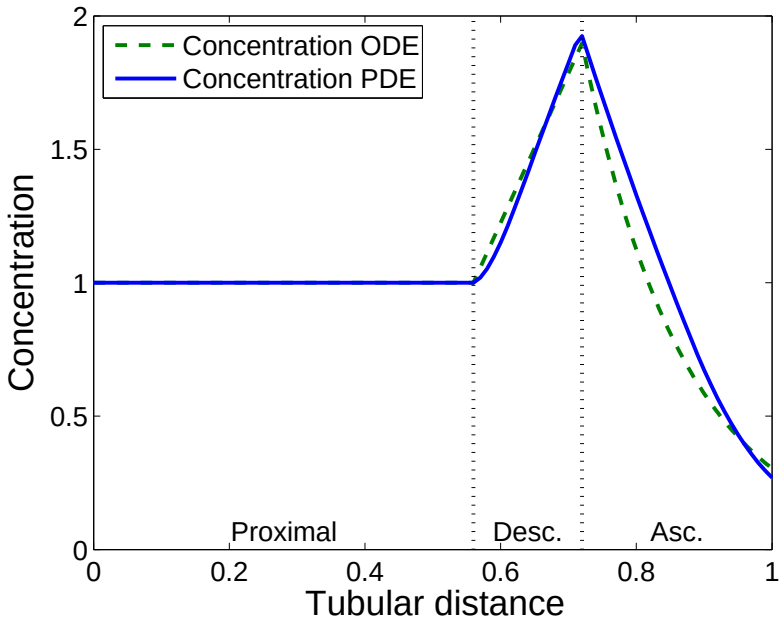

Figure 4.8 Steady state NaCl concentration profile comparison of the **compliant** PDE and ODE tubular models.

setting $\gamma' = 0$. The numerical procedure was also checked by letting $\gamma' \to 0$. The compliant results converged on the noncompliant results, adding support to the validity of the numerical solution process.

The actual ODEs are not shown here because they are very long and contain many terms.

4.2.3 ODE-PDE comparison - steady state

The steady state NaCl concentration profiles for the ODE and PDE compliant tubular models are shown in Figure 4.8. The steady state volume flow, pressure, and radius profiles for the ODE and PDE compliant tubular models are shown in Figure 4.9. The major difference between the compliant and noncompliant steady states was that the tubular radius profile is no longer constant. As in the noncompliant model, there is good agreement between the NaCl concentration at the macula densa in the ODE and PDE tubular models.

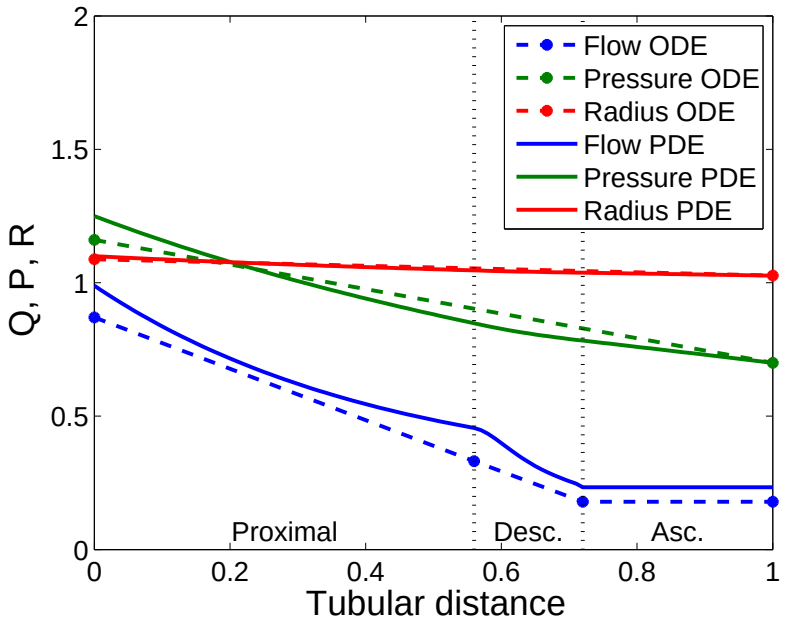

Figure 4.9 Steady state volume flow, pressure, and radius profile comparison of the **compliant** PDE and ODE tubular models.

4.2.4 ODE-PDE comparison - transient behaviour

Figure 4.10 shows oscillatory behaviour in the single nephron model with a compliant ODE tubular model. This behaviour occurred for a wide range of parameter values close to the experimentally based parameter set used by Holstein-Rathlou and Marsh [28]. The three parameters that were changed from those of Holstein-Rathlou and Marsh [28] to produce Figure 4.10 were $C'_{1/2}$, γ', and k'.

$C'_{1/2}$ was changed from 0.32 to 0.45 so that the operating point of the system was within the autoregulatory range. The NaCl concentration at the macula densa was higher for the exponential tubular model than for the PDE tubular model of Holstein-Rathlou and Marsh [28] as shown in Figure 4.8. Holstein-Rathlou and Marsh [28] also found that the operating point of the single nephron model must be on a steep portion of the autoregulatory curve, (3.34), for sustained oscillations.

The value of the compliance, γ'=1, is close to the range used by Holstein-Rathlou and Marsh [28] of [0.13, 0.665] and well within the range reported by Sakai et al. [64] of [0.133, 2.85] obtained experimentally.

$k' = 120$ was used to create Figure 4.10. The range used by Holstein-Rathlou

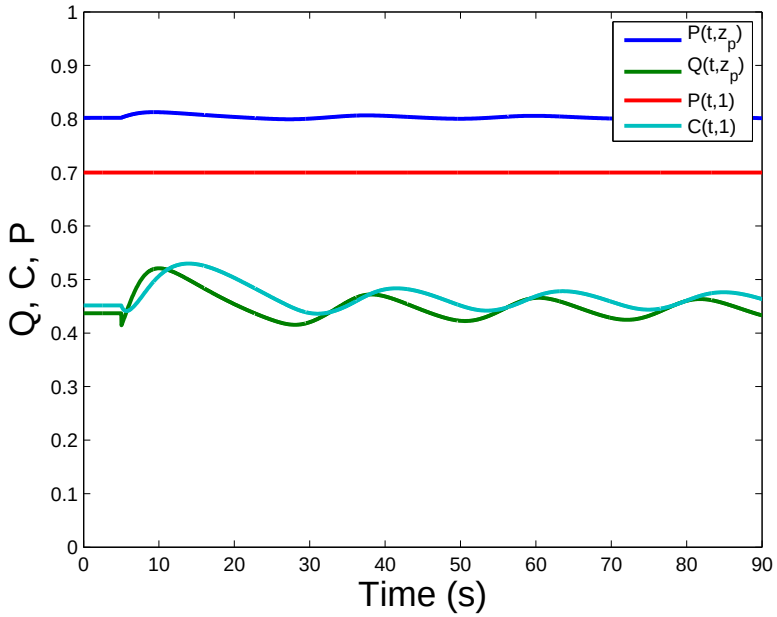

Figure 4.10 Sustained oscillations in the single nephron model with a **compliant**, ODE tubular model. ($\gamma' = 1$, $k' = 120$, $C'_{1/2} = 0.45$)

and Marsh [28] was [0, 60]. While this value is outside this range it is still reasonably close. Sustained oscillations were observed for lower values of k' as will be shown in the next section. Use of a linear approximation in the ascending limb, instead of the exponential, required a lower value of k' for sustained oscillations that was in the range 0–60 used by Holstein-Rathlou and Marsh [28].

4.3 BIFURCATION STUDY

Figure 4.11 shows the effect of varying compliance on the stability of the system. The real part of the eigenvalue with the largest real part becomes positive at approximately $\gamma' = 0.5$ and stays positive until approximately $\gamma' = 3$. The steady state is unstable in this region and the system exhibits oscillatory behaviour. The compliance of the tubule increases the delay between changes at the afferent arteriole and changes in NaCl concentration at the macula densa. This increased delay changes the behaviour of the system from damped oscillations to sustained oscillations. The system becomes stable at high values of γ' because the steady state moves out of the autoregulatory range. This shows good qualitative agreement with the results of the bifurcation study of the PDE model, shown in Figure 3.11. The change in sign of the real part of a complex pair of

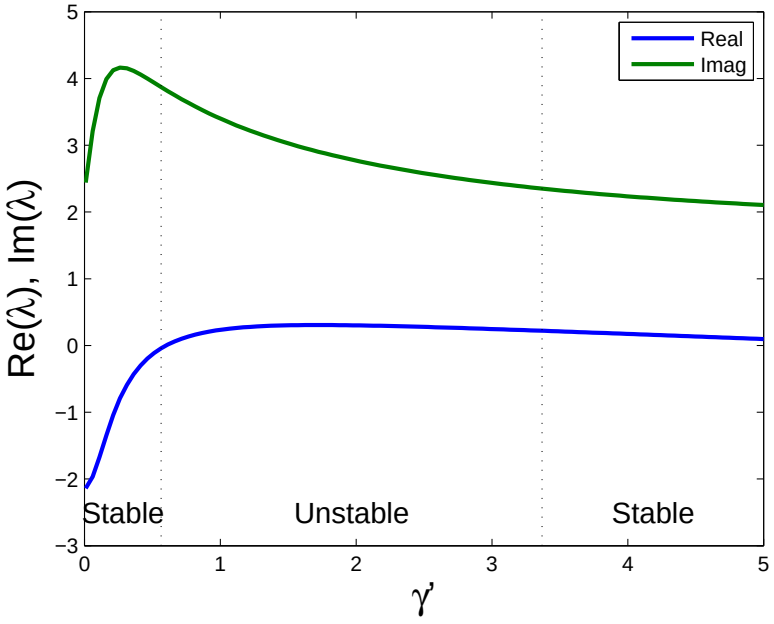

Figure 4.11 The eigenvalue with the largest real part of the Jacobian matrix evaluated at the steady state as compliance is varied ($C'_{1/2} = 0.45$, $k' = 125$).

eigenvalues at approximately $\gamma' = 0.5$ indicates a Hopf bifurcation. A necessary but insufficient condition for a Hopf bifurcation is that a pair of complex conjugate eigenvalues of the Jacobian matrix evaluated at the steady state must cross the imaginary axis.

Figure 4.12 shows the corresponding amplitude and frequency diagram to Figure 4.11. This figure was created by integrating the model forward in time. When the amplitude of the oscillations changed by less than 10^{-4} the oscillations were assumed to be stable. The frequency was calculated by dividing the total number of peaks by the time between the first and last peak. The stability of the system changes from stable to unstable to stable behaviour. This behaviour was also seen in the PDE model. The first change in behaviour can be explained by the additional delay caused by compliance. The additional delay changes the behaviour of the system from damped oscillations to sustained oscillations. The second change in behaviour occurs because of the position of the steady state on the TGF curve. High compliance lead to high flow as the tubule was distended that lead to high NaCl concentration at the macula densa. The steady state was no longer on a steep portion of the TGF curve, (3.34), and sustained oscillations were not exhibited.

Figure 4.13 shows the regions of parameter space where unstable and stable

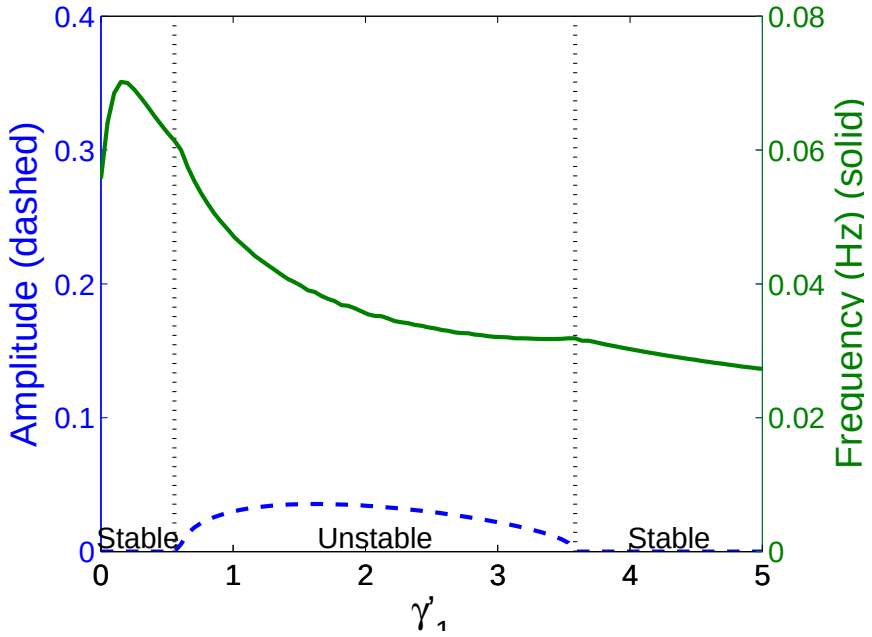

Figure 4.12 The effect of varying the tubule compliance on the frequency and amplitude of the oscillations ($C'_{1/2} = 0.45$, $k' = 125$).

behaviour was exhibited. This two-dimensional bifurcation diagram shows the effect of varying the compliance, γ', and TGF gain, k'. This diagram shows good qualitative agreement with results from the PDE model. For example, k' and γ' must be sufficiently large to produce sustained oscillations; with a fixed k', increasing γ' changes the stability of the steady state from stable to unstable back to stable. The noncompliant model, $\gamma' = 0$, does not exhibit sustained oscillation. Two dimensional bifurcation diagrams were not feasible with a PDE tubule model due to the high computational cost.

Figure 4.14 shows the effect of the slope of the TGF curve, (3.34), at the operating point on sustained oscillatory behaviour. The four subplots show the effect of the stability of the system by moving the inflection point, $C'_{1/2}$, of the autoregulatory curve, (3.34). The unstable oscillatory behaviour occurs over a wider range of parameter space as the inflection point is increased. The contour plots show the slope of the autoregulatory curve evaluated at the steady state for those values of γ', k', and $C'_{1/2}$. It is necessary that the slope must be greater that approximately 7 for oscillatory behaviour to occur.

The focus has been on the gain of the TGF mechanism because it a common bifurcation parameter in other studies. Compliance was also focused upon because it is not clear that it should cause a qualitative change in the behaviour

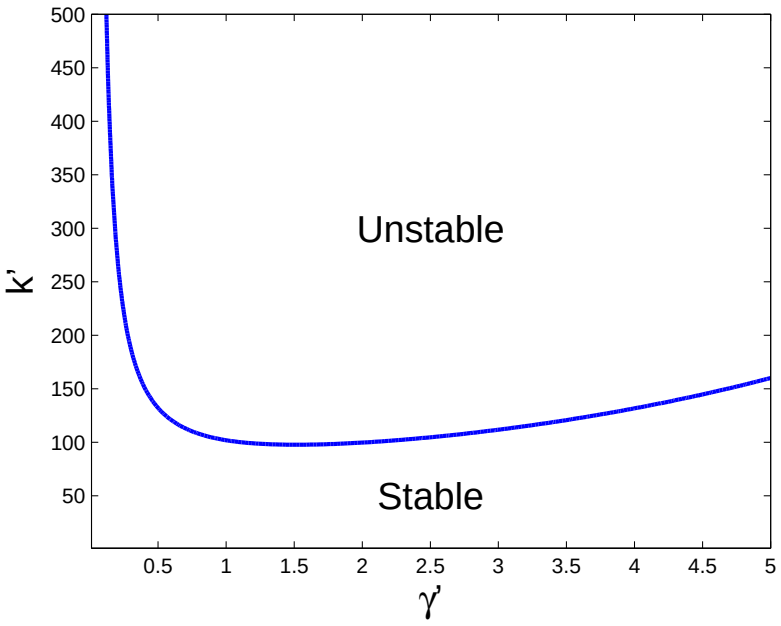

Figure 4.13 Regions of parameter space where the steady state is stable or unstable in the compliant ODE tubular model ($C'_{1/2} = 0.45$).

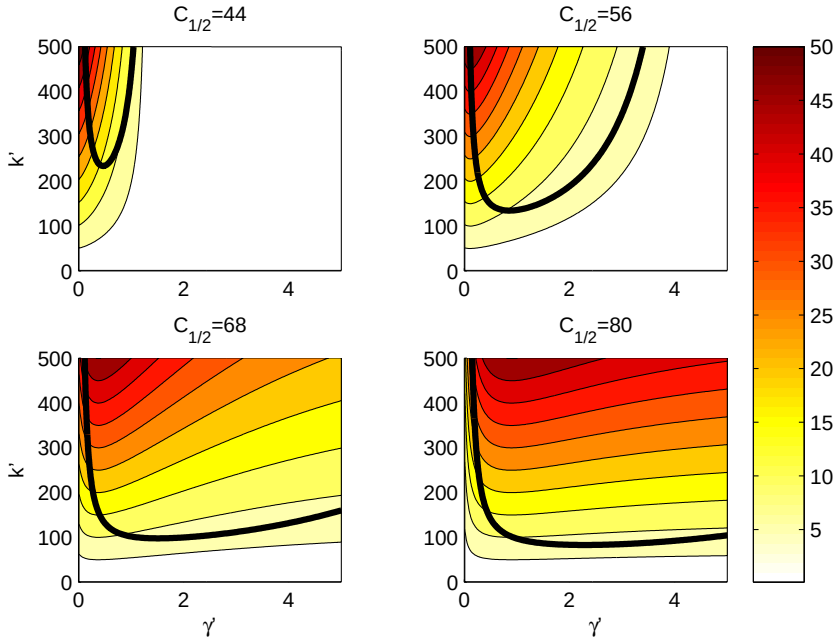

Figure 4.14 The effect of the slope of the TGF curve, (3.34), on the stability of the steady state. The coloured level curves show the slope of the TGF curve calculated at the steady state. The solid black lines show where the stability of the steady state changes.

of the system. However, there were other bifurcations in the system. The variation of some parameters caused a bifurcation because they moved the steady state away from a steep section of the TGF curve. For example, increasing κ' increased the volume reabsorption in proximal tubule. This meant that the volume flow was lower in the ascending limb and hence there was more time for NaCl to be reabsorbed from the tubule, decreasing the concentration of NaCl at the macula densa and moving the steady state away from a steep section of the curve. A parameter that has an expected affect on the bifurcation structure is the characteristic time of the TGF mechanism, t_0'. If t_0' was too small then the TGF mechanism reacted very slowly to a change in concentration at the macula densa and the steady state was stable.

4.4 DISCUSSION

In general, ODE models are easier to analyse and solve, and are less computationally expensive than PDE models. The stability of a steady state of an ODE model can be cheaply ascertained by examining the eigenvalues of the Jacobian matrix evaluated at the steady state. In general, this is much more difficult with a PDE model that has an infinite spectrum of eigenvalues, all of which must have a negative real part for stability.

The results from the PDE model and ODE model show good qualitative and quantitative comparison with each other when the PDE profiles are nearly linear. Low values of mean arterial pressure showed that the linear profile was not a good approximation as the PDE profile was nonlinear. This was rectified by using an exponential to represent the NaCl concentration in the ascending limb. Oscillatory behaviour in the ODE model occurs at a slightly higher value of compliance than for the PDE model. However, this value is still within the range of compliance values reported experimentally.

The ODE model supports the finding that oscillatory behaviour is unlikely in the noncompliant model. Significant analysis of the stability of the system was undertaken and no parameter set exhibited oscillatory behaviour. While this is inconclusive evidence that sustained oscillations do not exist in the ODE or PDE noncompliant tubule model, it supports the hypothesis that sustained oscillations are unlikely, or occur in such a small region of parameter space that they are unlikely to be exhibited *in vivo*. It was significantly easier to determine if the steady state was stable or unstable in the ODE model compared to the

PDE model. The availability of a Jacobian matrix with the ODE model made searching of parameter space significantly faster and more reliable.

The ODE model is also conceptually easier to understand and use. This makes the model more accessible to nonmathematicians such as clinicians. The savings in computational time made by the ODE model also make the model more useful to clinicians.

The ODE tubule model becomes a poorer representation of the PDE tubule model as the profile becomes less linear, for example when mean arterial pressure is low. The effects of this shortcoming can be alleviated by using an exponential approximation for the NaCl concentration in the ascending limb. Linear approximations are appropriate for the concentrations in the proximal tubule and the descending limb and the pressure for a wide range of physiologically realistic parameters. However, if these parameters are varied sufficiently then their profiles can also become nonlinear and the linear approximation will be a poor representation.

In summary, the linear and exponential approximations show good qualitative similarity to the computationally expensive PDE tubular model. The ODE tubular model exhibits sustained oscillations for similar areas of parameter space to the PDE tubular model. Compliance was again found to be important for sustained oscillations. The ODE tubular model requires far less computation time and effort than the PDE tubular model. It is also conceptually simpler making it more accessible to people who are unfamiliar with PDEs. The ODE model also permits a higher degree of mathematical analysis. Two-dimensional bifurcation diagrams can be readily computed for the ODE model where these would be an onerous, computationally expensive task using the PDE tubular model.

Chapter 5

NEPHRON MODEL WITH VARIABLE ARTERIAL PRESSURE

Sustained oscillations are unlikely to exist in the noncompliant single nephron model as presented in Chapter 3. Significant exploration of parameter space with a range of models and stability analysis techniques showed that sustained oscillations are unlikely, or exist in such a small domain of parameter space that they are unlikely to be encountered *in vivo*. However, the results of Chapters 3 and 4 have shown that the noncompliant model exhibits damped oscillations, at a frequency consistent with the tubuloglomerular feedback (TGF) mechanism, in response to a single relatively small pressure perturbation.

In reality, blood pressure varies constantly over a wide range of time scales from stimuli such as physical activity, circadian rhythm, the respiratory cycle, and heart beat. This chapter describes how sustained oscillations are elicited in the otherwise nonoscillatory noncompliant single nephron TGF model with either a periodic or non-periodic pressure forcing. The oscillations have a frequency of approximately 0.05 Hz. This frequency compares well with the experimentally observed frequency of the oscillations attributed to the operation of the TGF mechanism. Periodic pressure forcing was simulated by varying the inlet pressure, P_{a}, as a square wave. Periodic forcing simulates regular pressure perturbations such as heart beat or breathing. The frequency of the periodic forcing was significantly faster than those resulting from the TGF oscillations. A typical forcing frequency was 0.25 Hz. This is faster than the TGF oscillations exhibited by the model, which typically had a frequency of approximately 0.05 Hz. A wide range of forcing frequencies elicited sustained oscillations. As expected, sustained oscillations were still exhibited by the oscillatory compliant single nephron model with either periodic or non-periodic pressure forcing. A non-periodic pressure forcing was simulated with a mean reverting white noise process. A white noise

process models the wide frequency content of arterial pressure variations that has been observed experimentally [71]. White noise forcing also elicited sustained oscillations.

5.1 PERIODIC PRESSURE FORCING

In contrast to the slower TGF generated oscillations, significantly faster periodic blood pressure perturbations have been observed experimentally at the vascular level of the afferent arteriole. These pressure perturbations arise from several independent naturally occurring and artificial sources. For example, Yip et al. [74] found that a periodic pressure perturbation at 1 Hz exists at the level of the afferent arteriole due to respiration. Single nephron pressure and sodium chloride (NaCl) concentration time series are often passed through low-pass filters to remove high frequency fluctuations. For example, Yip et al. [74] passed data through a Kaiser-Bessel low-pass filter to remove a strong signal from respiration. Experimental results from Loutzenhiser et al. [52] indicated that pressure perturbations from heart beat, with a frequency of approximately 6 Hz, were found in the afferent arteriole. A experimental setup for measuring the flow rate, presented in [12], periodically injected a small amount of fluid containing boluses that were tracked by video. This widely used experimental method introduces an artificial periodic pressure perturbation. Variations in blood vessel diameter at a frequency of 0.5 Hz have been observed experimentally and in a mathematical model presented in Gonzalez-Fernandez and Ermentrout [18], due to interaction between calcium and potassium trans-sarcolemma fluxes in smooth muscle cells.

5.1.1 Model

Two types of inlet pressure conditions have been used so far in this thesis: a constant and a pressure step increase. In this section, the artificial and naturally occurring periodic pressure variations were modelled using a periodic function for the inlet pressure, P_{a}. The remainder of the model was the same as presented in Chapter 3 and the constant downstream pressure boundary condition, (3.35), was used. Briefly, the single nephron TGF model was comprised of three sub-models: glomerular, tubular, and TGF sub-models. For a full description of these models see Section 3.1. The nonoscillatory noncompliant model was used in this chapter to determine if sustained oscillations could be elicited in a nonoscillatory

nephron through interaction between a realistic pressure forcing and the time delay around the loop of Henle.

A periodic pressure forcing simulates a regular pressure perturbation from heart beat, respiration, or experimental procedure and was modelled using two simple periodic waveforms: a square wave and a sine wave. Both waves were centred around mean arterial pressure, P'_{MAP}. A typical amplitude was $0.1P'_{\mathrm{MAP}}$, approximately half the difference between systolic and diastolic pressure [68]. The effect of a range of forcing frequencies was investigated.

5.1.2 Results

Figure 5.1 shows time series of the NaCl concentration at the macula densa for the case where arterial pressure, P_{a}, was varied as a square wave with a frequency of 0.25 Hz (results for a sine wave of the same frequency are similar). Transient behaviour was removed by discarding the first four minutes of simulated data. The forcing can be identified in the time series as the sharp peaks every 2 s. In addition to the high-frequency forcing oscillations, there were sustained low-frequency oscillations with a frequency of approximately 0.06 Hz. Corresponding oscillations were observed in the resistance of the afferent arteriole and the flow and pressure in the renal tubule. As discussed in Chapter 3 the low-frequency oscillations were present, but were not sustained, without the periodic variation of the inlet pressure. The TGF mechanism was removed by setting R_a =constant instead of (3.33). The low-frequency oscillations did not occur and only the oscillations corresponding to the high forcing frequency were present. Hence, both an active TGF mechanism and a nonconstant arterial inlet pressure were required for sustained 0.06 Hz oscillations to occur. It is likely that the oscillations arise as a result of the interaction of these two factors. In addition, if the TGF gain, k', was too low, $k' \leq 280$, then sustained oscillations were not exhibited.

Figure 5.2 shows a Fourier transform of the NaCl concentration time series shown in Figure 5.1, which was computed using MATLAB's periodogram function. The peak at 0.25 Hz corresponds to the forcing frequency, whilst the peak at approximately 0.06 Hz corresponds to the slower oscillations whose frequency was consistent with the experimentally observed TGF frequency. The resonant frequencies of the TGF frequency can also be seen, although these are several orders of magnitude smaller in power than the peaks at the forcing and TGF frequencies. The peak at approximately 0.06 Hz disappears when the TGF mechanism is disabled by setting R_{a}=constant, shown in Figure 5.2 as a dashed line.

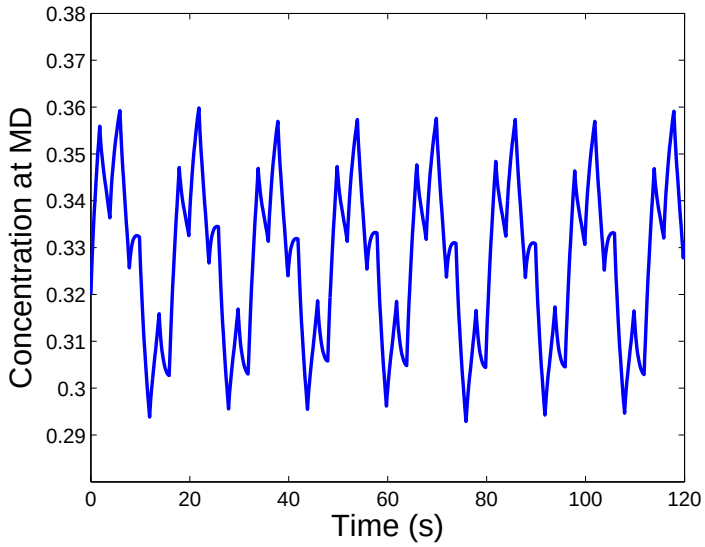

Figure 5.1 The nondimensional NaCl concentration at the macula densa ($k' = 300$, $\gamma' = 0$), with a periodic inlet pressure variation at 0.25 Hz. Sustained low-frequency oscillations are exhibited at approximately 0.06 Hz, consistent with the frequency of TGF. Superimposed on the low-frequency oscillations are higher-frequency oscillations, corresponding to the forcing frequency.

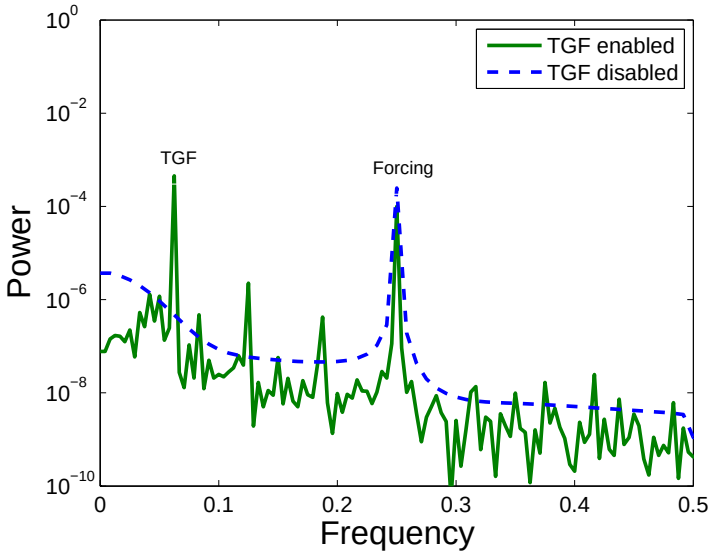

Figure 5.2 Fourier transform of the macula densa NaCl concentration time series ($k' = 300$, $\gamma' = 0$): with an intact TGF (solid); and without TGF (dashed). The solid line is the Fourier transform of the time series in Figure 5.1. The forcing frequency can be identified at 0.25 Hz and oscillations attributed to TGF identified at 0.06 Hz. Note that without the TGF mechanism (dashed line), there is no spike in power at approximately 0.06 Hz. 0.25 Hzis very close to a resonant frequency of the system.

Periodic pressure perturbations are exhibited at the vascular level of the afferent arteriole over a range of frequencies [74, 18]. Frequencies range from the relatively fast heart rate at 6 Hz, down to the slower vasomotion of the afferent arteriole at 0.5 Hz. Figure 5.3 shows the effect of varying the period of the pressure forcing, (period in), on the periods exhibited in the NaCl concentration time series, (period out). Each vertical strip is a Fourier transform of sixteen minutes of simulated macula densa NaCl concentration at the corresponding forcing period, (period in). The first four minutes of simulated data were discarded to remove transient behaviour. For example, the Fourier transform shown in Figure 5.2 is positioned vertically above (period in)=4 s which corresponds to a forcing frequency of 0.25 Hz. The peaks in Figure 5.2 at 0.06 Hz and 0.25 Hz correspond to the dark areas in Figure 5.3 above (period in)=4 s at approximately 16 s and 4 s respectively. The dark band along the line (period in) = (period out) shows the period of the pressure forcing exhibited in every NaCl concentration time series. The dashed lines show the resonant frequencies of the forcing frequency. In the areas of the plot where these resonant frequencies intersect with the horizontal band at approximately 16 s, i.e., the natural period of the nephron, the power is increased. This indicates the innate excitability of the system at its natural period.

5.1.3 Discussion

It is hypothesised that naturally occurring variations in arterial blood pressure contribute to observed TGF-associated oscillations. Importantly, the model predicts that the period of the TGF-associated oscillations stays relatively constant as the periodic inlet forcing frequency is varied. This can be seen in Figure 5.3 as the roughly horizontal band at (period out) = 16 s. This implies that the sustained oscillations attributed to the TGF mechanism are robust with respect to the frequency of pressure variations.

It would be relatively easy to test this hypothesis experimentally. The naturally occurring fluctuations in blood pressure could be removed by blocking the afferent arteriole with a wax block and microperfusing tubular fluid downstream of the wax block at a constant flow and pressure. This would effectively remove any fluctuations in pressure or flow entering the nephron. Wax blocks were commonly inserted when examining the function of the kidney with a closed loop method and microperfusion is also routinely carried out to perturb the system. If the oscillations are not exhibited when the flow and pressure are held constant,

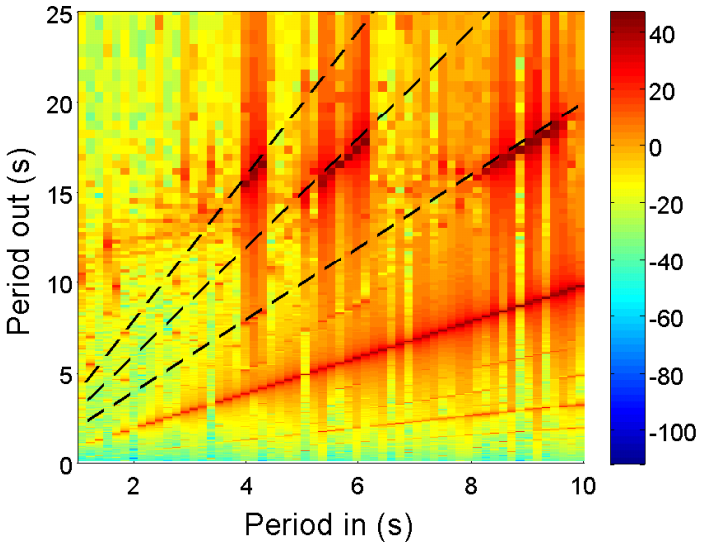

Figure 5.3 Periods in the macula densa NaCl concentration time series, (period out), as a function of the forcing period, (period in), for $k' = 300$ and $\gamma' = 0$. Dark areas indicate periods that are present in the time series when forced at (period in). The forcing period is always present in the time series, as indicated by the dark diagonal line (period in) = (period out). The dashed lines show the resonant frequencies of the forcing frequency. The horizontal band of high power at approximately (period out) = 16 s is present over a range of forcing periods from 1–10 s, and is consistent with the period of the TGF mechanism.

the naturally occurring blood fluctuations are likely to be contributing to the generation of sustained oscillations.

These sustained low-frequency oscillations are observed in the noncompliant model for a wide range of periodic pressure perturbation frequencies ranging from 0.1 Hz to 0.5 Hz. For periodic forcing frequencies above 0.5 Hz, the pressure is changing too rapidly for a signal capable of eliciting low-frequency oscillations to reach the macula densa, and the forcing frequency is the only strong frequency seen in the model solution. For frequencies lower than 0.1 Hz, the frequency attributed to the TGF mechanism becomes indistinguishable from the forcing frequency. An interesting result from the model is the clustering of sustained oscillations around the forcing period harmonics. While the sustained oscillations are present in the model for a range of forcing periods the intersection of a forcing harmonic and the natural period of the nephron is necessary to increase the amplitude of the sustained oscillations.

The parameter values used in this investigation are largely taken from Holstein-Rathlou and Marsh [28] and pertain to the rat. Both the vasomotion of the afferent arteriole, as discussed in Gonzalez-Fernandez and Ermentrout [18], and

experimental methods such as the method presented in Chou and Marsh [12] and used by Holstein-Rathlou and Marsh [27], could cause periodic perturbations in pressure at the afferent arteriole. Both of these frequencies fall in the range predicted by the model to elicit sustained oscillations at a frequency consistent with TGF. The heart rate of the rat is approximately 6 Hz [51]. A periodic inlet pressure perturbation at a frequency of 6 Hz is well above the frequency range that elicits TGF-associated sustained oscillations in this model. The respiratory rate of the rat, even with artificial ventilation of 1 Hz as employed in Yip et al. [74], also falls just above this range. Thus, the model predicts that it is unlikely that TGF-associated oscillations would be elicited by either heart beat or respiration in the rat. However, the frequencies of both vasomotion and experimental procedures fall within the general range predicted by this model to produce slow TGF oscillations.

5.2 WHITE NOISE PRESSURE FORCING

In the preceding section the inlet pressure to the single nephron model, developed in Chapter 3, was forced with a periodic function. This varies the inlet pressure to the system at one frequency. However, blood pressure has been shown to have a $1/f$ spectrum, implying a wide frequency content [71]. A $1/f$ spectrum means that the power spectral density of the signal is inversely proportional to the frequency. In contrast, a white noise process has a flat power spectral density. A $1/f$ spectrum means that slower, low frequency blood pressure oscillations have more energy than faster, high frequency oscillations.

5.2.1 Model

Three types of inlet pressure conditions have been used thus far in this thesis: a constant and a single step in pressure were used in Chapters 3 and 4 and a periodic pressure waveform was used in the preceding section. In the current section, naturally occurring pressure variations were modelled using a non-periodic function for the inlet pressure, P_{a}. The remainder of the model was the same as presented in Chapter 3. Refer to Section 3.1 for more details of this model. The nonoscillatory noncompliant model was used in this section to determine if sustained oscillations could be elicited in a nonoscillatory nephron through interaction between a realistic pressure forcing and the time delay around the loop of Henle.

Blood pressure exhibits a wide range of frequencies [29]. Indeed, studies have shown that under physiological conditions, the fluctuations in blood pressure have a $1/f$ spectrum [71]. A white noise process for P_{a} was used to force the system with equal power at every frequency, simulating the wide range of frequencies exhibited by blood pressure. A white noise process was used instead of the more realistic pink noise process, $1/f$, to simplify the modelling. This assumption is discussed in more detail in the discussion. A mean-reverting Ornstein-Uhlenbeck process was used to model the pressure. This process was chosen as the pressure remains close to mean arterial pressure in contrast to a generic white noise process. Details of the Ornstein-Uhlenbeck process and its numerical implementation with the Euler-Maruyama method can be found in Appendix A.

5.2.2 Results

As with the periodic pressure forcing, the white noise forcing caused a peak in power at 0.06 Hz corresponding to the natural frequency of the nephron, as shown in Figures 5.4 and 5.5. Sections of the time series, such as $t \in [250,\ 350]$ s, show excellent qualitative agreement with both experimental and modelling results. Within this section the oscillations are sustained and regular and there were oscillations in both the NaCl concentration at the macula densa and the pressure in the proximal tubule. While other sections of the time series, for example $t \in [50,\ 100]$ s, do not resemble regular oscillations, the underlying natural frequency of the oscillations was still present.

The compliant system forced with white noise is also oscillatory. The results from this model show excellent qualitative agreement with the experimental proximal pressure and distal NaCl concentration time series from Holstein-Rathlou and Marsh [27]. The experimental time series of Holstein-Rathlou and Marsh [27], shown in Figure 2.3, exhibits significant variation in the amplitude of the oscillations as well as in the mean value in both the proximal tubular pressure and distal tubule NaCl concentration time series. This is qualitatively captured in the time series from the compliant, white noise forced model and is a result of using a stochastic process for the arterial pressure, P_{a}.

5.2.3 Discussion

The noncompliant system exhibits damped oscillations for a wide range of parameter sets as shown in Chapter 3 and 4. Forcing with either a periodic or

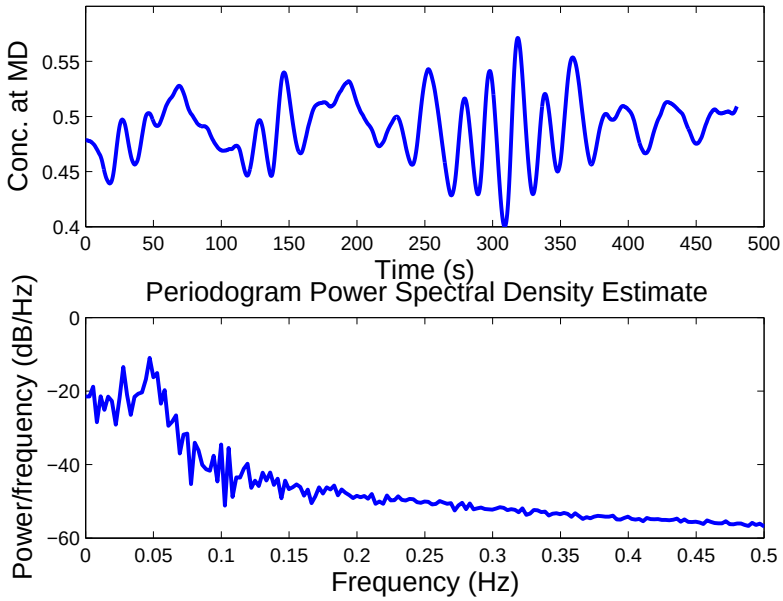

Figure 5.4 The NaCl concentration at the macula densa from the **noncompliant** single nephron model forced with a white noise process for the inlet pressure. The realisation of the white noise process used to create this Figure was also used to create Figure 5.5. The lower graph shows a power spectrum of the time series in the upper graph.

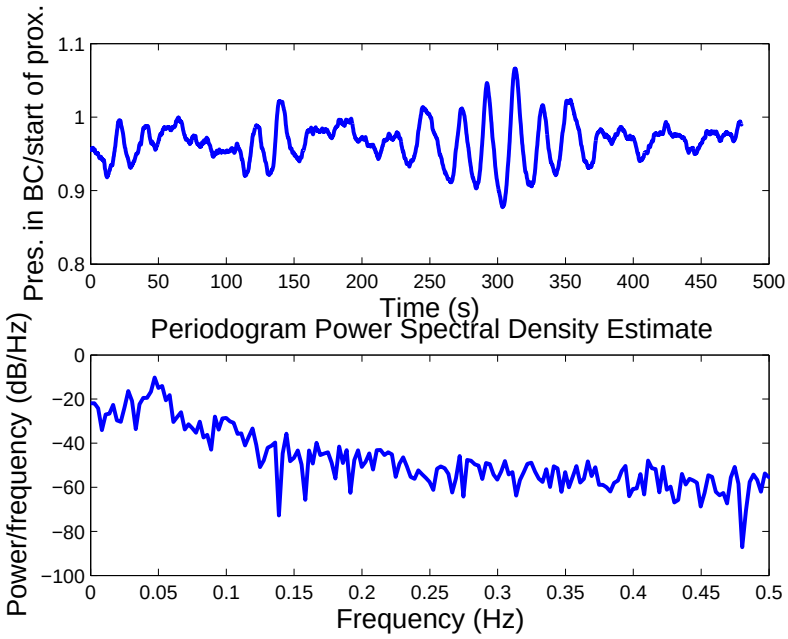

Figure 5.5 The proximal pressure from the **noncompliant** single nephron model forced with a white noise process for the inlet pressure. The realisation of the white noise process used to create this Figure was also used to create Figure 5.4. The lower graph shows a power spectrum of the time series in the upper graph.

white noise forcing elicits sustained oscillations. With a noncompliant tubule and a white noise forcing there was a peak in the Fourier transform at approximately 0.06 Hz but it was not as well defined as in the compliant case. A model from Sakai et al. [64] shows that a compliant nephron acts like a low pass filter attenuating frequencies above 0.1 Hz because of its compliance. This means that only low frequency flow and pressure perturbations reached the macula densa. In the noncompliant case the high frequency perturbations were not damped out before they reached the macula densa. Many high frequency perturbations were exhibited at the macula densa and a clear TGF response was not possible.

A white noise process was used to force the system at a wide range of frequencies. A white noise process has a flat power spectrum i.e., equal power at every frequency. Experimental evidence has shown that blood pressure fluctuations have a $1/f$ spectrum. This corresponds to a pink noise process. It is hypothesised that forcing the model with a pink noise process would produce a more clearly defined peak in power due to removing the high frequency fluctuations from the forcing. Pink noise could be approximated by passing white noise through a low pass filter.

In summary, the single nephron model with a noncompliant tubule model and a physiologically realistic first-order TGF model, was not inherently oscillatory as shown in Chapters 3 and 4. Sustained oscillations were exhibited if the noncompliant system was forced with a periodic or mean-reverting stochastic forcing. The compliant model was intrinsically oscillatory with or without forcing and oscillated at a frequency governed by the TGF and not the forcing. The most physiologically realistic model, compliant with white noise forcing, shows the best agreement with the experimental time series from Holstein-Rathlou and Marsh [27].

Chapter 6

MODEL EXTENSIONS

6.1 DELAY

There are three significant delays in the tubuloglomerular feedback (TGF) loop of a single nephron. In chronological order:

- The delay between a change in the resistance of the afferent arteriole and a change in the sodium chloride (NaCl) concentration at the macula densa.
- The transmission delay as information is passed between the cells of the macula densa and the afferent arteriole [26].
- The delay as the smooth muscle cells of the afferent arteriole constrict or dilate.

In some TGF models [2, 66] all three delays are lumped into one parameter. This combined delay is often modelled by a system of differential equations, most commonly a system equivalent to a third-order differential equation. While this greatly simplifies the solution process, important aspects of the *in vivo* system, such as the temporal characteristics of the tubule, are lost. The total delay is often used as a bifurcation parameter. As expected, typical results show that if the delay is large enough then the system exhibits sustained oscillations. These types of models provide insight into the effect of the size of the delay on the behaviour of the system. However, they cannot capture the variability in the delays. For example, the size of the first delay depends on the speed of the flow, which is variable, and the third delay depends on the properties of the afferent arteriole.

In the single nephron TGF model, the first delay is already intrinsic to the partial differential equation (PDE) or ordinary differential equation (ODE) tubu-

lar model presented in Chapters 3 and 4, respectively. Changes at the upstream-end of the tubule take a few seconds to propagate downstream due to the temporal characteristics of the models. The third delay was modelled by the first-order differential equation, (3.33), presented in Chapter 3. This provides a first-order response as the resistance of the afferent arteriole reverts to the target resistance, R_{a}^{*}, with a characteristic time scale, t_0'. The second delay, which has not been represented in the previous chapters, is modelled in this chapter as a pure delay of τ. In relation to this model, a pure delay is a period of time following a change in the NaCl concentration at the macula densa during which there is no change in R_{a} [5].

This delay occurs as information is passed across the juxtaglomerular apparatus by paracrine signalling [39]. Casellas and Moore [9] experimentally observed an average time of 4.5±0.5 s from a change in NaCl concentration at the macula densa to full vasoconstriction or vasodilation of the afferent arteriole. This was comprised of a pure delay of 2 s followed by an adjustment to maximal arterial tone over 2–3 s. Mathematical models, such as those reported by Layton et al. [42, 44], used a pure delay of 2 s followed by a distributed delay of 3 s that is based on the experimental results of Casellas and Moore [9]. The model in this thesis uses a first-order response to model the distributed delay.

6.1.1 Model

The transmission delay across the juxtaglomerular apparatus was modelled by delaying the signal to the site of TGF actuation at the afferent arteriole by τ. Instead of using the current NaCl concentration at the macula densa, $C(t, 1)$, as the signal to the TGF mechanism, as used in previous chapters, the delayed NaCl concentration, $C(t - \tau, 1)$, was used, namely

$$C_{\mathrm{md}}(t) = C(t - \tau, 1), \tag{6.1}$$

where τ was the time delay, C was the NaCl concentration at the macula densa, and C_{md} was the signal to the TGF mechanism. This delayed NaCl concentration was applied to the system through (3.33) and (3.34). The remainder of the model was as presented in Chapter 3. Both downstream pressure boundary conditions were used. Noncompliant and compliant versions of both the PDE and ODE tubular models were used to determine the effect of the delayed signal.

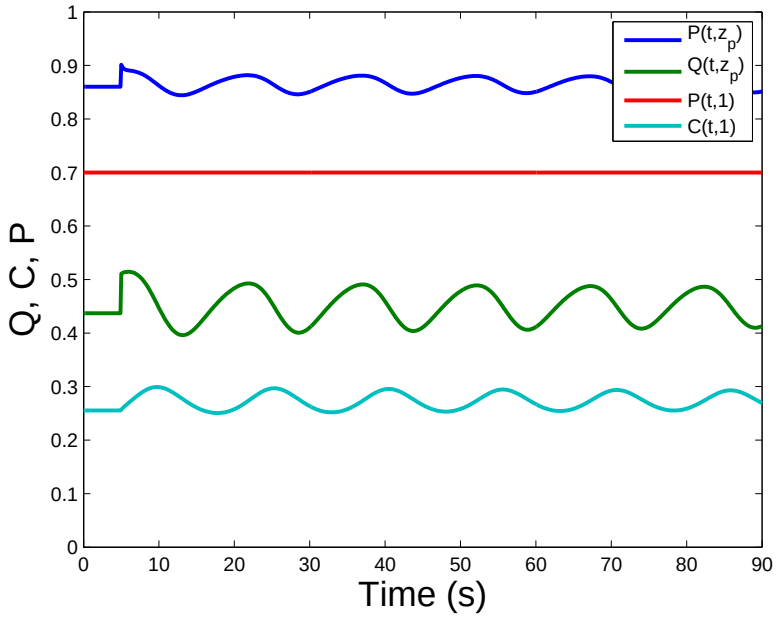

Figure 6.1 Sustained oscillations in a single nephron TGF model with a **noncompliant** tubule and juxtaglomerular delay of 1 s.

6.1.2 Results

Adding a small pure delay evoked sustained oscillatory behaviour in an otherwise nonoscillatory noncompliant single nephron model with a PDE or ODE tubular model. Figure 6.1 shows a time series of the single nephron model with noncompliant tubule and delay of 1 s. Without the delay the noncompliant model is nonoscillatory as shown in Chapter 3.

As expected, the oscillatory single nephron model with compliant tubule still exhibited sustained oscillations. Figure 6.2 shows a time series of the single nephron model with compliant tubule and juxtaglomerular delay of 1 s. Also as expected, the period increased by approximately 4 s and the amplitude increased. The addition of a 1 s delay allows an overshoot at the peak taking 1 s compared to the nondelayed system. This overshoot takes approximately 1 s to return to the previous maximum. This overshoot also occurs at the trough and in total adds 4 s to the period, compared to the nondelayed model. The increased amplitude is also explained by the overshoot due to the delay.

The delay was varied between 0–4 s to determine the effect on the behaviour of the noncompliant system, shown in Figure 6.3. This range contains the values reported experimentally [9] and used in other mathematical models [42]. Damped

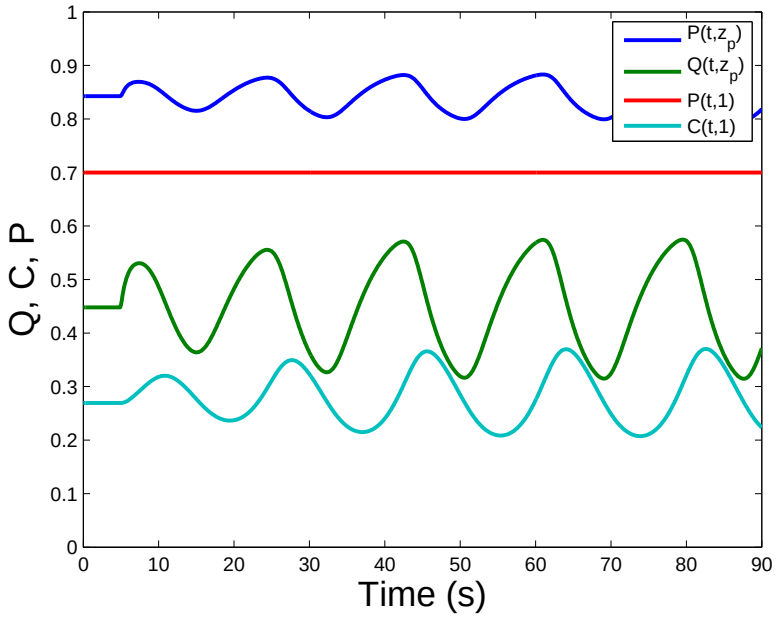

Figure 6.2 Sustained oscillations in single nephron TGF model with a **compliant** tubule and juxtaglomerular delay of 1 s. Figure 3.7 shows the results without the delay.

behaviour is exhibited by the model for delay values below approximately 1 s and sustained oscillatory behaviour is exhibited above this value. The shape of the amplitude curve likely indicates a Hopf bifurcation. To be certain that this system exhibits a Hopf bifurcation the eigenvalues of this model, containing a PDE with delays, would need to be checked for a change in sign of the real part of a complex conjugate pair of eigenvalues.

Adding a delay to the single nephron model with noncompliant ODE tubular model gave similar results to using the noncompliant PDE tubular model. Although a much larger delay of approximately 6 s was necessary for the system to exhibit sustained oscillations. A delay of this size is relatively large compared to the period of the oscillations as well as being physiologically unrealistic.

The delay was also varied in the single nephron model with the compliant PDE tubular model and the results are shown in Figure 6.4. As shown in Chapter 3, this model is oscillatory without any delay. The model remained oscillatory as the delay was increased through 0–4 s. As expected, the frequency of the oscillations decreased with increasing delay.

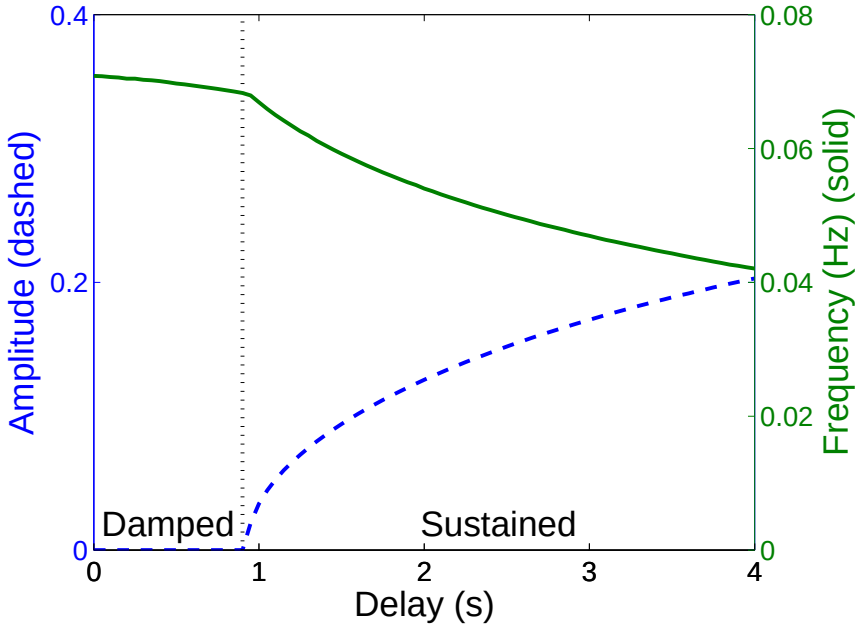

Figure 6.3 Effect of varying the delay, τ, on the frequency and amplitude of the oscillations in the **noncompliant** model.

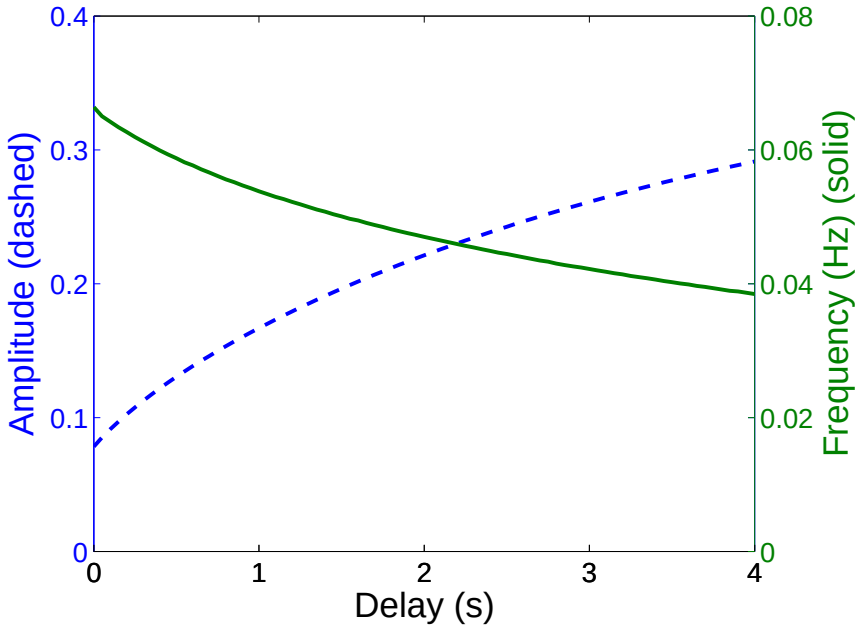

Figure 6.4 Effect of varying the delay, τ, on the frequency and amplitude of the oscillations in the **compliant** model.

6.1.3 Discussion

The delay was added to this model to represent the time for a signal to pass across the juxtaglomerular apparatus. The stability of many systems can be changed by adding or varying a delay in one or more model variables [19]. The size of the delay, 1 s, was small compared to the period of the oscillations, 20 s. This indicates that the oscillations are not caused solely by the pure delay, but by the interaction between the pure delay and other factors already inherent in the system.

Most of the TGF signalling mechanism between the macula densa cells and the cells of the afferent arteriole is well characterised [38]. The delay between the macula densa and the afferent arteriole can be modelled by a cellular model of the macula densa cells. This model would consist of several ODEs for intracellular concentrations of sodium, chloride, and calcium; cell volume; and cell potential.

In summary, a small delay in the otherwise nonoscillatory noncompliant model with a PDE or ODE tubular model induced sustained oscillations. The delay was physiologically motivated experimentally and corresponded to the pure delay as information is transmitted across the juxtaglomerular apparatus. The oscillatory compliant model remained oscillatory after adding a small delay, and the amplitude and period of the oscillations were increased.

6.2 VARIABLE INTERSTITIAL NACL CONCENTRATION

The model described in this section builds on the tubular model of Chapter 3 by replacing the constant interstitial NaCl profile with a partial differential equation (PDE) that describes the sodium chloride (NaCl) concentration in the interstitium and vasa recta. A fixed interstitial NaCl concentration profile used by [28, 45] and in Chapters 3 and 4 is used to simplify the modelling. In reality, the interstitial NaCl concentration profile is created and maintained by the close hairpin arrangement of the descending and ascending limbs of the loop of Henle and their different transport properties. Hence, the interstitial NaCl concentration profile is not fixed and depends on, for example, the strength of the Na-K-2Cl cotransporter in the ascending limb and the water permeability of the descending limb.

The tubules of the vasa recta are intertwined around the loops of Henle.

Their role is to return constituents that are reabsorbed by the proximal tubules and loops of Henle back to the body [17]. Under normal intake of fluids, most of the filtered water is reabsorbed. Thus, the vasa recta transports approximately the same volume of material that was filtered by the glomerulus and entered the renal tubule. The space around the vasa recta and loops of Henle is called the interstitium and comprises less than 10% of the renal volume.

The countercurrent mechanism creates and maintains a NaCl concentration gradient in the interstitium. The NaCl concentration in the interstitium increases with increasing depth from the surface of the kidney.

The model developed in this section only models the noncompliant tubule of a single nephron and does not include a glomerular or a TGF model. The TGF and glomerular models were not included in this model to determine the effects of a variable interstitial NaCl concentration without their confounding effects. The noncompliant tubule model was chosen as NaCl concentration and flow can be calculated independently of pressure, as shown in (3.39). This simplifies the solution process while still allowing comparison with the noncompliant profiles of Chapter 3.

6.2.1 Model

The NaCl concentration is assumed to be the same in the vasa recta and the interstitium. This assumption is valid due to the high water permeability of the vasa recta walls [58]. Water rapidly passes over the wall of the vasa recta via osmosis and quickly eliminates any NaCl concentration difference across the wall. This allows the vasa recta and interstitium to be modelled with a single NaCl concentration that simplifies the modelling. For the remainder of this section the vasa recta is combined into the interstitium.

The important difference between the model presented in this section and the model presented in Chapter 3 is the replacement of a fixed interstitial NaCl concentration profile with a PDE. The PDE for the interstitial NaCl concentration, C'_{I}, is given by

$$\frac{\partial C'_{\mathrm{I}}}{\partial t'} = J'_{\mathrm{s}}(z') + J'_{\mathrm{s}}\left(\frac{z'-z'_{\mathrm{p}}}{z'_{\mathrm{d}}-z'_{\mathrm{p}}}z'_{\mathrm{d}} + \frac{z'-z'_{\mathrm{d}}}{z'_{\mathrm{p}}-z'_{\mathrm{d}}}z'_{\mathrm{a}}\right) - v'C'_{\mathrm{I}},\ z' \in [z'_{\mathrm{p}},\ z'_{\mathrm{d}}], \tag{6.2}$$

where J'_{s} is the solute flux and z'_{p}, z'_{d}, z'_{a} are the ends of the proximal tubule, descending limb, and ascending limb, respectively. A diffusion term could be

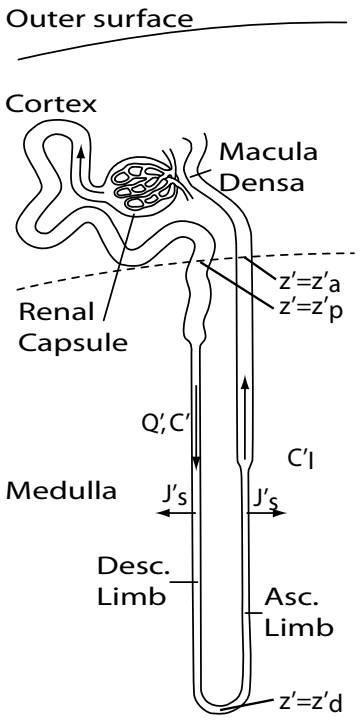

Figure 6.5 Single nephron anatomy showing the pertinent variables. C' and Q' are the luminal NaCl concentration and flows, respectively, C'_{I} is the interstitial NaCl concentration, and J'_{s} is the solute flux.

included in (6.2). However, its effect was expected to be small and it was not included. If the diffusion term was large the experimentally observed gradient would not be able to be set up.

The first and second terms on the right hand side are the solute flux from the descending and ascending limb, respectively. For each value of $z' \in [z'_{\mathrm{p}},\ z'_{\mathrm{d}}]$ there is a contribution to the interstitial NaCl concentration from both the descending and ascending limbs, as shown in Figure 6.5. The second term looks complicated, but it simply ensures that the contribution from the ascending limb is spatially matched with the contribution from the descending limb. For example, at $z' = z'_{\mathrm{p}}$ there is a contribution from the start of the descending limb, $J'_{\mathrm{s}}(z'_{\mathrm{p}})$, and a contribution from the end of the ascending limb, $J'_{\mathrm{s}}(z'_{\mathrm{a}})$. The last term models the convection of the reabsorbed NaCl in the vasa recta. Without this term the NaCl concentration would increase without bound due to the active transport in the ascending limb. In the remaining medullary section, $z' \in [z'_{\mathrm{a}},\ 1]$, the interstitial NaCl concentration is constant, $C'_{\mathrm{I}} = 1$, as in the fixed NaCl concentration profile in Chapter 3.

J_s is defined, as it was in Chapter 3, as

$$J'_s = \begin{cases} C'_{in}\kappa' \exp(-\theta' z') & 0 \le z' < z'_p \text{ (proximal tubule)}, \\ L'_s(C' - C'_I(z)) & z'_p \le z' < z'_d \text{ (descending limb)}, \\ L'_s(C' - C'_I(z)) + \frac{V'_{max}C'}{K'_m + C'} & z'_d \le z' \le 1 \text{ (ascending limb)}. \end{cases} \tag{6.3}$$

where the NaCl transport is modelled by a decaying exponential in the proximal tubule, osmosis in the descending limb, and as the sum of an osmotic term and a active Michaelis-Menten term in the ascending limb.

Equation (6.2) replaces the fixed interstitial NaCl concentration profile used by [28] and in previous chapters. Holstein-Rathlou and Marsh [28] used a piecewise linear function that increased from $C'_I(z'_p) = 1$ at the end of the proximal tubule to $C'_I(z'_d) = 2$ at the bottom of the loop of Henle. The fixed interstitial profile then decreased to $C'_I(z'_a) = 1$ at the end of the ascending limb and remained constant at $C'_I = 1$ until the macula densa, $z' = 1$.

The flow and NaCl concentration inlet boundary conditions are given by $Q'(t', 0) = Q'_{in}$ and $C'(t', 0) = C'_{in}$, respectively.

6.2.2 Results

Figure 6.6 shows the luminal, variable interstitial, and fixed interstitial NaCl profiles. The fixed interstitial profile was used in Chapters 3 and 4 and also by [28]. Layton et al. [45] also used a fixed interstitial NaCl concentration profile that had a similar shape, although they used exponential rather than linear functions. The variable interstitial profile shows some similarity to the fixed profile. They both increase in the descending limb and decrease in the ascending limb. The variable interstitial profile is not continuous like the fixed interstitial profile as there is no spatial continuity enforced by (6.2). The shape of the interstitial NaCl concentration profile arises purely as a result of the countercurrent mechanism, not a prior assumption as in previous work. The discontinuities occur at $z' = z'_d$ and $z' = z'_a$. The maximum value of the luminal NaCl concentration is limited by the maximum value of the interstitial NaCl concentration. Therefore, as the maximum of the interstitial concentration is lower with the variable interstitial profile the luminal NaCl concentration is also lower. Despite this difference the NaCl concentration at the macula densa is similar with a variable or fixed interstitial NaCl concentration profile. For the steady state profile with a fixed interstitial concentration profile see Figure 3.2.

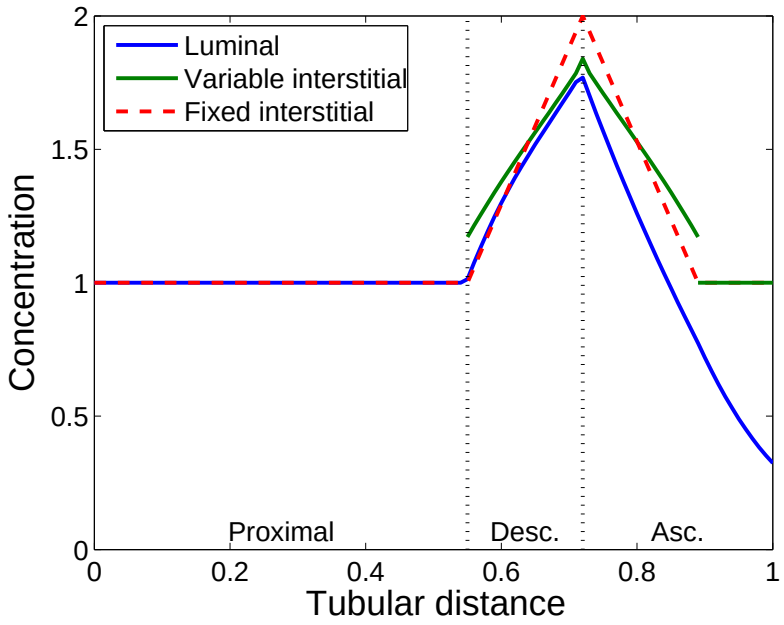

Figure 6.6 Luminal, variable interstitial, and fixed interstitial NaCl concentration profiles (v'=1).

The interstitial NaCl concentration increases with increasing depth. This agrees with the profile expected from the operation of the countercurrent mechanism. The results of the model also show how the countercurrent mechanism creates and maintains the NaCl concentration gradient in the interstitium. The steady state results support the shape of the fixed NaCl concentration profile used in Chapter 3.

Several values of the strength of the vasa recta convection, v', were used to determine its effect on the system. As expected, increasing v' resulted in a lower peak in the luminal and interstitial concentration profiles as NaCl was more rapidly removed from the system. Lowering v' had the opposite effect, resulting in relatively higher NaCl concentrations in both the luminal and interstitial profiles. The steady state profiles for four values of v' are shown in Figure 6.7. Interestingly, the value of v' had a relatively small effect on the value of the NaCl concentration at the macula densa despite having a large effect on the maximum of the luminal and interstitial NaCl concentration.

Figure 6.8 shows the effect of a small flow perturbation. The system is initially started in the steady state, then it is subjected to an inlet flow increase from $Q'(t', 0) = 1$ to $Q'(t', 0) = 1.1$ at $t = 5$. This tubular inlet flow perturbation has a similar effect to the step increase in afferent arteriolar inlet pressure used in

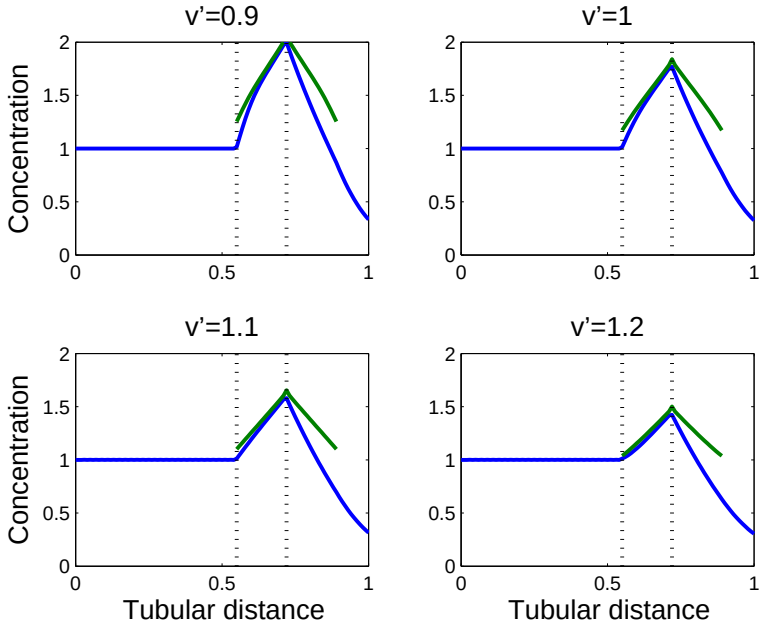

Figure 6.7 Steady state NaCl profiles for four values of the vasa recta convection strength, v'.

Chapters 3 and 4.

As expected, the NaCl concentrations return to a stable equilibrium after exhibiting a small period of transient behaviour. There are no damped oscillations as this is only a model of the tubule with no TGF present. The NaCl concentration monotonically converges to the new steady state. The NaCl concentration at the macula densa comes to equilibrium at a higher value that with an intact TGF mechanism; as the TGF mechanism acts to maintain a constant flow via homeostasis of the macula densa NaCl concentration. The maximum of the interstitial NaCl concentration varies very little with this increase in flow.

6.2.3 Discussion

The model presented in this section differs from the model presented in Chapter 3. The TGF and glomerular models were removed and a variable interstitial NaCl concentration profile was added. Replacing the fixed interstitial NaCl concentration profile of Chapter 3 with the variable interstitial NaCl concentration profile from this chapter is expected to change the time dynamics of the model. However, it is not clear what effect it will have on the generation of sustained oscillations. It could reduced the likelihood of sustained oscillations by damping

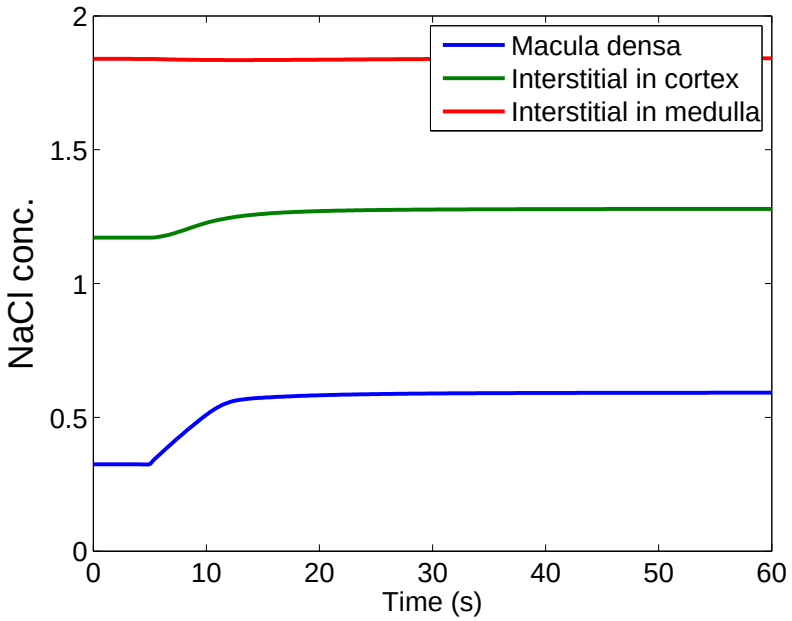

Figure 6.8 Transient behaviour in response to a small change in inlet flow rate from $Q_{\text{in}} = 1$ to $Q_{\text{in}} = 1.1$ at t=5 (v=1). This figure shows the luminal concentration at the macula densa, $C'(t', 1)$, and the interstitial concentrations at the cortex/medulla boundary, $C'_{\text{I}}(t', z'_{\text{p}})$ and deep in the cortex, $C'_{\text{I}}(t', z'_{\text{d}})$.

concentration changes at the macula densa in response to changes in afferent arteriole resistance. Or it could increases the concentration changes at the macula densa increasing the likelihood of sustained oscillations. Further work is required to ascertain the effect of a variable interstitial concentration profile on the generation of sustained oscillations.

The discontinuity in the variable interstitial NaCl concentration profile is physiologically unrealistic. Spatial continuity could be included by adding a convection term to (6.2). This would enforce interstitial NaCl concentration boundary conditions at $z' = z'_{\text{p}}$ and $z' = z'_{\text{a}}$.

In summary, this section presents a variation on the single nephron model presented in Chapter 3. The interstitial NaCl concentration is modelled using a PDE instead of a fixed interstitial NaCl concentration profile. The results support the profiles expected from the countercurrent mechanism. The interstitial NaCl concentration profile is similar to the fixed NaCl concentration profile used in Chapters 3 and 4 and by [28] and [45] and arises from the physiology. This supports the assumption of a linear profile used in this thesis and by others [28, 45]. This model produces a discontinuous interstitial NaCl profile that is unrealistic.

Chapter 7

INTER-NEPHRON COUPLING

Nephrons affect one another through their shared vasculature [73]. The models presented in the previous chapters of this thesis do not incorporate the effects from neighbouring nephrons that occur *in vivo*. Many afferent arterioles branch off a single interlobular artery and are defined as coupled in the literature if they share the same interlobular artery. This shared, anatomically close piece of the vasculature allows for at least two types of coupling: vascular and haemodynamic [30].

Vascular coupling occurs as electrochemical signals from the TGF mechanism of one nephron are transmitted from its afferent arteriole through the interlobular artery to the afferent arteriole of neighbouring nephrons. This type of coupling tends to produce in-phase oscillations as the signal to the neighbouring nephron propagates rapidly compared to the time scale of the oscillations [30]. Although this interaction is supported by a wide range of experimental evidence, the details of this mechanism are not currently known [56]. It is believed that electrochemical signals propagate upstream along the arteriole wall from the afferent arteriole. There is experimental evidence that the tubuloglomerular feedback (TGF) mechanism not only varies the resistance of the afferent arteriole but also affects the resistance of the interlobular arteries, the next highest level of the vasculature [33, 70]. This resistance change also travels downstream to afferent arterioles that feed from the same interlobular artery.

Haemodynamic coupling occurs as one nephron varies its resistance in turn initiating a change in pressure across the neighbouring nephrons [61]. For example nephron A increases its resistance, this increases flow to the coupled nephron B, approximately half a period later nephron B constricts, increasing flow to nephron A. As can be seen from this example, haemodynamic coupling tends to produce out-of-phase or antiphase oscillations. In an experiment from Marsh et al. [56],

the vascular coupling overwhelmed the haemodynamic coupling. However, the relative strengths of the two forms of coupling depends on the anatomy [67].

Most of the experimental literature on coupled nephrons shows synchronised oscillations [24, 33, 73]. Although antiphase oscillations, 180° phase difference, have also been observed [67]. In the nephrons exhibiting antiphase oscillations the afferent arterioles were too far apart for the vascular coupling component to be active [67], and hence the haemodynamic coupling dominated. The anatomy of the vascular network dictates if vascular or haemodynamic coupling is stronger and synchronous or antiphase oscillations are observed [30]. Yip et al. [73] found that, when nephrons were entrained, there was consistently a small phase lag between the members of each pair. The phase difference arises from the difference in natural frequencies; the faster oscillator leads the synchronised oscillations while the slower oscillator lags behind [73]. In contrast to coupled nephrons, those without a common afferent arteriolar origin, referred to as uncoupled nephrons, typically did not have the same phase or frequency [33]. This experimental evidence implies that sub-populations of nephrons are synchronised but that the entire population is not. Uncoupled nephrons that were adjacent showed no signs of entrainment and were not affected by altering the oscillations in the adjacent nephron [73]. This evidence implies that the nephrons are coupled through their vasculature and not through the interstitial space.

Coupled oscillators arise in a wide range of biological systems ranging from population to cellular level. These systems of coupled oscillators can exhibit a wide range of behaviours including: synchronous oscillations, same frequency and phase; asynchronous oscillations, same frequency and different phase; or phase drift, different frequency [21]. Entrainment is a well-known characteristic of weakly coupled oscillators, where two systems that oscillate independently at different frequencies oscillate at the same frequency when they are coupled [24, 33, 73].

Experimental results have shown that oscillations in one nephron can be affected by altering the oscillations in a coupled nephron [24, 33, 49, 73]. The oscillations were altered by increasing the flow with microperfusion of artificial tubular fluid or by blocking the TGF response with furosemide. Reducing the amplitude of oscillations in a coupled nephron reduced the amplitude of the oscillations in the other nephron as shown in Figure 2.5. In an uncoupled pair, reducing the amplitude of the oscillations in one nephron had no effect on the other.

Populations of synchronised nephrons will provide a faster and stronger response than nephrons that are asynchronous [61]. These results indicate the operation of an interaction amongst nephrons derived from a common cortical radial artery. Such an interaction could produce a cooperative effect larger than that predicted from measured single-nephron responses when systemic arterial pressure changes [33].

Several multi-nephron models have been published recently [67, 5, 60]. Much of the earlier work on coupling used very simple single nephron models. As computers have become more powerful models coupling up to 16 detailed single nephron models have been investigated. Vascular and haemodynamic forms of coupling has been successfully modelled. These papers showed a wealth of different behaviours including chaos, entrainment, and anti-phase oscillations depending on the type of coupling and parameters used.

This chapter investigates the effect of vascular coupling in the single nephron model with the ordinary differential equation (ODE) tubular model presented in Chapter 4. The simple ODE representation permits analytical stability analysis through interrogation of the Jacobian matrix of the system. This is not possible with the partial differential equation (PDE) tubular model presented in Chapter 3. The coupled nephrons exhibit entrainment, where the natural frequencies of two nephrons become the same as the level of coupling is increased.

7.1 MODEL

Coupling two nonlinear, oscillatory models can lead to a wealth of behaviours including synchronisation, constant phase lags, phase drift, and chaos [21]. The effects of coupling were explored by coupling two single nephron models from Chapter 4. A simple, physiologically realistic coupling model was chosen to couple two nephrons together. The single nephron model developed in Chapter 4 was chosen because it permitted a high level of analytical analysis, low computational expense, and produced good results compared to both the PDE model, presented in Chapter 3, and experimental results. Only vascular coupling was included in this model. There were two reasons for this: (i) antiphase oscillations, associated with strong haemodynamic coupling, are rarely seen in the literature and (ii) to elucidate the implications of this type of coupling without the confounding factors of haemodynamic coupling.

This coupling model assumes instantaneous signal transmission. This is a

good first approximation as the signal travels quickly compared to the period of the oscillations [67]. The single nephron models were based on the exponential approximation for the ascending limb sodium chloride (NaCl) concentration, as outlined in Chapter 4. The linear approximation gave qualitatively similar results albeit in slightly different areas of parameter space. The exponential approximation was preferred to the linear approximation as it did not produce physically incorrect negative concentrations at low mean arterial pressures. The resistances of the afferent arterioles, $\mathbf{R} = (R_{\mathrm{aA}},\ R_{\mathrm{aB}})^{\mathrm{T}}$, were again assumed to be a governed by a first-order response, given by

$$\dot{\mathbf{R}} = t_0'(\mathbf{R}^* - \mathbf{R}). \tag{7.1}$$

The target resistance, $\mathbf{R}^*$, is given by a weighted average of the signals from each macula densa,

$$\mathbf{R}^* = \begin{bmatrix} (1-\alpha) & \alpha \\ \alpha & (1-\alpha) \end{bmatrix} \boldsymbol{\phi},\ \alpha \in [0,\ 1], \tag{7.2}$$

where

$$\boldsymbol{\phi}_{\mathrm{i}} = \xi'_{\max} - \frac{\psi'}{1 + \exp(k'(\mathbf{C}_{(\mathrm{md})\mathrm{i}} - C_{1/2}))},\ i = 1, 2. \tag{7.3}$$

α denotes the level of coupling and $\mathbf{C}_{(\mathrm{md})} = (C_{(\mathrm{md})\mathrm{A}},\ C_{(\mathrm{md})\mathrm{B}})^{\mathrm{T}}$ is a vector of the concentrations at the macula densa of each coupled nephron. This equation was also used in Chapters 3 and 4 to relate the concentration at the macula densa to the target resistance of the afferent arteriole. For a coupling value of $\alpha = 0$, the information only comes from the nephron's own macula densa. This corresponds to two uncoupled nephrons. For $\alpha = 1$, the information comes solely from the coupled nephron's macula densa.

Relatively few experimental measurements of the coupling parameter have been taken [60]. Kallskog and Marsh [33] experimentally observed the level of coupling between two nephrons to decay exponentially with distance. This result was used by [11] who experimentally estimated the level of coupling by fitting an exponential decay function of distance. Chen et al. [11] estimated a maximum value of the coupling parameter to be 0.3 at 0 mm separation, decaying to approximately 0.1 at 1 mm separation. This experimental procedure indicates a physiologically realistic value of the coupling parameter to fall between 0 and 0.3. A mathematical model by Pitman et al. [60] assumes a value between 0.01

and 0.3 and uses a base case of 0.1. Another mathematical model from Holstein-Rathlou et al. [30] uses a base case of 0.1 and a maximum of 0.2. A range of 0 to 0.5 has been used for much of this chapter, although the lower end of this range is probably more physiologically realistic.

7.2 RESULTS

The results of this chapter generally compared well with experimental measurements. Entrainment behaviour occurred in two individually oscillatory nephrons with the faster of the two leading the other in phase. Blocking the TGF mechanism in a pair of oscillatory nephrons stopped the oscillation in the blocked nephron and greatly reduced the amplitude of the oscillation in the coupled pair in agreement with experimental results [24].

7.2.1 Steady state

Figure 7.1 shows the effect of varying the level of coupling, α, on the steady state, macula densa concentrations of two heterogeneous nephrons. Heterogeneity is introduced through different compliance values, although heterogeneity could be introduced by varying other parameters such as the gain, k', or ascending limb pump strength, V_{max}. In the case where the nephrons are identical, the steady states are the same as in the single nephron case due to the form of the coupling being used, (7.2). For physiologically realistic values of the coupling parameter, $\alpha \in [0,\ 0.5)$, the resistance of the afferent arteriole is weighted toward the signal from the macula densa of the same nephron. For higher values of the coupling parameter, $\alpha \in [0.5,\ 1]$, the resistance of each afferent arteriole is weighted more heavily on information from the other nephron. This is not physiologically realistic and the focus of this chapter will be on values of $\alpha < 0.5$. For such values of α the steady state macula densa concentrations are close to the mean. The concentrations in each nephron diverge from the mean as α is increased. This can be seen through a simple dynamic example. A higher NaCl concentration in nephron A constricts the afferent arteriole of nephron B, lowering its volume flow and hence NaCl concentration. This low NaCl concentration in nephron B dilates the afferent arteriole of nephron A, increasing its volume flow and hence NaCl concentration. This continues until equilibrium is reached.

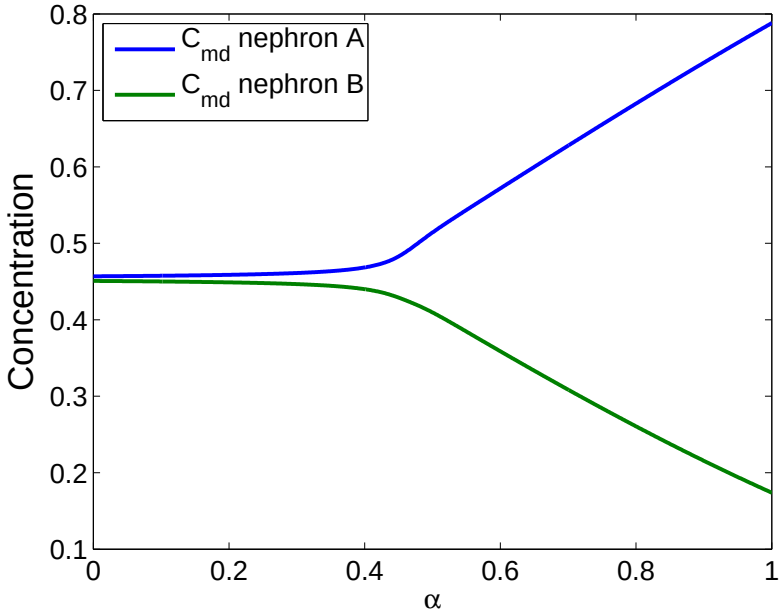

Figure 7.1 Steady state of C_{md} in each nephron as the level of coupling is varied ($\gamma'_{\mathrm{A}} = 4$, $\gamma'_{\mathrm{B}} = 1$). Blue is nephron A, green is nephron B.

7.2.2 Two nonoscillatory nephrons

Two individually nonoscillatory nephrons were coupled to produce the results shown in Figure 7.2. As expected, coupling did not incite oscillatory behaviour in either nephron. The system was started in the steady state at $t = 0$ and subjected to a single arterial pressure step of 5 mmHg at $t = 5$ s. Figure 7.2 shows three values of the coupling parameter, α. $\alpha = 0$ corresponds to no coupling and $\alpha = 0.5$ corresponds to getting 50% of the signal from each nephron. As shown in Figure 7.1, the difference between the two concentrations increases with increasing coupling. For each value of the coupling parameter the system exhibits damped oscillations around the new steady state. The uncoupled pair, $\alpha = 0$, exhibited damped oscillations at their individual natural frequencies.

7.2.3 One oscillatory nephron

The region of parameter space where an oscillatory nephron incited oscillations in a nonoscillatory coupled nephron was very small. It is unlikely that this region of parameter space is encountered *in vivo*. This is shown in Figure 7.10 and discussed in more detail later in this chapter. In the majority of cases coupling one oscillatory nephron with a nonoscillatory nephron produced nonoscillatory

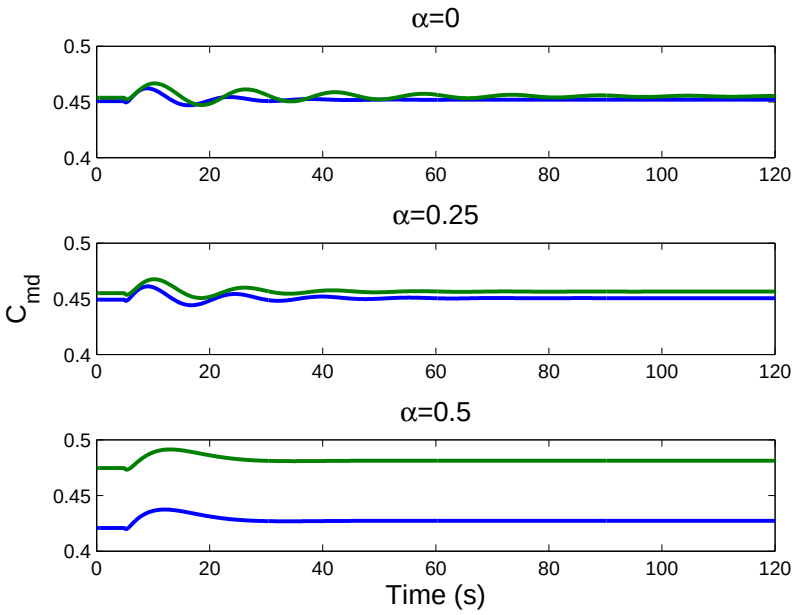

Figure 7.2 Two nephrons exhibiting nonoscillatory behaviour for three levels of coupling ($\gamma'_{\mathrm{A}} = 0.2$ and $\gamma'_{\mathrm{B}} = 0.4$). Blue is nephron A, green is nephron B.

behaviour in both nephrons.

7.2.4 Two oscillatory nephrons

Figure 7.3 shows the effect of varying the level of coupling between two individually oscillatory nephrons. With no coupling the two nephrons oscillate at their natural frequencies. As the level of coupling is increased the nephrons become synchronised. The system exhibits entrainment as the frequency of the faster oscillations reduces and the frequency of the slower oscillations increases. The system exhibits synchronisation even if each nephron is initialised with a different phase as shown in Figure 7.7.

Figure 7.4 shows how the frequency of the oscillations changes with coupling. Each subplot corresponds to the respective time series in Figure 7.3. The model simulated 6400 s of time series data; the first 800 s was discarded to remove transient behaviour. Without coupling ($\alpha = 0$), the two nephrons oscillated at their two distinct natural frequencies. As the coupling parameter is increased they became entrained, oscillating at the same frequency. The entrained frequency was located between the distinct natural uncoupled frequencies, as expected. Although, it was typically a higher frequency than the average. The amplitude

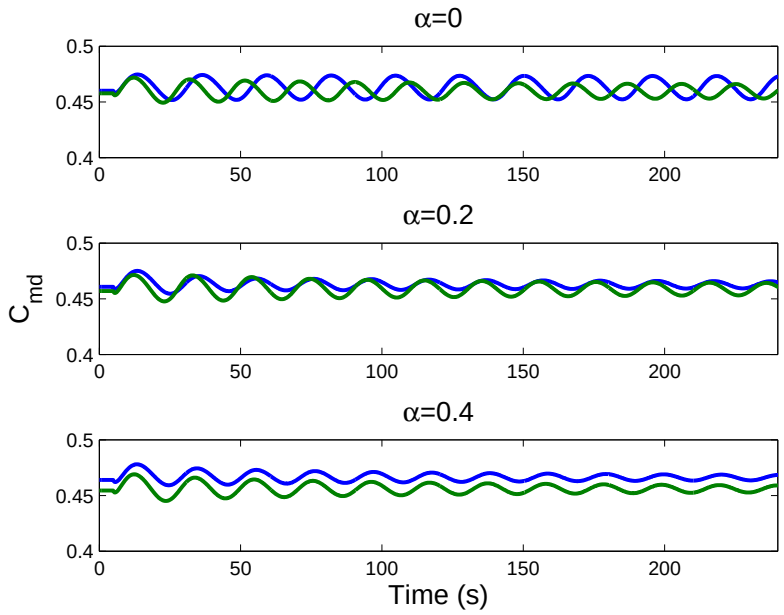

Figure 7.3 Two individually oscillatory nephrons (γ'_{A}=0.8, γ'_{B}=1.2, k'=120, and $C'_{1/2}$=68). Blue is nephron A, green is nephron B.

decreased with increased coupling.

Figure 7.5 shows frequencies and amplitudes of a pair of uncoupled nephrons as the compliance of nephron B is varied. As expected, the frequency and amplitude of nephron A is constant as it is unaffected by the compliance of nephron B. The frequency and amplitude of nephron B vary as they did in the single nephron case, shown in Figure 4.12. At $\gamma'_{\mathrm{B}} = 1.2$ the nephrons are identical and their frequencies and amplitudes are also identical.

Figure 7.6 shows the frequencies and amplitudes of a pair of coupled nephrons. In contrast to the results shown in Figure 7.5, varying the compliance of nephron B in a coupled pair affects both the amplitude and frequency of the oscillations of nephron A. The individually oscillatory nephron A becomes damped when coupled with nephron B, when it has a low value of compliance.

7.2.5 Phase locking

Figure 7.7 shows the transience to entrainment between two coupled nephrons. The initial conditions were constructed by first finding the steady state at 5 mmHg either side of mean arterial pressure. Nephron A was started at the high pressure steady state and Nephron B was started at the low pressure steady state. This

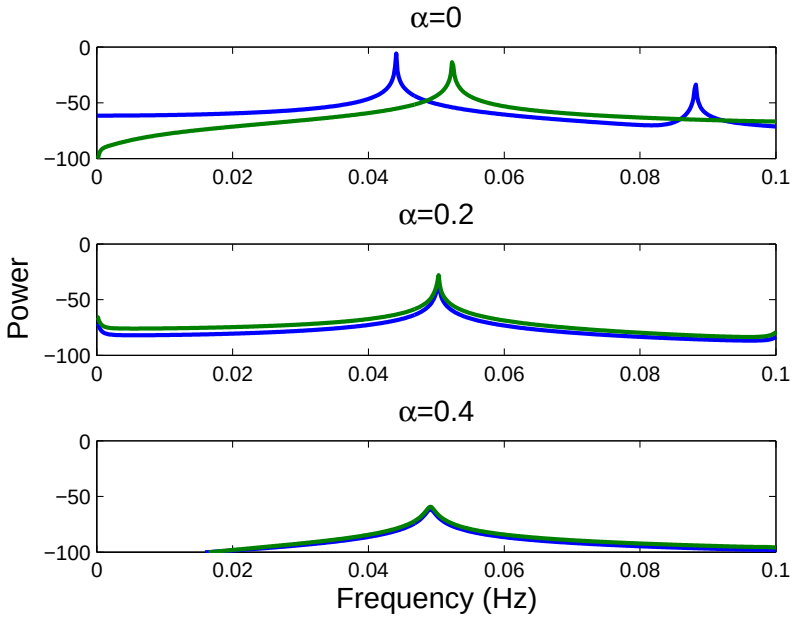

Figure 7.4 Fourier transforms of the time series from Figure 7.3 (γ'_{A}=0.8, γ'_{B}=1.2, $C'_{1/2}$=68, and k'=120). With no coupling, α=0, the nephron oscillate at their natural frequencies. As the coupling is increased the nephrons become entrained. Blue is nephron A, green is nephron B.

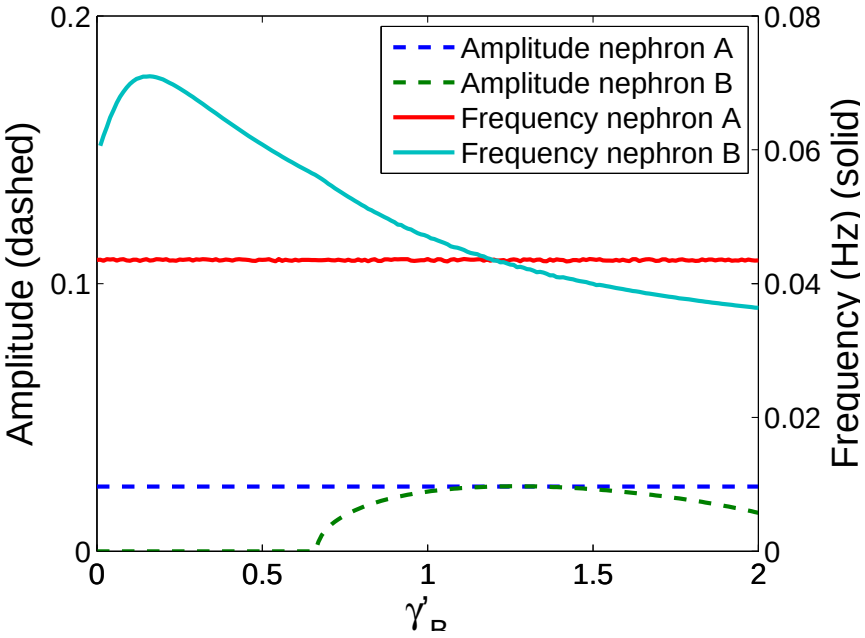

Figure 7.5 The effect of varying the compliance of one nephron in an **uncoupled** pair ($\alpha = 0$, γ'_{A}=1.2, $C'_{1/2}$=68, and k'=120). At γ_{B}=1.2, the nephrons are identical and the nephron A and nephron B curves coincide.

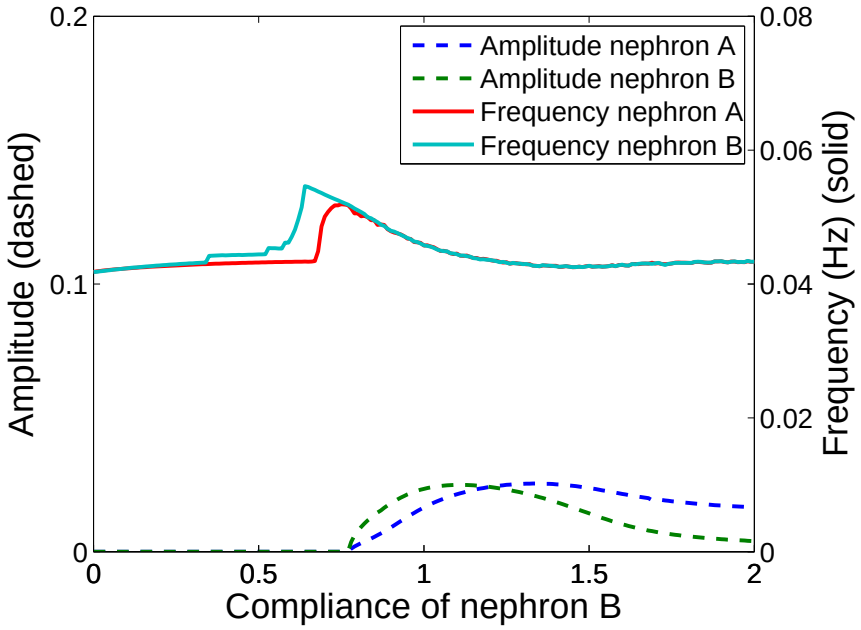

Figure 7.6 The effect of varying the compliance of one nephron in a **coupled** pair ($\alpha = 0.2$, γ'_{A}=1.2, $C'_{1/2}$=68, and k'=120).

initial condition ensures the nephrons start in two very different states. The two nephrons become entrained over approximately 100 s regressing into stable limit cycle behaviour. This shows that the two nephrons become entrained even though they are initialised in two very different states.

Figure 7.8 shows phase plots of the time series from Figure 7.3. The first subplot show two uncoupled, individually oscillatory nephrons. As the two nephrons are oscillating at different frequencies they exhibit phase drift. This results in no correlation between the two concentrations. As the coupling parameter is increased they exhibit entrainment and stable limit cycle behaviour. With further increase in the coupling parameter the amplitude of the limit cycle begins to decrease. For unrealistically high values of the coupling parameter, $\alpha > 0.6$, the concentrations are forced away from the mean in a similar fashion to the steady state results shown in Figure 7.1. In this physiologically unrealistic case the steady state of the system is stable. It is important to note that the limit cycle does not lie on the line $C_{(\mathrm{md})\mathrm{B}} = C_{(\mathrm{md})\mathrm{A}}$. This result implies that there is always a phase lag. The faster oscillator always leads the slower oscillator. This result is consistent with experimental result from Yip et al. [73], who found a small phase lag of $20.3 \pm 2.6^{\circ}$. The compares reasonably with the model results. For example the phase lag for the time series presented in Figure 7.7 is approximately 35°.

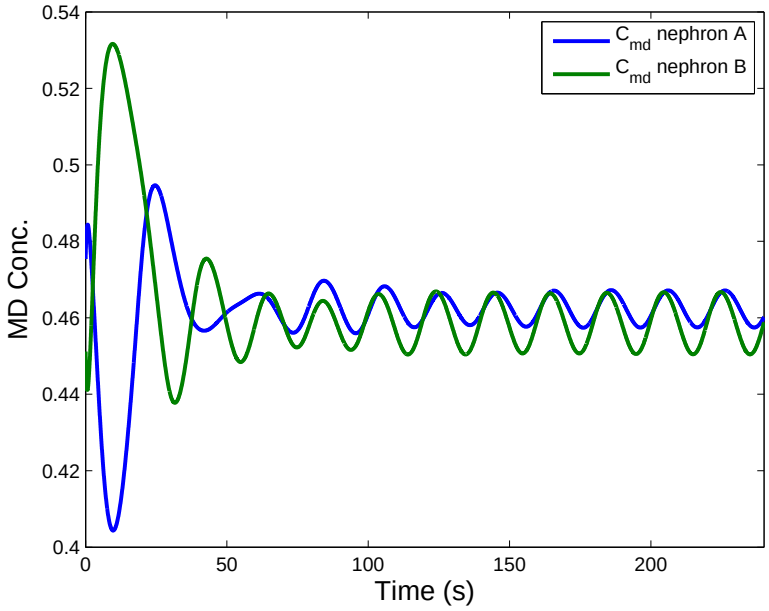

Figure 7.7 Transient behaviour as the two coupled, individually oscillatory nephrons become entrained ($\alpha = 0.2$, $\gamma_{\mathrm{A}} = 1.2$, and γ_{B}=0.8).

This value varies with the level of coupling and the uncoupled frequencies of each nephron.

7.2.6 Bifurcation diagrams

Figure 7.9 shows the stability of the steady state as the compliances of two uncoupled nephrons are varied. As these two nephrons are uncoupled each behaves as it would individually. To the right of the line $\gamma'_{\mathrm{A}} \approx 0.6$ nephron A is oscillatory and above the line $\gamma'_{\mathrm{B}} \approx 0.6$ nephron B is oscillatory.

Figure 7.10 shows the effect of varying the coupling parameter on the stability of the steady state in a pair of coupled nephrons. The dashed lines indicate a change in stability of the steady state in a pair of uncoupled nephrons, $\alpha = 0$, as shown in Figure 7.9. The solid lines indicate a change a change in stability for a range of different values of the coupling parameter. The main effect of increased coupling is to reduce the region of parameter space where sustained oscillations occur. For example, for $(\gamma'_{\mathrm{A}}, \gamma'_{\mathrm{B}}) = (1.8, 0.8)$ the system is oscillatory if the nephrons are uncoupled, $\alpha = 0$, or 10% coupled, $\alpha = 0.1$. For higher values of the coupling parameter the steady state is stable. The uncoupled frequencies of these two nephrons are quite different as shown in Figure 7.5. As the coupling as

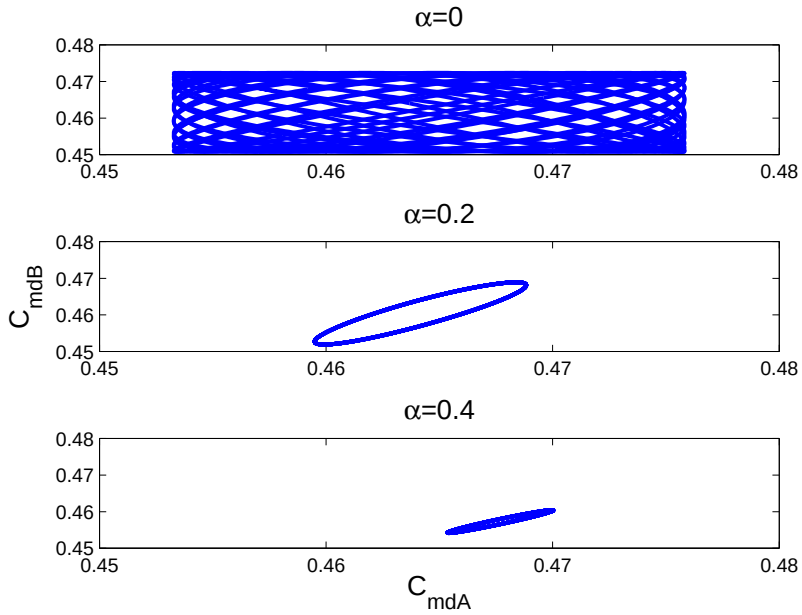

Figure 7.8 A: phase drift of two uncoupled oscillators, B,C: synchronous behaviour as the coupling parameter is increased (k'=0.8, $C'_{1/2}$=68, γ'_{A}=1, γ'_{B}=1.5).

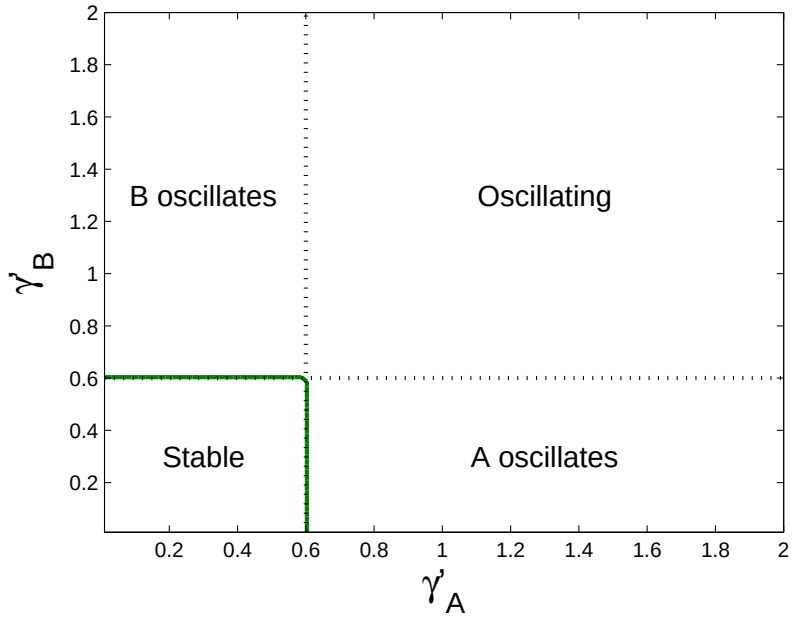

Figure 7.9 Regions of stability of the steady state as the compliances of two **uncoupled** nephrons are varied (α=0).

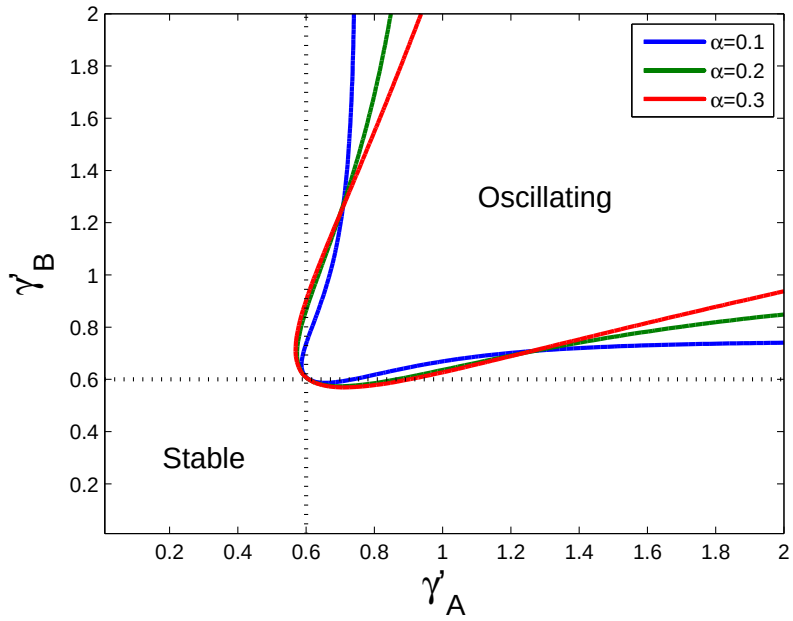

Figure 7.10 Stability of the steady state as the compliances of two **coupled** nephrons are varied for a range of the coupling parameter, α.

increased these two differing frequencies tend to reduce the oscillatory behaviour of one another. Thus, oscillatory behaviour remains around the line $\gamma'_{\mathrm{A}} = \gamma'_{\mathrm{B}}$ due to their similar uncoupled frequencies as α is increased.

There are two small regions where an uncoupled oscillatory nephron induces an oscillation in an uncoupled nonoscillatory nephron. These regions can be identified in Figure 7.10 to the left of the line $\gamma'_{\mathrm{A}} = 0.6$ or below the line $\gamma'_{\mathrm{b}} = 0.6$.

7.2.7 Experimental intervention

Figure 7.11 shows the effect of disabling the TGF mechanism in one nephron on a coupled pair. The TGF mechanism was disabled in nephron B by setting $C_{(\mathrm{md})\mathrm{B}} = C_{1/2}$. As the TGF mechanism is disabled in nephron B the NaCl concentration at the macula densa monotonically tends to its steady state. Nephron A is now getting its 70% of its signal from its own glomerulus and 30% from the now constant coupled nephron. The constant part of this signal reduces the amplitude of the oscillation in the NaCl concentration at the macula densa of Nephron A. This models the effect of disabling the TGF mechanism in one of a pair of coupled nephron by administering a loop diuretic like Furosemide. The reduction in the amplitude of the oscillation in one nephron exhibited by the model shows good

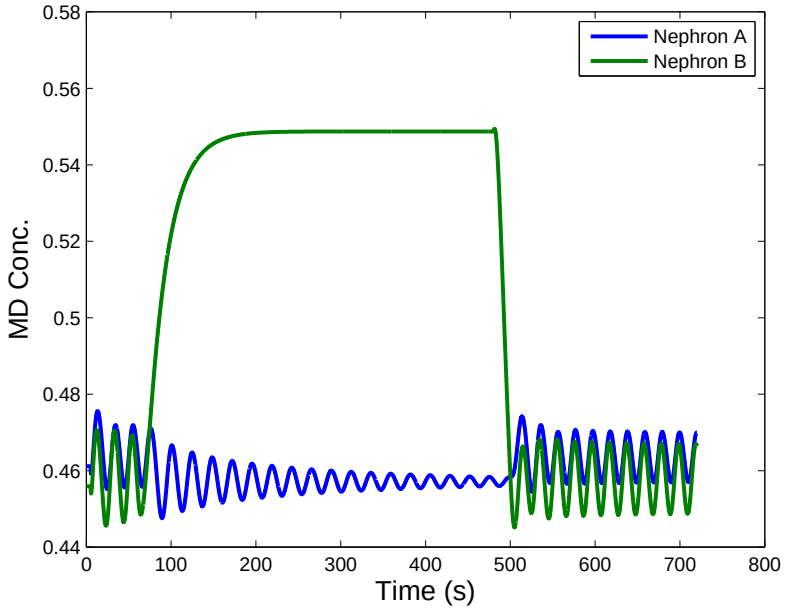

Figure 7.11 The effect of disabling the TGF mechanism in one nephron of a coupled pair (α=0.3, γ'_{A}=0.8, γ'_{B}=1.2). The TGF mechanism of nephron B was turned off between $t = 60$ and $t = 480$ by setting $C_{(\mathrm{md})\mathrm{B}} = C_{1/2}$ in equation (7.3).

qualitative agreement with experimentally disabling the TGF mechanism shown in Figure 2.5.

7.3 DISCUSSION

Two single nephron models with PDE tubular models could be coupled in the same way. It is expected that they would return similar results due to the good comparison of the ODE and PDE tubular models. The range of parameter space that exhibited oscillatory and nonoscillatory behaviour would not be the same. For example oscillatory behaviour occurred for a lower value of compliance with the PDE tubular model. However the same qualitative shift from nonoscillatory to oscillatory behaviour is expected. Using the ODE tubular model allowed a 3D bifurcation diagram, like Figure 7.10, to be calculated relatively inexpensively through the Jacobian matrix of the system. This was computationally prohibitive with the PDE tubule model.

Haemodynamic coupling could be added to the model by modelling a small section of the interlobular artery by Poiseuille's law. This would allow for pressure and flow changes in one nephron to be realistically transmitted to the coupled

nephron through this shared piece of the vasculature. This resistance of this piece of interlobular artery could also be dependent on the signal from each macula densa as observed experimentally [70]. Higher levels of the vascular tree could be modelling using a similar approach to that of Kleinstreuer et al. [37]. It is hypothesised that this increased coupling will tend to increase the level of synchronisation.

In summary, this chapter coupled two single nephron models with ODE tubular models as developed in Chapter 4. The signal to the afferent arteriole was taken to be a weighted average of the NaCl concentration at its own macula densa and the macula densa of the coupled pair. Entrainment behaviour occurred in two individually oscillatory nephrons. An individually oscillatory nephron did not usually incite an oscillation in a individually nonoscillatory nephron. Blocking the TGF mechanism in a pair of oscillatory nephrons stopped the oscillation in the blocked nephron and greatly reduced the amplitude of the oscillation in the coupled pair in agreement with experimental results [24].

Chapter 8

SUMMARY AND DISCUSSION

This thesis presents a number of single nephron tubuloglomerular feedback (TGF) models based primarily on the model of Holstein-Rathlou and Marsh [28]. The main focus of this thesis was to determine the factors that contribute to sustained oscillatory behaviour that has been observed experimentally. The physiological significance of sustained oscillations is not clear and has not been addressed in the literature. A better understanding of the factors that contribute to sustained oscillations will aid in the understanding of their physiological significance.

Chapter 3 initially derives the single TGF model used by Holstein-Rathlou and Marsh [28] then presents and discusses several changes to the [28] model. The crucial change is the replacement of their second-order ordinary differential equation (ODE) with a first-order ODE, which models the resistance of the afferent arteriole. In contrast to the second-order ODE the first-order ODE is not inherently oscillatory. Sustained oscillations were exhibited by the model with a first-order differential equation model for the resistance of the afferent arteriole and they had a period of 15–20 s. With a noncompliant tubule, sustained oscillations were not exhibited for any parameter set tested and are unlikely to be encountered *in vivo*.

Chapter 4 presents a ODE approximation to the PDE model presented in Chapter 3. The ODE model has several advantages to the PDE model: it is less computationally intensive to solve, a higher degree of analytical analysis is feasible, and it is conceptually simpler while still producing similar results to the PDE model. The ODE tubular model exhibits sustained oscillations for similar areas of parameter space to the PDE tubular model. Compliance was again found to be important for sustained oscillations.

Chapter 5 presents the results of applying an inlet pressure forcing to the single nephron model presented in Chapter 3. Two forcings were applied: a pe-

riodic forcing and a mean-reverting white noise process. The white noise process models the wide range of frequencies observed experimentally to occur *in vivo*. The single nephron model with a noncompliant tubule model was not inherently oscillatory as shown in Chapters 3 and 4. Sustained oscillations were exhibited if the noncompliant system was forced with either a periodic or mean-reverting stochastic pressure perturbation.

Chapter 6 presents two extensions to the single nephron models presented in Chapters 3 and 4: a small delay and a variable interstitial concentration profile. A small delay models the delay observed experimentally between a change in sodium chloride concentration at the macula densa and a change in the vascular tone of the afferent arteriole. Adding a small delay changed the behaviour of the nonoscillatory single nephron model with a noncompliant tubule form nonoscillatory to oscillatory. The delay was physiologically motivated and was small compared to the period of the oscillations. The second extension was to remove the fixed interstitial profile and replace it with a variable interstitial NaCl concentration. The results support the profiles expected from the countercurrent mechanism. The interstitial NaCl concentration profile is similar to the fixed NaCl concentration profile used in Chapters 3 and 4 and by [28] and [45].

Damped oscillations with a frequency consistent with the action of the TGF mechanism were exhibited in the noncompliant, fixed pressure, undelayed model for a wide range of parameter space. Adding tubular compliance, a physiologically realistic pressure perturbation, or a delay across the juxtaglomerular apparatus changed the behaviour of the system from damped oscillations to sustained oscillations. It is unclear which factors or combination of factors is responsible for eliciting sustained oscillations *in vivo* without experimental validation. The pressure forcing hypothesis would be the easiest to test experimentally and could be done by holding the inlet pressure constant with conventional experimental methods. The compliance and delay hypotheses would be harder to test experimentally and would probably require chemical manipulation.

Chapter 7 presents the effects of coupling two single nephron models with ODE tubular models as developed in Chapter 4. The signal to the afferent arteriole was taken to be a weighted average of the NaCl concentration at its own macula densa and the macula densa of the coupled pair. Entrainment behaviour occurred in two individually oscillatory nephrons as observed experimentally. Blocking the TGF mechanism in a pair of oscillatory nephrons stopped the oscillation in the blocked nephron and greatly reduced the amplitude of the

oscillation in the coupled pair also in agreement with experimental results [24].

This thesis provides background on experimental and modelling results relating to the TGF mechanism, sustained oscillation, and coupling. The modelling work in this thesis names a few possible causes of sustained oscillations and briefly suggests experimental methods to test them. Additional modelling work could also be undertaken on the variable interstitial NaCl profile and coupling. The variable interstitial NaCl profile was not attached to a working TGF model. This could be relatively easily added using the work in this thesis. It would be interesting to see the effect of a variable interstitial NaCl profile on the transient behaviour of the system. Only vascular coupling was implemented in the thesis. The effect of hemodynamic coupling has been shown to be significant in certain cases and adding this would enable modelling of these cases.

Appendix A

ORNSTEIN-UHLENBECK PROCESS

The Ornstein-Uhlenbeck process is the solution, X_{t}, of the stochastic differential equation

$$\mathrm{d}X_{\mathrm{t}} = \theta\left(m - X_{\mathrm{t}}\right)\mathrm{d}t + \sigma \mathrm{d}B_{\mathrm{t}} \tag{A.1}$$

where m, and σ are real constants, $B_{\mathrm{t}} \in \mathbb{R}$. The solution to this stochastic differential equation can be found using Ito's formula,

$$X_{\mathrm{t}} = m + \left(X_0 - m\right)e^{-\theta t} + \sigma \int_0^t e^{\theta(s-t)}\mathrm{d}B_{\mathrm{s}}. \tag{A.2}$$

The expected value of X_{t} is

$$\mathrm{E}[X_{\mathrm{t}}] = X_0 e^{-\theta t} + m\left(1 - e^{-2\theta t}\right), \tag{A.3}$$

and the variance of X_{t} is

$$\mathrm{var}[X_{\mathrm{t}}] = \frac{\sigma^2}{2\theta}\left(1 - e^{-2\theta t}\right), \tag{A.4}$$

where the long term variance, $\mathrm{Var}_{\mathrm{LT}}$, is given by

$$\mathrm{Var}_{\mathrm{LT}} \equiv \lim_{t\to\infty} \mathrm{var}[X_{\mathrm{t}}] = \frac{\sigma^2}{2\theta}. \tag{A.5}$$

The numerical Euler-Maruyama method can be used to solve (A.1) [22]. The numerical approximation, X_{i}, to the exact solution, X_{t} is given by

$$X_{\mathrm{i}+1} = X_{\mathrm{i}} + \theta\left(m - X_{\mathrm{i}}\right)h + \sigma\sqrt{h}N(0,1) \text{ for } i = 0, ..., N \tag{A.6}$$

where h is the time step size and given the initial condition X_0. If $\sigma = 0$, the equation reverts to Euler's method.

θ and σ are calculated from the variance of 6.25 mmHg^2 that is used by Holstein-Rathlou et al. [29] to force their previous model [28]. Rearranging (A.5) for σ gives

$$\sigma = \sqrt{2\theta \text{Var}_{\text{LT}}}, \tag{A.7}$$

where $\text{Var}_{\text{LT}} = 6.25$ mmHg^2 is the long term variance of the process. θ is calculated from the fact that $r \equiv \left(1 - e^{-2\theta t}\right) \approx 1$ at the end of the simulation. This ensures that the variance of the simulation is approximately the long term variance. This gives

$$\theta = -\frac{1}{2t_{\text{LT}}} \ln(1 - r), \tag{A.8}$$

where t_{LT} is the long term time, typically the end of the simulation, and $r = 0.99$. These parameters are converted to nondimensional unit via $\theta' = \theta t_{\text{ref}}$ and $\sigma' = \sigma\sqrt{t_{\text{ref}}}/P_{\text{ref}}$.

Appendix B

IMPLICIT METHOD FOR CALCULATING THE JACOBIAN MATRIX

The stability of a system of ordinary differential equations can be determined by examining the eigenvalues of the Jacobian matrix of the system evaluated at the steady state. If the system is of the form $\dot{\mathbf{X}} = \mathbf{f}(\mathbf{X}(\mathbf{t}), \mathbf{t})$, the Jacobian matrix, $[J]$, can be readily calculated as

$$[J] = \left[\frac{\partial \dot{\mathbf{X}}}{\partial \mathbf{X}}\right] = \left[\frac{\partial \mathbf{f}}{\partial \mathbf{X}}\right] = \begin{bmatrix} \frac{\partial f_1}{\partial X_1} & \frac{\partial f_1}{\partial X_2} & \cdots \\ \frac{\partial f_2}{\partial X_1} & \frac{\partial f_2}{\partial X_2} & \cdots \\ \vdots & \vdots & \ddots \end{bmatrix}, \tag{B.1}$$

where $\mathbf{X}(\mathbf{t})$ is the state vector of the system, $\dot{\mathbf{X}}(\mathbf{t})$ is the first time derivative of the state vector, and square brackets denote a matrix.

If the time derivatives are defined implicity through $\mathbf{F}(\dot{\mathbf{X}}(\mathbf{X}(\mathbf{t}), \mathbf{t}), \mathbf{X}(\mathbf{t}), \mathbf{t}) = \mathbf{0}$, the Jacobian matrix can be derived using the chain rule as

$$[J] = \left[\frac{\partial \dot{\mathbf{X}}}{\partial \mathbf{X}}\right] = -\left[\frac{\partial \mathbf{F}}{\partial \dot{\mathbf{X}}}\right]^{-1} \cdot \left[\frac{\partial \mathbf{F}}{\partial \mathbf{X}}\right]. \tag{B.2}$$

Now suppose that there are additional equations that contain auxiliary variables $\mathbf{U}$ defined by

$$\mathbf{G}(\mathbf{X}, \mathbf{U}) = \mathbf{0}. \tag{B.3}$$

(B.3) implicitly defines $\mathbf{U} = \mathbf{U}(\mathbf{X})$ such that (B.3) becomes

$$\mathbf{G}(\mathbf{X}, \mathbf{U}(\mathbf{X})) = \mathbf{0}. \tag{B.4}$$

The system can be written as $\mathbf{F}(\dot{\mathbf{X}}(\mathbf{X}(\mathbf{t}), \mathbf{t}), \mathbf{X}(\mathbf{t}), \mathbf{U}(\mathbf{X}), \mathbf{t}) = \mathbf{0}$ and differentiated

with respect to $\mathbf{X}$ using the chain rule giving

$$\left[\frac{\partial \mathbf{F}}{\partial \dot{\mathbf{X}}}\right] \cdot \left[\frac{\partial \dot{\mathbf{X}}}{\partial \mathbf{X}}\right] + \left[\frac{\partial \mathbf{F}}{\partial \mathbf{X}}\right] + \left[\frac{\partial \mathbf{F}}{\partial \mathbf{U}}\right] \cdot \left[\frac{\partial \mathbf{U}}{\partial \mathbf{X}}\right] = 0 \tag{B.5}$$

that can be rearranged to give the Jacobian matrix as

$$[J] = \left[\frac{\partial \dot{\mathbf{X}}}{\partial \mathbf{X}}\right] = -\left[\frac{\partial \mathbf{F}}{\partial \dot{\mathbf{X}}}\right]^{-1} \cdot \left(\left[\frac{\partial \mathbf{F}}{\partial \mathbf{X}}\right] + \left[\frac{\partial \mathbf{F}}{\partial \mathbf{U}}\right] \cdot \left[\frac{\partial \mathbf{U}}{\partial \mathbf{X}}\right]\right). \tag{B.6}$$

(B.3) can be differentiated implicitly to give an expression for $\partial \mathbf{U}/\partial \mathbf{X}$ as

$$\left[\frac{\partial \mathbf{U}}{\partial \mathbf{X}}\right] = -\left[\frac{\partial \mathbf{G}}{\partial \mathbf{U}}\right]^{-1} \cdot \left[\frac{\partial \mathbf{G}}{\partial \mathbf{X}}\right]. \tag{B.7}$$

Substituting (B.7) into (B.6) gives an expression for the Jacobian matrix in terms of the derivatives of the implicit functions $\mathbf{F}$ and $\mathbf{G}$ with respect to $\dot{\mathbf{X}}$, $\mathbf{X}$, and $\mathbf{U}$,

$$[J] = \left[\frac{\partial \dot{\mathbf{X}}}{\partial \mathbf{X}}\right] = -\left[\frac{\partial \mathbf{F}}{\partial \dot{\mathbf{X}}}\right]^{-1} \cdot \left(\left[\frac{\partial \mathbf{F}}{\partial \mathbf{X}}\right] - \left[\frac{\partial \mathbf{F}}{\partial \mathbf{U}}\right] \cdot \left[\frac{\partial \mathbf{G}}{\partial \mathbf{U}}\right]^{-1} \cdot \left[\frac{\partial \mathbf{G}}{\partial \mathbf{X}}\right]\right). \tag{B.8}$$

REFERENCES

[1] Baines, A. D. (1978). Luminal volume and reabsorption in the loop of Henle: Effects of blood pressure and noradrenalin. *Kidney International*, 14(3):255–262.

[2] Barfred, M., Mosekilde, E., and Holstein-Rathlou, N.-H. (1996). Bifurcation analysis of nephron pressure and flow regulation. *Chaos*, 6:280–287.

[3] Barnard, A. L., Hunt, W., Timlake, W., and Varley, E. (1966). A theory of fluid flow in compliant tubes. *Biophysical Journal*, 6(6):717 – 724.

[4] Bauer, H. F. (1976). Pulsatile flow in a straight circular pipe with reabsorption across the wall. *Archive of Applied Mechanics (Ingenieur Archiv)*, 45(1):1–15.

[5] Bayram, S., Stepien, T. L., and Pitman, E. B. (2009). TGF-mediated dynamics in a system of many coupled nephrons. *Bulletin of Mathematical Biology*, 71(6):1482–1506.

[6] Brenner, B. M., Troy, J. L., and Daugharty, T. M. (1971). The dynamics of glomerular ultrafiltration in the rat. *Journal of Clinical Investigation*, 50(8):1776–1780.

[7] Brenner, B. M., Troy, J. L., Daugharty, T. M., Deen, W. M., and Robertson, C. R. (1972). Dynamics of glomerular ultrafiltration in the rat. ii. plasma-flow dependence of gfr. *American Journal of Physiology*, 223(5):1184–1190.

[8] Briggs, J. P. and Schnermann, J. B. (1996). Whys and wherefores of juxtaglomerular apparatus function. *Kidney International*, 49.

[9] Casellas, D. and Moore, L. C. (1990). Autoregulation and tubuloglomerular feedback in juxtamedullary glomerular arterioles. *American Journal of Physiology Renal Physiology*, 258(3):F660–669.

[10] Chen, Y. M. and Holstein-Rathlou, N. H. (1993). Differences in dynamic autoregulation of renal blood flow between SHR and WKY rats. *American Journal of Physiology Renal Physiology*, 264(1):F166–174.

[11] Chen, Y. M., Yip, K. P., Marsh, D. J., and Holstein-Rathlou, N. H. (1995). Magnitude of TGF-initiated nephron-nephron interactions is increased in SHR. *American Journal of Physiology Renal Physiology*, 269(2):F198–204.

[12] Chou, C. L. and Marsh, D. J. (1987). Measurement of flow rate in rat proximal tubules with a nonobstructing optical method. *American Journal of Physiology Renal Physiology*, 253(2):F366–371.

[13] Cortell, S., Gennari, F. J., Davidman, M., Bossert, W. H., Schwartz, W. B., and Ponte, M. L. (1973). A definition of proximal and distal tubular compliance: Practical and theoretical implications. *Journal of Clinical Investigation*, 52(9):2330–2339.

[14] Cupples, W. A. and Braam, B. (2007). Assessment of renal autoregulation. *American Journal of Physiology Renal Physiology*, 292(4):F1105–1123.

[15] Deen, W., Robertson, C., and Brenner, B. (1972). A model of glomerular ultrafiltration in the rat. *American Jounal of Physiology*, 223(5):1178–1183.

[16] Ditlevsen, S., Yip, K.-P., Marsh, D. J., and Holstein-Rathlou, N.-H. (2007). Parameter estimation of feedback gain in a stochastic model of renal hemodynamics: differences between spontaneously hypertensive and Sprague-Dawley rats. *American Journal of Physiology Renal Physiology*, 292(2):F607–616.

[17] Eaton, D. C. and Pooler, J. P. (2004). *Vander's Renal Physiology*. Lange Medical Books/McGraw-Hill.

[18] Gonzalez-Fernandez, J. M. and Ermentrout, B. (1994). On the origin and dynamics of the vasomotion of small arteries. *Mathematical Biosciences*, 119(2):127–167.

[19] Gopalsamy, K. (1992). *Stability and oscillations in delay differential equations of population dynamics*. Springer.

[20] Greger, R. (1981). Coupled transport of Na+ and Cl- in the thick ascending limb of Henle's loop of rabbit nephron. *Scandinavian Audiology. Supplementum*, 14 Suppl:1–15.

[21] Hastings, A. and Goldwyn, E. E. (2009). Small heterogeneity has large effects on synchronization of ecological oscillators. *Bulletin of Mathematical Biology*, 71(1):130–144.

[22] Higham, D. J. (2001). An algorithmic introduction to numerical simulation of stochastic differential equations. *SIAM Review*, 43(3):525–546.

[23] Holstein-Rathlou, N. and Leyssac, P. (1986). TGF-mediated oscillations in the proximal intratubular pressure: differences between spontaneously hypertensive rats and Wistar-Kyoto rats. *Acta Physiologica Scandinavica*, 126:333–339.

[24] Holstein-Rathlou, N. H. (1987). Synchronization of proximal intratubular pressure oscillations: evidence for interaction between nephrons. *Pflügers Archiv European Journal of Physiology*, 408(5):438–443.

[25] Holstein-Rathlou, N. H., Christensen, P., and Leyssac, P. P. (1982). Effects of halothane-nitrous oxide inhalation anesthesia and inactin on overall renal and tubular function in Sprague-Dawley and Wistar rats. *Acta Physiologica Scandinavica*, 114(2):193–201.

[26] Holstein-Rathlou, N. H. and Leyssac, P. P. (1987). Oscillations in the proximal intratubular pressure: a mathematical model. *American Journal of Physiology Renal Physiology*, 252(3):F560–572.

[27] Holstein-Rathlou, N. H. and Marsh, D. J. (1989). Oscillations of tubular pressure, flow, and distal chloride concentration in rats. *American Journal of Physiology Renal Physiology*, 256(6):F1007–1014.

[28] Holstein-Rathlou, N. H. and Marsh, D. J. (1990). A dynamic model of the tubuloglomerular feedback mechanism. *American Journal of Physiology Renal Physiology*, 258(5):F1448–1459.

[29] Holstein-Rathlou, N. H., Wagner, A. J., and Marsh, D. J. (1991). Tubuloglomerular feedback dynamics and renal blood flow autoregulation in rats. *American Journal of Physiology Renal Physiology*, 260(1):F53–68.

[30] Holstein-Rathlou, N.-H., Yip, K.-P., Sosnovtseva, O. V., and Mosekilde, E. (2001). Synchronization phenomena in nephron-nephron interaction. *Chaos: An Interdisciplinary Journal of Nonlinear Science*, 11(2):417–426.

[31] Hoppensteadt, F. C. and Peskin, C. S. (2004). *Modeling and Simulation in Medicine and the Life Sciences*. Springer.

[32] Just, A. (2007). Mechanisms of renal blood flow autoregulation: dynamics and contributions. *American Journal of Physiology - Regulatory, Integrative, and Comparative Physiology*, 292(1):R1–17.

[33] Kallskog, O. and Marsh, D. J. (1990). TGF-initiated vascular interactions between adjacent nephrons in the rat kidney. *American Journal of Physiology Renal Physiology*, 259(1):F60–64.

[34] Keener, J. and Sneyd, J. (1998). *Mathematical Physiology*. Springer.

[35] Keener, T. (1972). Flow and pressure in the arteries. In *Biomechanics: Its Foundations and Objections*, pages 381–434.

[36] Kleinstreuer, N. C. (2009). *Mathematical Modeling of Renal Autoregulation*. PhD thesis, University of Canterbury.

[37] Kleinstreuer, N. C., David, T., Plank, M. J., and Endre, Z. (2008). Dynamic myogenic autoregulation in the rat kidney: a whole-organ model. *American Journal of Physiology Renal Physiology*, 294(6):F1453–1464.

[38] Komlosi, P., Fintha, A., and Bell, P. D. (2004). Current mechanisms of macula densa cell signalling. *Acta Physiologica Scandinavica*, 181(4):463–469.

[39] Komlosi, P., Fintha, A., and Bell, P. D. (2006). Unraveling the relationship between macula densa cell volume and luminal solute concentration osmolality. *Kidney International*, 70(5):865–871.

[40] Kriz, W. and Bankir, L. (1988). A standard nomenclature for structures of the kidney. The Renal Commission of the International Union of Physiological Sciences (IUPS). *American Journal of Physiology Renal Physiology*, 254(1):F1–8.

[41] Layton, A., Moore, L., and Layton, H. (2009). Multistable dynamics mediated by tubuloglomerular feedback in a model of coupled nephrons. *Bulletin of Mathematical Biology*, 71(3):515–555.

[42] Layton, H. E., Pitman, E. B., and Moore, L. C. (1991). Bifurcation analysis of TGF-mediated oscillations in SNGFR. *American Journal of Physiology Renal Physiology*, 261(5):F904–919.

[43] Layton, H. E., Pitman, E. B., and Moore, L. C. (1995). Instantaneous and steady-state gains in the tubuloglomerular feedback system. *American Journal of Physiology Renal Physiology*, 268(1):F163–174.

[44] Layton, H. E., Pitman, E. B., and Moore, L. C. (1997). Spectral properties of the tubuloglomerular feedback system. *American Journal of Physiology Renal Physiology*, 273(4):F635–649.

[45] Layton, H. E., Pitman, E. B., and Moore, L. C. (2000). Limit-cycle oscillations and tubuloglomerular feedback regulation of distal sodium delivery. *American Journal of Physiology Renal Physiology*, 278(2):F287–301.

[46] Layton, H. E. and Weinstein, A. M. (2002). *Membrane transport and renal physiology, Volume 129 of The IMA volumes in mathematics and its applications*. Springer.

[47] Leyssac, P. and Baumbach, L. (1983). An oscillating intratubular pressure response to alterations in Henle loop flow in the rat kidney. *Acta Physiologica Scandinavica*, 117:415–419.

[48] Leyssac, P. and Holstein-Rathlou, N. (1986). Effects of various transport inhibitors on oscillating TGF pressure responses in the rat. *Pflügers Archiv European Journal of Physiology*, 407:285–291.

[49] Leyssac, P. P. (1986). Further studies on oscillating tubulo-glomerular feedback responses in the rat kidney. *Acta Physiologica Scandinavica*, 126(2):271–277.

[50] Leyssac, P. P. and Holstein-Rathlou, N. H. (1989). Tubulo-glomerular feedback response: enhancement in adult spontaneously hypertensive rats and effects of anaesthetics. *Pflügers Archiv European Journal of Physiology*, 413(3):267–272.

[51] Loutzenhiser, R., Bidani, A., and Chilton, L. (2002). Renal myogenic response: Kinetic attributes and physiological role. *Circulatory Research*, 90(12):1316–1324.

[52] Loutzenhiser, R., Bidani, A. K., and Wang, X. (2004). Systolic pressure and the myogenic response of the renal afferent arteriole. *Acta Physiologica Scandinavica*, 181(4):407 – 413.

[53] Macey, R. (1965). Hydrodynamics in the renal tubule. *Bulletin of Mathematical Biology*, 27(2):117–124.

[54] Marieb, E. N. (1998). *Human anatomy and physiology*. Benjamin/Cummings Science Publishing.

[55] Marsh, D. J., Sosnovtseva, O. V., Chon, K. H., and Holstein-Rathlou, N.-H. (2005). Nonlinear interactions in renal blood flow regulation. *American Journal of Physiology Regulatory, Integrative, and Comparative Physiology*, 288(5):R1143–1159.

[56] Marsh, D. J., Sosnovtseva, O. V., Mosekilde, E., and Holstein-Rathlou, N.-H. (2007). Vascular coupling induces synchronization, quasiperiodicity, and chaos in a nephron tree. *Chaos: An Interdisciplinary Journal of Nonlinear Science*, 17(1):015114.

[57] Martini, F. H. (2006). *Fundamentals of Anatomy and Physiology*. Pearson.

[58] Morgan, T. and Berliner, R. (1968). Permeability of the loop of Henle, vasa recta, and collecting duct to water, urea, and sodium. *American Journal of Physiology*, 215(1):108–115.

[59] Navar, L. G., Inscho, E. W., Majid, S. A., Imig, J. D., Harrison-Bernard, L. M., and Mitchell, K. D. (1996). Paracrine regulation of the renal microcirculation. *Physiological Reviews*, 76(2):425–536.

[60] Pitman, E. B., Zaritski, R. M., Kesseler, K. J., Moore, L. C., and Layton, H. E. (2004). Feedback-mediated dynamics in two coupled nephrons. *Bulletin of Mathematical Biology*, 66(6):1463–1492.

[61] Postnov, D. E., Sosnovtseva, O. V., Mosekilde, E., and Holstein-Rathlou, N. H. (2001). Cooperative phase dynamics in coupled nephrons. *International Journal of Modern Physics B*, 15:3079–3098.

[62] Radhakrishnamacharya, G., Chandra, P., and Kaimal, M. (1981). A hydrodynamical study of the flow in renal tubules. *Bulletin of Mathematical Biology*, 43(2):151–163.

[63] Rhoades, R. A. and Bell, D. R. (2009). *Medical physiology - Principles for clinical medicine*. Lippincott Williams and Wilkins.

[64] Sakai, T., Craig, D. A., Wexler, A. S., and Marsh, D. J. (1986). Fluid waves in renal tubules. *Biophys Journal*, 50(5):805–813.

[65] Sherwin, S., Franke, V., Peir, J., and Parker, K. (2003). One-dimensional modelling of a vascular network in space-time variables. *Journal of Engineering Mathematics*, 47(3):217–250.

[66] Sosnovtseva, O. V., Pavlov, A. N., Mosekilde, E., and Holstein-Rathlou, N.-H. (2002). Bimodal oscillations in nephron autoregulation. *Physical Review E*, 66(6):061909.

[67] Sosnovtseva, O. V., Postnov, D. E., Mosekilde, E., and Holstein-Rathlou, N. H. (2003). Synchronization of tubular pressure oscillations in interacting nephrons. *Chaos, Solitons & Fractals*, 15(2):343–369.

[68] Suckow, M. A., Weisbroth, S. H., and Franklin, C. L. (2006). *The Laboratory Rat*. Elsevier.

[69] Vallon, V. (2003). Tubuloglomerular Feedback and the Control of Glomerular Filtration Rate. *News Physiol Sci*, 18(4):169–174.

[70] Wagner, A. J., Holstein-Rathlou, N. H., and Marsh, D. J. (1997). Internephron coupling by conducted vasomotor responses in normotensive and spontaneously hypertensive rats. *American Journal of Physiology Renal Physiology*, 272(3):F372–379.

[71] Wagner, C. D. and Persson, P. B. (1994). Two ranges in blood pressure power spectrum with different 1/f characteristics. *American Journal of Physiology Heart and Circulatory Physiology*, 267(2):H449–454.

[72] Wikipedia (2009). NavierStokes equations. `http://en.wikipedia.org/wiki/Navier_Stokes`.

[73] Yip, K. P., Holstein-Rathlou, N. H., and Marsh, D. J. (1992). Dynamics of TGF-initiated nephron-nephron interactions in normotensive rats and SHR. *American Journal of Physiology Renal Physiology*, 262(6):F980–988.

[74] Yip, K. P., Holstein-Rathlou, N. H., and Marsh, D. J. (1993). Mechanisms of temporal variation in single-nephron blood flow in rats. *American Journal of Physiology Renal Physiology*, 264(3):F427–434.

[75] Young, D. K. and Marsh, D. J. (1981). Pulse-wave propagation in rat renal tubules - implications for GFR auto-regulation. *American Journal of Physiology Renal Physiology*, 240(5):F446–F458.